Towards a better understanding of the Anthropogenic Impact on the Hydrological Cycle: Detecting and Estimating Irrigation through Remote Sensing Soil Moisture

Jacopo Dari

http://hdl.handle.net/10803/671502

DOTTORATO DI RICERCA IN
INTERNATIONAL DOCTORATE IN CIVIL AND ENVIRONMENTAL
ENGINEERING

CICLO XXXIII

COORDINATORE Prof. Borri Claudio

Towards a better understanding of the Anthropogenic Impact on the Hydrological Cycle: Detecting and Estimating Irrigation through Remote Sensing Soil Moisture

Settore Scientifico Disciplinare ICAR/02

Dottorando
Dott. Dari Jacopo

Tutore
Prof. Morbidelli Renato

Coordinatore
Prof. Borri Claudio

Anni 2017/2020

DOCTORAL THESIS

Title	Towards a better understanding of the Anthropogenic Impact on the Hydrological Cycle: Detecting and Estimating Irrigation through Remote Sensing Soil Moisture
Presented by	Jacopo Dari
Centre	Ebro Observatory University Institute
Department	Geophysics
Directed by	Prof. Renato Morbidelli Dr. Luca Brocca Dr. Pere Quintana-Seguí

INTERNATIONAL DOCTORATE IN CIVIL AND ENVIRONMENTAL
ENGINEERING

Department of Civil and Environmental Engineering

Universities of Florence, Perugia, and Pisa

PH.D. PROGRAM IN INFORMATION TECHNOLOGIES AND ITS
APPLICATIONS IN MANAGEMENT, ARCHITECTURE AND GEOPHYSICS

Ebro Observatory

Ramon Llull University, Barcelona

Towards a better understandig of the Anthropogenic Impact on the Hydrological Cycle: Detecting and Estimating Irrigation through Remote Sensing Soil Moisture

PhD Candidate: Jacopo Dari, XXXIII cycle

Italian supervisors:

Prof. Eng. Renato Morbidelli

Department of Civil and Environmental Engineering, University of Perugia

Dr. Eng. Luca Brocca

National Research Council, Research Institute for Geo-Hydrological Protection

Spanish supervisor:

Dr. Pere Quintana-Seguí

Ebro Observatory, Ramon Llull University

Abstract

Irrigation is the primary source of anthropogenic freshwater consumptions. The exploitation of water resources to improve the food production through irrigation practices is expected to further increase in the upcoming decades. In fact, the population growth and climate changes are expected to put even more pressure on the available water resources. Despite irrigation having direct implications on the rational management of water resources, as well as on food production, a detailed knowledge of where irrigation actually occurs worldwide and of how much water is actually used for irrigation practices is missing. In this research, approaches to detect and map areas where irrigation actually occurs, as well as methods to estimate the amounts of water applied for irrigation, have been developed; the proposed methodologies exploit remote sensing soil moisture. Two case studies have been considered in this research: the first one is located within the Ebro basin, in North-eastern Spain, while the other one is the Upper Tiber basin, in central Italy. Several remotely sensed soil moisture products at different spatial resolutions have been tested to evaluate the best performing ones in detecting irrigation signals and thus mapping irrigated areas. In addition, quantitative estimates of the water amounts applied for irrigation have been performed.

The irrigation detection and mapping activity has been carried out over both case studies. In the Spanish one, the capability to detect irrigation of several remote sensing products has been initially assessed. The following soil moisture data sets have been evaluated: SMAP (Soil Moisture Active Passive) at 1 km and 9 km, SMOS (Soil Moisture and Ocean Salinity) at 1 km, Sentinel-1 at 1 km, and ASCAT (Advanced SCATterometer) at 12.5 km. The 1 km versions of SMAP and SMOS are obtained through downscaling with the DISPATCH (DISaggregation based on Physical And Theoretical scale CHange) method. The detectability of irrigation by the considered products has been assessed through indices derived from the temporal stability theory here used under this new perspective. Furthermore, maps of irrigated areas have been produced through the K-means clustering algorithm. Over the agricultural areas in the Upper Tiber basin, in Italy, a double-scale analysis has been carried out. In the analysis at 1 km spatial resolution, the

same procedure adopted over the case study in the Ebro basin to evaluate the detectability of irrigation through remotely sensed soil moisture has been applied. The following products have been used: SMAP at 1 km, the Sentinel-1 at 1 km version delivered by the Copernicus Global Land Service, and a plot-scale-born Sentinel-1 version (produced by THEIA) aggregated at 1 km. Note that the first two products are the same used over the Spanish case study also. In this analysis, as well as in the one carried out over the study area in the Ebro basin, surface soil moisture simulated by the SURFEX-ISBA (*SURface EXternalisée - Interaction Sol Biosphère Atmosphère*) land surface model has been used as support. In the plot-scale analysis, THEIA Sentinel-1 data aggregated at 100 m have been used to produce high-resolution maps of irrigated areas through the K-means clustering algorithm.

The irrigation quantification activity has been carried out over the study area in the Ebro basin only; two experiments have been performed: one exploiting SMAP at 1 km data and another one exploiting SMOS at 1 km data. Both data sets have been used to force the SM2RAIN algorithm adapted to estimate irrigation. A more realistic modeling of the evapotranspiration term has been implemented into the algorithm to properly reproduce the crop evapotranspiration according to the FAO (Food and Agriculture Organization) model.

The analyses carried out are aimed at filling the existing gaps in the irrigation-related research field; the obtained results are useful to assess the impact of irrigation practices on the hydrological cycle.

KEYWORDS: Irrigation Mapping, Irrigation Estimates, Remote Sensing, Soil Moisture, Land Surface Modeling.

Sommario

L'irrigazione è la principale fonte di consumo di acqua dolce. Nei prossimi decenni è atteso un ulteriore sfruttamento della risorsa idrica per incrementare la produzione di cibo attraverso le pratiche irrigue. Si stima infatti che la crescita della popolazione e i cambiamenti climatici possano esercitare una pressione ancora maggiore sulle risorse idriche disponibili. Nonostante le importanti implicazioni che ha l'irrigazione sulla gestione razionale dell'acqua e sulla produzione di cibo, non si ha una conoscenza dettagliata di dove l'irrigazione effettivamente avvenga nel mondo e di quanta acqua venga effettivamente utilizzata per le pratiche irrigue. In questa ricerca sono stati sviluppati approcci per rilevare e mappare le aree dove effettivamente si verifica l'irrigazione e per stimare i volumi irrigui; le metodologie proposte sfruttano l'umidità del suolo rilevata da satellite. In questa ricerca sono stati considerati due casi di studio: il primo si trova nel bacino del fiume Ebro, nel Nord-Est della Spagna, mentre l'altro è il bacino superiore del Tevere, nell'Italia centrale. Diversi prodotti di umidità del suolo da satellite, caratterizzati da diverse risoluzioni spaziali, sono stati valutati al fine di determinare i più performanti nel rilevare segnali di irrigazione e quindi mappare le aree irrigate. Inoltre, sono state eseguite stime quantitative dei volumi di acqua utilizzati per pratiche irrigue.

L'attività di rilievo e mappatura dell'irrigazione è stata condotta su entrambe le aree pilota. In quella spagnola, è stata valutata la capacità di rilevare l'irrigazione di diversi prodotti di umidità del suolo. Sono stati considerati i seguenti set di dati: SMAP (*Soil Moisture Active Passive*) a 1 km e 9 km, SMOS (*Soil Moisture and Ocean Salinity*) a 1 km, Sentinel-1 a 1 km e ASCAT (*Advanced SCATterometer*) a 12.5 km. Le versioni a 1 km di SMAP e SMOS sono ottenute tramite disaggregazione eseguita con il metodo DISPATCH (*DISaggregation based on Physical And Theoretical scale CHange*). La capacità di rilevare l'irrigazione da parte dei prodotti considerati è stata valutata tramite indici derivanti dalla teoria della stabilità temporale e usati in questo studio sotto una nuova prospettiva. Inoltre, sono state prodotte delle mappe delle aree irrigate attraverso l'algoritmo di classificazione K-means. Un'analisi a doppia scala spaziale è stata condotta sulle aree agricole all'interno del bacino superiore del Tevere, in Italia. Nell'ambito dell'analisi alla risoluzione

spaziale di 1 km, è stata applicata la stessa procedura già adottata per il caso di studio nel bacino dell'Ebro per valutare la possibilità di rilevare l'irrigazione tramite umidità del suolo da satellite. Sono stati utilizzati i seguenti prodotti: SMAP a 1 km, la versione a 1 km di Sentinel-1 fornita da *Copernicus Global Land Service* e una versione di Sentinel-1 originariamente prodotta de THEIA alla scala di parcella e aggregata a 1 km. Va sottolineato che i primi due prodotti menzionati sono stati utilizzati anche sull'area pilota in Spagna. Sia in questa analisi che in quella condotta nel bacino dell'Ebro, dati di umidità del suolo superficiale modellati tramite il modello di superficie terrestre SURFEX-ISBA (*SURface EXternalisée - Interaction Sol Biosphère Atmosphère*) sono stati utilizzati come supporto. Nell'analisi alla scala di parcella, sono stati impiegati i dati di Sentinel-1 prodotti da THEIA e aggregati a 100 m al fine di produrre mappe di aree irrigate ad alta risoluzione tramite l'algoritmo di classificazione K-means.

L'attività di quantificazione dell'irrigazione è stata finalizzata solamente per l'area pilota nel bacino dell'Ebro; sono stati condotti due esperimenti: uno utilizzando i dati da SMAP a 1 km e un altro sfruttando i dati da SMOS a 1 km. Entrambi i set di dati sono stati utilizzati per forzare la versione dell'algoritmo SM2RAIN adattata per la stima dell'irrigazione. Una modellazione più realistica dell'evapotraspirazione è stata implementata nell'algoritmo al fine di riprodurre adeguatamente l'evapotraspirazione delle colture secondo il modello FAO (*Food and Agriculture Organization*).

Le analisi condotte sono finalizzate a colmare le lacune esistenti nel campo di ricerca relativo all'irrigazione; i risultati ottenuti sono utili per valutare l'impatto delle pratiche irrigue sul ciclo idrologico.

PAROLE CHIAVE: Mappatura dell'Irrigazione, Stima dell'Irrigazione, Telerilevamento, Umidità del Suolo, Modellazione della Superficie Terrestre.

Resum

El reg és el principal consum antropogènic d'aigua dolça. Es preveu que l'explotació dels recursos hídrics per a millorar la producció d'aliments mitjançant pràctiques de reg seguirà augmentant en els propers decennis. De fet, es preveu que el creixement demogràfic i els canvis climàtics exerceixin una pressió encara més gran sobre els recursos hídrics disponibles. Tot i que el reg té conseqüències directes en la gestió racional dels recursos hídrics, així com en la producció d'aliments, cal un coneixement detallat dels llocs en què realment es rega a tot el món i de quanta aigua s'utilitza realment per les pràctiques de reg. En aquesta investigació s'han elaborat mètodes per detectar i cartografiar les zones on realment es rega, així com mètodes per estimar les quantitats d'aigua que s'apliquen per al reg; les metodologies proposades utilitzen dades d'humitat del sòl provinents de la teledetecció espacial. En aquesta investigació s'han adoptat dos casos d'estudi: el primer es troba a la conca de l'Ebre, al nord-est d'Espanya, mentre que l'altre és la conca de l'Alt Tíber, a Itàlia central. S'han assajat diversos productes d'humitat del sòl obtinguts per teledetecció amb diferents resolucions espacials per avaluar els que millor funcionen en la detecció de reg i, per tant, en la cartografia de les zones de regadiu. A més, s'han realitzat estimacions quantitatives de les quantitats d'aigua aplicades per al reg.

L'activitat de detecció i cartografia del reg s'ha dut a terme en els dos casos d'estudi. En l'espanyol s'ha avaluat inicialment la capacitat de detecció de reg de diversos productes de teledetecció. S'han avaluat els següents jocs de dades d'humitat del sòl: SMAP (*Soil Moisture Active Passive*) a 1 km i 9 km, SMOS (*Soil Moisture and Ocean Salinity*) a 1 km, Sentinel-1 a 1 km, i ASCAT (*Advanced SCATterometer*) a 12,5 km. Les versions d'1 km de SMAP i SMOS s'obtenen mitjançant la desagregació amb el mètode DISPATCH (*DISaggregation based on Physical And Theoretical scale CHange*). La detectabilitat del reg pels productes considerats s'ha avaluat mitjançant índexs derivats de la teoria d'estabilitat temporal aquí utilitzada sota aquesta nova perspectiva. A més, s'han elaborat mapes de les zones irrigades produïts a través de l'algoritme d'agrupament K-mitjanes. A les zones agrícoles de la conca de l'Alt Tíber, a Itàlia, s'ha realitzat una anàlisi a doble escala. En l'anàlisi a 1 km de resolució espacial s'ha aplicat el mateix

procediment adoptat en el cas d'estudi de la conca de l'Ebre per avaluar la detectabilitat del regadiu mitjançant la humitat del sòl provinent de la teledetecció. S'han utilitzat els següents productes: SMAP a 1 km, la versió Sentinel-1 a 1 km publicada pel *Copernicus Global Land Service*, i una versió Sentinel-1 a escala de la parcel·la (produïda per THEIA) agregada a 1 km. Cal observar que els dos primers productes són els mateixos que també s'han utilitzat en el cas d'estudi espanyol. En aquesta anàlisi, així com en la realitzada sobre l'àrea d'estudi a la conca de l'Ebre, s'ha utilitzat com a suport el model de superfície continental SURFEX-ISBA (*Surface EXternalisée - Interaction Sol Biosphère Atmosphère*). En l'anàlisi a escala de parcel·la, les dades de THEIA Sentinel-1 agregades a 100 m s'han utilitzat per produir mapes d'alta resolució de les zones de regadiu mitjançant l'algoritme d'agrupament K-mitjanes.

L'activitat de quantificació del reg s'ha dut a terme a la zona d'estudi a la conca de l'Ebre únicament; s'han realitzat dos experiments: un utilitzant SMAP amb dades a 1 km de resolució i un altre utilitzant SMOS amb dades a 1 km. Tots dos conjunts de dades s'han utilitzat per forçar l'algoritme SM2RAIN adaptat a l'estimació del reg. En l'algoritme s'ha aplicat una modelització més realista del terme d'evapotranspiració per reproduir adequadament l'evapotranspiració dels cultius segons el model de la FAO (Organització de les Nacions Unides per a l'Agricultura i l'Alimentació).

Les anàlisis realitzades tenen per objecte satisfer les llacunes existents en el camp de la recerca relacionada amb el reg; els resultats obtinguts són útils per avaluar l'impacte de les pràctiques de reg en el cicle hidrològic.

PARAULES CLAU: Cartografia de Reg, Estimacions de Reg, Teledetecció, Humitat del sòl, Modelització de la Superfície Continental.

Resumen

El riego es el principal consumo antropogénico de agua dulce. Se prevé que la explotación de los recursos hídricos para mejorar la producción de alimentos mediante prácticas de riego seguirá aumentando en los próximos decenios. De hecho, se prevé que el crecimiento demográfico y los cambios climáticos ejerzan una presión aún mayor sobre los recursos hídricos disponibles. A pesar de que el riego tiene consecuencias directas en la gestión racional de los recursos hídricos, así como en la producción de alimentos, falta un conocimiento detallado de los lugares en los que realmente se riega en todo el mundo y de cuánta agua se utiliza realmente para las prácticas de riego. En esta investigación se han elaborado métodos para detectar y cartografiar las zonas donde realmente se riega, así como métodos para estimar las cantidades de agua que se aplican para el riego; las metodologías propuestas utilizan datos de humedad del suelo provenientes de la teledetección espacial. En esta investigación se han adoptado dos casos de estudio: el primero se sitúa en la cuenca del Ebro, en el noreste de España, mientras que el otro es la cuenca del Alto Tíber, en Italia central. Se han ensayado varios productos de humedad del suelo obtenidos por teledetección con diferentes resoluciones espaciales para evaluar los que mejor funcionan en la detección del riego y, por lo tanto, en la cartografía de las zonas de regadío. Además, se han realizado estimaciones cuantitativas de las cantidades de agua aplicadas para el riego.

La actividad de detección y cartografía del riego se ha llevado a cabo en ambos casos de estudio. En el español se ha evaluado inicialmente la capacidad de detección de riego de varios productos de teledetección. Se han evaluado los siguientes conjuntos de datos de humedad del suelo: SMAP (*Soil Moisture Active Passive*) a 1 km y 9 km, SMOS (*Soil Moisture and Ocean Salinity*) a 1 km, Sentinel-1 a 1 km, y ASCAT (*Advanced SCATterometer*) a 12,5 km. Las versiones de 1 km de SMAP y SMOS se obtienen mediante la desagregación con el método DISPATCH (*DISaggregation based on Physical And Theoretical scale Change*). La detectabilidad del riego por los productos considerados se ha evaluado mediante índices derivados de la teoría de la estabilidad temporal aquí utilizada bajo esta nueva perspectiva. Además, se han elaborado mapas de las zonas irrigadas producidos a través del algoritmo de agrupamiento K-medias. En las zonas agrícolas de la cuenca del Alto

Tíber, en Italia, se ha realizado un análisis a doble escala. En el análisis a 1 km de resolución espacial, se ha aplicado el mismo procedimiento adoptado en el caso de estudio de la cuenca del Ebro para evaluar la detectabilidad de la irrigación mediante la humedad del suelo por teledetección. Se han utilizado los siguientes productos: SMAP a 1 km, la versión Sentinel-1 a 1 km entregada por el *Copernicus Global Land Service*, y una versión Sentinel-1 a escala de parcela (producida por THEIA) agregada a 1 km. Obsérvese que los dos primeros productos son los mismos que también se utilizaron en el caso de estudio español. En este análisis, así como en el realizado sobre el área de estudio en la cuenca del Ebro, se ha utilizado como soporte el modelo de superficie terrestre SURFEX-ISBA (*SURface EXternalisée - Interaction Sol Biosphère Atmosphère*). En el análisis a escala de parcela, los datos del THEIA Sentinel-1 agregados a 100 m se han utilizado para producir mapas de alta resolución de las zonas de regadío mediante el algoritmo de agrupamiento K-medias.

La actividad de cuantificación del riego se ha llevado a cabo en la zona de estudio de la cuenca del Ebro únicamente; se han realizado dos experimentos: uno explotando SMAP con datos a 1 km de resolución y otro explotando SMOS con datos a 1 km. Ambos conjuntos de datos se han utilizado para forzar el algoritmo SM2RAIN adaptado a la estimación del riego. En el algoritmo se ha aplicado una modelización más realista del término de evapotranspiración para reproducir adecuadamente la evapotranspiración de los cultivos según el modelo de la FAO (Organización de las Naciones Unidas para la Agricultura y la Alimentación).

Los análisis realizados tienen por objeto colmar las lagunas existentes en el campo de la investigación relacionada con el riego; los resultados obtenidos son útiles para evaluar el impacto de las prácticas de riego en el ciclo hidrológico.

PALABRAS CLAVE: Cartografía de Riego, Estimaciones de Riego, Teledetección, Humedad del Suelo, Modelización de la Superficie Terrestre.

Acknowledgements

I can only start by thanking Prof. Renato Morbidelli, who first believed in me and made this great experience possible. He has been providing me with constant and wise guidance; the faith he has always placed in me has been an impulse to constantly improve myself. Thanks for inspiring me since I was a student. I wish to thank Dr. Luca Brocca, or just "Luca"; I had the pleasure to work with him since my M.Sc. thesis. Luca has been a bright mentor, always available to support me and to answer my questions. Moreover, his way of being has inspired me and spurred me on during these years. I wish to thank Dr. Pere Quintana-Seguí, "Pere". I use to say that my PhD experience would not have been so satisfying for me without meeting Pere. I deeply believe in these words. He has been a careful mentor, he has taught me a lot of technical work essential for my thesis, and he has made me feel at home during my stay in Tortosa. His physics-based point of view has opened my mind a lot.

I wish to thank the members of the hydrology group of the DICA-University of Perugia, Prof. Carla Saltalippi and Prof. Alessia Flammini, "Alessia". I thank Prof. Satalippi for the support she has always provided me, for her bluntness, which is her distinctive feature but hiding a world I had the pleasure to discover. I wish to thank Alessia, my "roommate", for her support, for the laughter, the confidences, the chats, and much more moments together. She made me feel comfortable since my first PhD day. I also wish to thank all the colleagues from the CNR-IRPI. It has been very formative for me to work in such a stimulating environment. A special thanks goes to Sara and Paolo, we shared ideas, thoughts, and laughter.

I wish to acknowledge my parents. My mother Anna is my pillar, always ready to support me with just one word or one gesture and to rejoice with me in the best moments. I thank my father Marco for his support and for the pride he has always manifested in his own way.

I wish to thank Arianna. She is fundamental for me; she has alleviated the worst moments and completed the best ones. During this journey, her eyes have been my light.

I thank my friends for having always supported me and for being the family I have chosen.

Finally, I wish to thank all the people I met during my stay in Tortosa, especially Ana, Jordi, and Julia. It is thanks to all of you that I can say I have another place I miss like home.

Table of Contents

List of Figures

List of Tables

Chapter 1

Introduction

1.1 Anthropogenic Pressure on Water Resources: Why Focus on Irrigation?

The hydrological cycle consists of all the transformations and status changes undergone by water on Earth and regulated by the geophysical processes determining its circulation on the Earth's surface and its exchanges with the atmosphere. All the forms under which water is present on Earth (e.g., rivers, lakes, oceans, glaciers) are also components of the cycle. The principal processes constituting the hydrological cycle are the precipitation, the infiltration, the evapotranspiration, and the runoff generation. A well-established and widely used representation of the cycle has been proposed by the United States Geological Survey (USGS); it is provided in Figure 1.1. The water cycle and the carbon cycle represent the two main biogeochemical cycles occurring on Earth and humans strongly interact with both them.
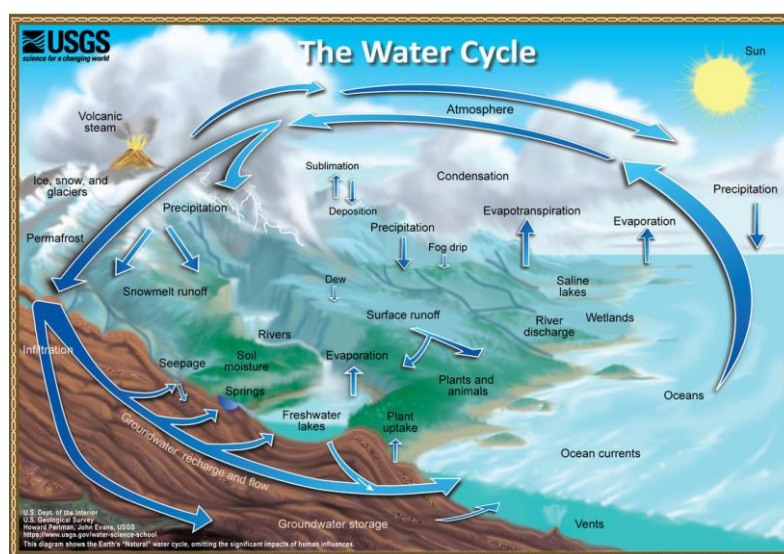
Figure 1.1. The illustration of the natural hydrological cycle proposed by the USGS.

Human interventions on the hydrological cycle can be summarized in three main categories, which are not independent on each other. The first one is represented by water withdrawals for several purposes, known as blue water uses. Humans are also responsible for soil water consumption through agricultural practices, e.g. irrigation (green water uses). Finally, water is also used for sanitary and waste disposal purposes, known as grey water uses. All the processes involved in the water cycle are directly or indirectly (or both) influenced by human activities. In addition, the natural distribution and circulation of water on the Earth's surface are also altered by humans, which stock water into reservoirs for several purposes and modify the natural paths of water courses. Human interventions on the natural hydrological cycle have reached such a magnitude as they can no more be neglected in the global economy of the hydrological cycle. Abbot et al. (2019) suggest that even the way the hydrological cycle is typically represented (e.g., the one proposed by the USGS) needs to be updated by involving anthropic activities also (see Figure 1.2).
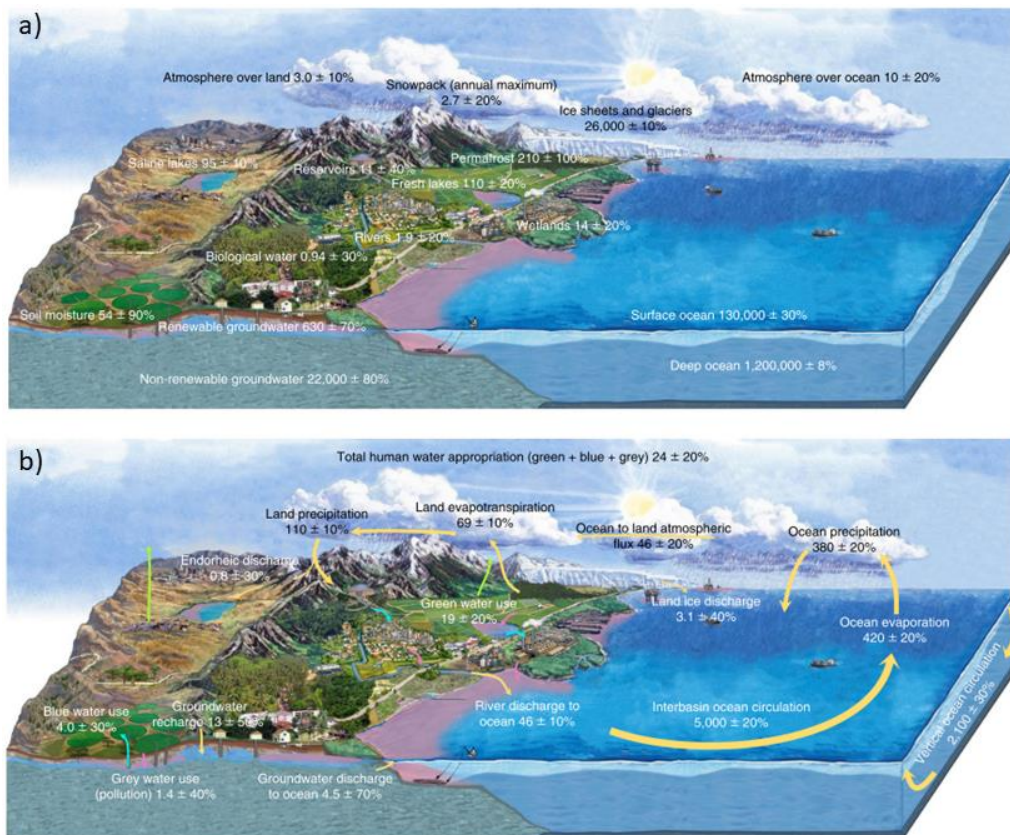
Figure 1.2. The water cycle representation proposed by Abbot et al. (2019). The major water resources, expressed in 10^3 km³, are represented in panel a), while panel b) provides the water fluxes in 10^3 km³/year.

The entity of human interventions on the hydrological cycle and more generally the influence of anthropic activities on each natural system existing on Earth has led many scientists to classify the period we are living now into a new geological era, the Anthropocene (Steffen et al., 2011; Montanari et al., 2013; Savenije et al., 2014). Pokhrel et al. (2016) claim that nowadays human impacts on the natural environment rival global geophysical processes. From a hydrological point of view, of interest for this research, irrigation is the anthropogenic activity introducing the largest imbalances in the natural water cycle from the local to the global scale (Wada et al., 2014; Alter et al., 2015). Despite an increase of cropland by only 12%, the agricultural production has been doubled thanks to irrigation during the past decades (Rosegrant et al., 2012; Gleick, 2003). In fact, although only 17% of the total croplands are irrigated, they account for 40% of the total food production worldwide. These rates are expected to further increase in the upcoming decades (Abdullah et al., 2006; Hunter et al., 2017; Ferguson et al., 2018). The ever-growing global population, as well as the ever-increasing living standards, are expected to further intensify the water depletion to boost the agricultural production, with stronger consequences over areas already facing water stress conditions and limited water availability (Vörösmarty et al., 2000; Rockström et al., 2012; Kummu et al., 2016). Hence, a massive extension of irrigated lands over arid and semi-arid areas, as well as a significant intensification of irrigated agriculture, is expected in the upcoming years to satisfy the foreseen growing demand (Ozdogan et al., 2010). According to the available estimates, over the 70% of water withdrawn from lakes, rivers, and groundwater resources is destined to irrigation practices (Cai and Rosegrant, 2002; FAO, 2006; Foley et al., 2011), thus making irrigation the main consumer of fresh water resources. The major rates of irrigation water consumptions are attributable to Europe, Northern America, Northern India, and Eastern China (Zhou et al., 2016). Irrigation practices affect water availability, food production, and climate, since heavily irrigated areas experience evaporative cooling phenomena (Moore and Rojstaczer, 2002; Kueppers et al., 2007). Despite this, a detailed information on the actual extents of irrigated lands and on the amounts of water used for irrigation practices is generally lacking worldwide. Irrigation information is essential for research purposes also; in fact, irrigation often represents the missing variable to adequately solve the hydrological balance over agricultural areas and/or anthropized basins. The development of methods and algorithms to retrieve irrigation-related information through remote sensing can bring potential benefits

that are essential for many activities: 1) the assessment of food production through irrigation practices (Vörösmarty et al., 2000), 2) the modeling of global scale water demand for irrigation (Döll and Siebert, 2002), and 3) the quantification of irrigation impacts on river discharge (Haddeland et al., 2007), on the climate (Alter et al., 2015), and on groundwater resources (Breña-Naranjo et al., 2014; Hu et al., 2016). Among the existing data sets on the spatial extent of irrigation practices, the Global Map of Irrigated Area (GMIA) developed by the Food and Agriculture Organization (FAO) of the United Nations (Siebert et al., 2015) is noteworthy. The data set contains the area equipped for irrigation (AEI) expressed as the percentage of each cell area and it is provided at a global scale on a ~10 km at the Equator spatial grid (5 arcmin resolution). Figure 1.3 shows the GMIA version 5.0 (Siebert et al., 2013).
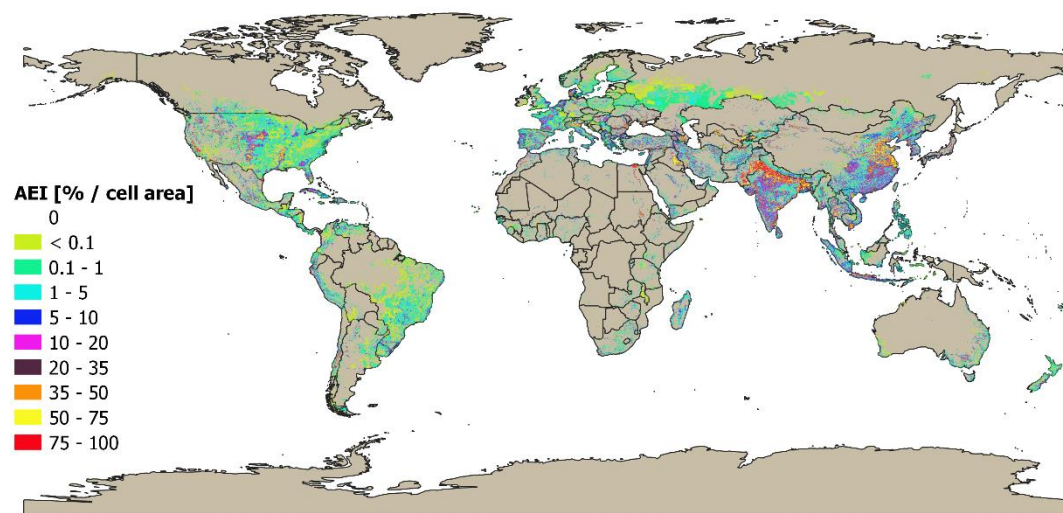
Figure 1.3. Global map of areas equipped for irrigation derived from the GMIA data set and expressed as the percentage of each cell area (derived from Siebert et al., 2013).

The map is based on national and sub-national surveys; hence, the data on the area equipped for irrigation does not represent the actually irrigated area. However, the data set is very useful to have an idea on the spatial distribution of irrigation infrastructures worldwide and for modeling purposes. The non-reproduction of the actually occurring irrigation is a common issue of the statistical-survey-based data sets, which, in addition, are often referred to specific years. The information provided in such data sets usually does not represent the spatial-temporal dynamics of irrigated areas and are often affected by not-negligible inconsistencies (Deines et al., 2017). The detailed assessment of water consumptions for irrigation

practices is even less explored than the irrigation mapping. Several obstacles, mainly the installation of monitoring systems and economic and legal limitations (e.g., illegitimate consumptions), make the information on the amounts of water actually applied for irrigation very difficult to be obtained and, at best, it is only available at a local scale and for short periods. Many studies adopt approaches aimed at modeling irrigation water requirements (Döll and Siebert, 2002; Wada et al., 2014). The outputs from these models represent a theoretical irrigation that generally does not reproduce the actually occurring one, as often crops are irrigated more or less than necessary, since the quantity of supplied water basically depends on the single farmers. As thoroughly explained in Chapter 2, remote sensing techniques have opened up new perspectives to spot where irrigation practices actually occur; in fact, observations of hydrological variables representing a proxy of irrigation (e.g., soil moisture) can be used to map irrigated areas and to retrieve the amounts of water actually applied for irrigation.

1.2 Technical Details on Irrigation Practices

The main aim of irrigation practices is to improve the productivity of an agricultural soil, thus optimizing it from an economic point of view. In general, a suitable soil for agricultural practices is characterized by an intermediate soil texture, fine enough to hold water into the soil's pores through capillarity actions but still allowing the motion of water, and not too many coarse fragments, that facilitate a rapid loss of water because of deep percolation. According to the soils' classification proposed by the USDA (United States Department of Agriculture) and provided in Figure 1.4, the sandy loam is the optimal soil texture class for agricultural purposes. Another important feature of an agricultural soil is its depth, which should be compatible with plants' roots. Finally, excesses of salts and harmful substances should be avoided.

The correct planning of irrigation practices requires the knowledge of two fundamental soil moisture values that can be derived from the soil retention curve: the field capacity and the wilting point (Mualem, 1986; Feki et al., 2018). When the soil moisture is higher than the field capacity, part of the water supplied to the crop is lost for deep percolation, as it exceeds the maximum amount absorbable by the plant. Conversely, soil moisture values lower than the wilting point lead the plant to stress conditions. An optimal irrigation practice begins before the wilting point, which should not be reached, and brings the soil moisture value close to the

field capacity; the optimal amount of water to be supplied to the crops can be determined through the water balance.
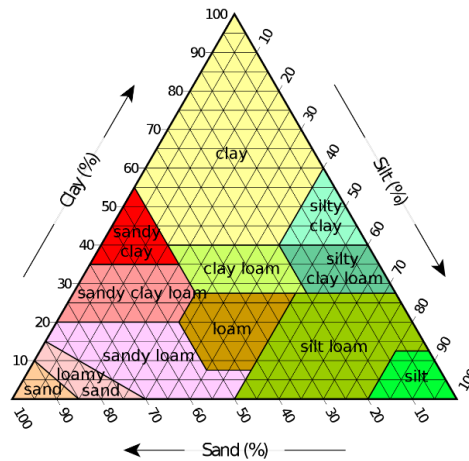
Figure 1.4. Triangle for determining the soil texture given the sand, silt, and clay fractions proposed by the USDA.

The design of an irrigation infrastructure requires the knowledge of the timing and of the water amount to be delivered during each event; in fact, after an irrigation event, the soil wetness drops down according to a drying law that can be approximated through an exponential law. As already explained, irrigation should occur when the soil moisture is close to the wilting point thus bringing it to an optimal condition. An essential parameter to be taken into account is the global efficiency of the system, which is determined by the product between the irrigation efficiency and the transport efficiency. The first one is determined by the irrigation technique adopted, while the second one is linked to the delivery of water from the withdrawal point to the final destination.

A typical irrigation system consists of a source of supply (e.g., rivers, lakes, reservoirs, groundwater or nonconventional sources such as desalinization plants) with the necessary infrastructure (e.g., wells or pumps). The network is completed by the abduction system, the distribution system, the irrigation infrastructure, and the drainage network. The abduction and distribution are realized through pressurized pipes or free surface canals. The irrigation infrastructure depends on the particular irrigation technique adopted; the most widespread ones are flood irrigation, irrigation by submersion, irrigation by infiltration, sprinkler irrigation, and drip irrigation. Figure 1.5 provides an overview on the abovementioned techniques. In the flood irrigation, a tiny layer of water flows upon the soil. In the irrigation by submersion, not-negligible amounts of water stagnate on the crop;

this technique is typically adopted for rice fields. Over fields irrigated by infiltration, only a portion of the parcel is directly wetted, e.g., through furrows. The crops' roots are fed by the water infiltrated into the soil. Underground pipes are also used for this technique. In sprinkler irrigation, the water reaches the soil as artificial rainfall. Finally, in drip irrigation systems, water is delivered close to the crop's basis with low-entity but frequent irrigation events.

The choice of the irrigation method depends on several factors: the kind of crop, the water availability, the topographic and hydrological soil features, the exposure to the wind, and economical factors. Flood irrigation is particularly suitable for intermediate soil textures and for slopes allowing the water flow; the irrigation by submersion requires soils with a low permeability. In the irrigation by infiltration, the soil texture plays a fundamental role, as it influences the distribution of water into the soil. In sprinkler irrigation, the wind is an important factor to be taken into account, as well as the sprinkler's operating pressure. Drip irrigation is particularly suitable for tree crops, as the supplied water is localized at the basis of the plant.

Finally, the drainage network is useful to move away the exceeding water, thus avoiding dangerous stagnations for the crops. The drainage systems are mainly realized through underground pipes conveying water into appropriate furrows. The depth at which such pipes are installed is of paramount importance for the system, as it influences the groundwater level. Furthermore, the design depth must ensure that the pipes are not interested by operations with agricultural machinery and must allow the delivery of the exceeding water to the disposal furrows.
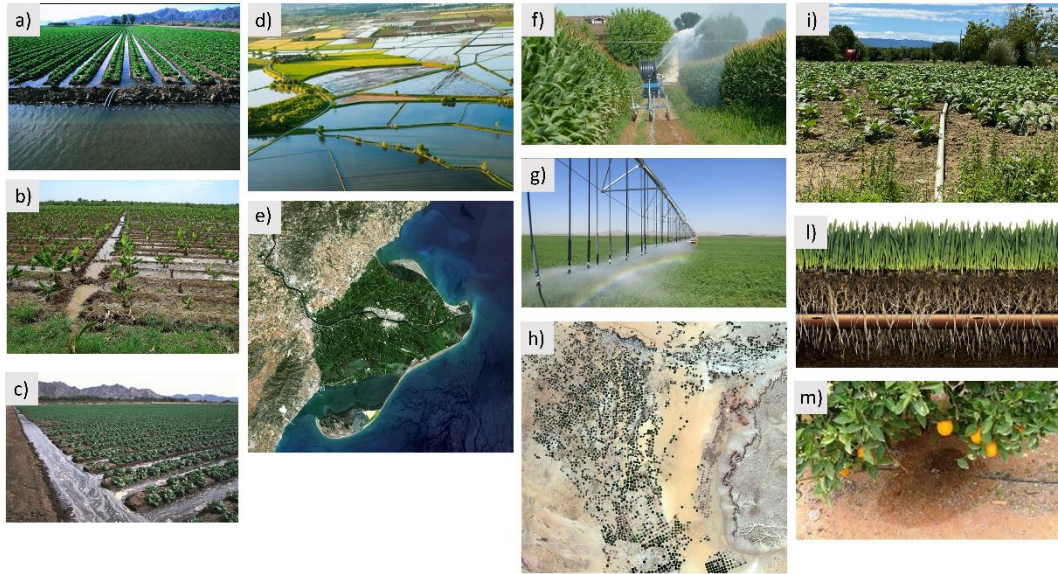
Figure 1.5. Overview on the irrigation techniques: a), b), c) flood irrigation, d) irrigation by submersion, e) Sentinel-2 image (August 14th, 2019) of the delta of the Ebro river in Spain where several rice fields irrigated by submersion can be observed, f) sprinkler irrigation, g) sprinkler irrigation through pivots, whose typical circles produced are shown in the h) Sentinel-2 image (January 16th, 2020) captured on the Wadi ad-Dawasir desert, in Saudi Arabia, i) irrigation by infiltration occurring on a tobacco field located in the Italian study area of this research, which is described in Chapter 3, l) irrigation by infiltration through underground pipes, and m) drip irrigation on fruit trees.

1.3 Objectives and Structure of the Thesis

The main objective of this research is to develop methods exploiting remotely sensed data to address the most common research questions on the irrigation topic from a hydrological perspective, namely where and when irrigation practices actually occur as well as how much water is used for irrigation purposes. Hence, the development of approaches and algorithms to retrieve irrigation-related information through remotely sensed observation is the main activity described in this thesis. The final aim is supporting the assessment of the impacts due to the primary water-affecting anthropogenic activity on the natural hydrological cycle. In order to do this, methodologies to map actually irrigated areas and to estimate irrigation water amounts have been developed. The proposed approaches are mainly based on remotely sensed soil moisture data.

The manuscript is structured in the following chapters. Chapter 2 provides the state of the art on the irrigation detection, mapping, and quantification topics. An

overview on the relevant scientific literature selected on the basis of the affinity with the methodologies proposed in this thesis is provided. Chapter 3 provides a detailed description of the case studies, namely the Ebro basin, in Spain, and the Upper Tiber basin, in Italy. Chapter 4 describes the materials and the methodologies adopted in this research to detect the actual extents of irrigation practices and to estimate the water consumptions for this purpose. Chapter 5 presents the results of the irrigation detection and mapping activity, while the results obtained in the irrigation quantification activity are provided in Chapter 6. The future perspectives of this research are discussed in Chapter 7. Finally, the conclusions of this work are summarized in Chapter 8.

Chapter 2

Remote Sensing Techniques for Mapping and Estimating Irrigation

The spread of spatial remote sensing technology has opened up perspectives of paramount importance in monitoring irrigated lands and irrigation practices worldwide. Remote sensing products have proven to be useful tools to identify where irrigation occurs; furthermore, studies describing approaches to retrieve the amounts of water applied for irrigation are recently increasing.

There are multiple benefits in exploiting satellite-derived data to monitor irrigated lands. First and foremost, this technology provides a global scale view, thus ensuring the observation of irrigation practices under different climatic conditions. Remote sensing observations can be exploited to assess the vegetation status and its changes along time. Furthermore, remotely sensed data are less time and money costly than surveys requiring aerial photogrammetry over large areas (Ozdogan et al., 2010). Among all the advantages of this technology, there is a predominant one. Remote sensing allows to map the exact location of irrigation fields, i.e., the exact location where irrigation occurs. This aspect has important implications on the rational management of water resources and it often represents a step forward in understanding the actual distribution of freshwater over anthropized areas, where the available data on irrigation and on its extent are usually limited to statistical inventories often not up to date. In addition, remote sensing technology is useful to overcome the limitations due to inconsistencies affecting the available databases based on legal irrigation inventories. However, remote sensing has also limitations. The main one is the spatial resolution of the retrieved data, often too coarse to define irrigated areas or to adequately solve the signal from adjacent pixels over highly-mixed areas. In addition, some irrigation methods (i.e. drip irrigation) are often more difficult to detect than others. Finally, when using optical data, the cloud coverage represents a limit to the data availability.

23

In the following, an overview of the relevant scientific literature on the detection (and mapping) and on the quantification of irrigation through microwave and optical remotely sensed data, selected by considering the affinity of the proposed methodologies with those presented in this thesis, is provided. In particular, the selected literature about the detection and mapping of irrigation is presented in Section 2.1, while selected studies on the irrigation estimates topic are discussed in Section 2.2.

2.1 Detecting and Mapping Irrigation

Several studies have investigated the capability of remotely sensed products to detect irrigated areas by exploiting different kinds of data sets. The selected relevant works in this field can be grouped by the type of data used: optical data only, optical data with land surface modeling, microwave data only, microwave data with optical data, and microwave data with land surface modeling (see Figure 2.1).
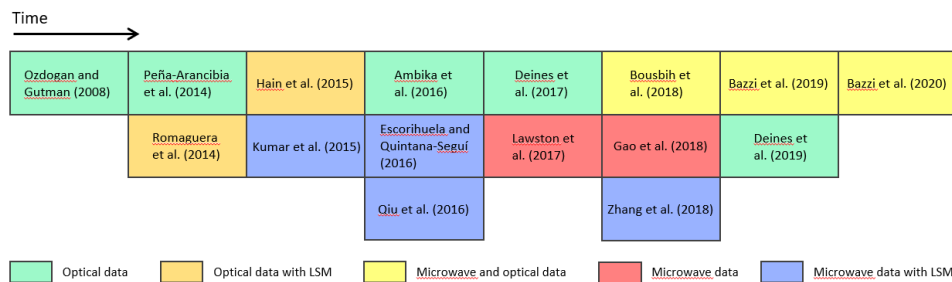
Figure 2.1. Selected relevant studies in the irrigation mapping framework divided according to the kind of remote sensing technique employed.

Ozdogan and Gutman (2008) proposed a methodology to map irrigated areas by exploiting MODIS (MODerate resolution Imaging Spectroradiometer) data and applied it over the continental United States. The authors developed a four-steps algorithm requiring MODIS and ancillary data as input to produce a binary map of irrigated areas (irrigated/not irrigated) and to assess the percentage of the irrigated area within pixels classified as irrigated. Satisfactory results were obtained, especially under dryland irrigation conditions. Peña-Arancibia et al. (2014) implemented a Random Forest classification model to identify irrigated areas within the Murray-Darling basin (Australia), which is known to be highly influenced by human activities. The data used were remotely sensed indices of the vegetation phenology and the actual evapotranspiration, along with gauge-based precipitation. The surplus of evapotranspiration with respect to the precipitation

and the vegetation phenology were found to be the best irrigation predictors. Ambika et al. (2016) exploited NDVI (Normalized Difference Vegetation Index) data retrieved by the MODIS sensor to produce high-resolution (250 m) maps of irrigated areas over the agricultural zones of India for the period 2000-2015, obtaining high accuracies (R^2 = 0.95). Deines et al. (2017) produced annual irrigation maps at high resolution (30 m) over the Republican River Basin in the United States during the period 1999-2016 by working with Landsat data on the Google Earth Engine (GEE) platform (Gorelick et al., 2017). A similar approach was proposed by Deines et al. (2019); in this study, Landsat data and the GEE computing platform were used to produce maps at 30 m resolution of annual irrigation over the High Plains Aquifer in the United States and covering the period 1984-2017.

When the aim is to detect the irrigation signal, land surface modeling is often coupled with Earth observation derived data. In general, the philosophy behind this approach is the search for differences between the behaviour of observed and modeled hydrological (or vegetation status related) variables. Generally, modeled data sets do not take into account of irrigation. Models' outputs represent the responses of the natural hydrological cycle, without any kind of human alteration; hence, if a remotely sensed data set contains the irrigation information, it can be detected by difference with modeled data sets. Romaguera et al. (2014) showed the potential in detecting irrigation by considering the differences between remotely sensed and modeled actual evapotranspiration over two pilot areas: the province of Sichuan in China and the Horn of Africa. Although the main aim of the study was to estimate the evapotranspiration rates due to irrigation practices, interesting results in detecting irrigated croplands were also obtained. In fact, high remotely sensed evapotranspiration rates were observed over an area in the Southwest of China, which is heavily irrigated according to the Global Irrigated Area Map (GIAM) proposed by Thenkabail et al. (2009). Hain et al. (2015) compared ALEXI (Atmosphere-Land EXchange Inverse) latent heat fluxes retrievals with energy fluxes modeled by the Noah land surface model over the CONUS (CONtiguous United States), finding good matches between irrigated lands and areas where non-precipitation water inputs (among others, the irrigation) affect the exchange of heat fluxes.

The use of microwave data overcomes the limitations due to the cloud coverage, a typical optical data issue. Lawston et al. (2017) highlighted the potential of the enhanced 9 km version of SMAP (Soil Moisture Active Passive) to detect irrigation

over three semiarid areas in the Western United States. The track of irrigation practices in the remotely sensed soil moisture data was more clear where flood irrigation mainly occurs with respect to other irrigation techniques (i.e., sprinkler). Gao et al. (2018) analyzed several metrics calculated from Sentinel-1 SAR (Synthetic Aperture Radar) time series to map irrigated fields over the Urgell, an agricultural area located in Catalonia, Spain. In this study, a classification of irrigated crops, not irrigated fields and irrigated trees was performed trough the Support Vector Machine (SVM). The resulting maps were validated by comparisons with ground truth data from the SIGPAC (the Geographic Information System for Agricultural Parcels) data set, obtaining an overall accuracy of 81.08%. The main limitation of the method was the correct representation of fruit trees. Another approach for irrigation mapping through satellite data is merging microwave and optical data. Bousbih et al. (2018) used optical data retrieved form Sentinel-2 and Sentinel-1 SAR observations to produce annual maps of irrigated and rainfed areas over a semi-arid region in Tunisia. The validation with pilot fields showed an accuracy up to 77%. Bazzi et al. (2019) exploited both microwave (Sentinel-1 SAR time series) and optical (Sentinel-2 retrieved NDVI time series) data to map irrigated areas in Catalonia. In order to disentangle the rainfall from the irrigation practices, Sentinel-1 signals at plot scale were compared with Sentinel-1 signals aggregated at 10 km. Different classification models were applied to SAR and optical data, obtaining overall accuracies of ~90%. A similar approach was proposed in Bazzi et al. (2020). In this study, Sentinel-1 SAR data and Sentinel-2 NDVI were exploited to detect irrigation at a plot scale over Catalonia and two additional pilot sites in France.

As in the case of optical data, microwave remote sensing data also has been used along with land surface models' outputs with the aim of detecting and mapping the irrigation extent. Kumar et al. (2015) evaluated the capability to detect irrigation over the CONUS area through remote sensing soil moisture products. The data sets used were: ASCAT (Advanced SCATterometer), ASMR-E (Advanced Microwave Scanning Radiometer-Earth Observing System), ESA CCI SM (European Space Agency Climate Change Initiative Soil Moisture), Windsat, and SMOS (Soil Moisture and Ocean Salinity). The detection of irrigated areas was performed through comparisons between remotely sensed and modeled soil moisture from the Noah land surface model, in which irrigation practices are not incorporated. Some potential in detecting irrigation signals in terms of positive biases between satellite and modeled soil moisture was obtained over the plains

of Nebraska with ASCAT data. Escorihuela and Quintana-Seguí (2016) performed a comparison between microwave remote sensing soil moisture products and soil moisture simulated with the SURFEX-ISBA (*SURface EXternalisée – Interaction Sol Biosphère Atmosphère*) land surface model over the Catalonia, in Spain. The remotely sensed data sets used were: ASCAT, ASMR-E, SMOS, and a SMOS version at 1 km obtained by downscaling the coarse resolution product through the DISPATCH (DISaggregation based on Physical And Theoretical scale CHange) algorithm (Merlin et al., 2013). Low correlations with the model's output obtained over the Urgell area, heavily irrigated, compared with higher correlations found over areas with a similar flat topography showed the potential in detecting irrigation of the 1 km version of SMOS. Qiu et al. (2016) analyzed the trends of soil moisture over China from three different sources: the ESA CCI data set, the ERA-Interim/Land (European ReAnalysis-Interim/Land) reanalysis, and in situ observations; the authors found discordances between remote sensing soil moisture and precipitation trends over irrigated areas, interpreting this issue as a signal of the irrigation practices. Zhang et al. (2018) evaluated the potential of microwave remote sensing products in detecting irrigation patterns in China. In this work, a passive microwave product (AMSR-E and its successor AMSR-2), an active microwave product (ASCAT), and a merged product (the ESA CCI data set) were compared with soil moisture from ERA-Interim to assess the detectability of irrigation in terms of differences in probability distribution functions between satellite and modeled soil moisture. The results showed some potential of the evaluated products, especially ASCAT, in detecting irrigation over arid areas in the North of China.

Despite the significant increase in the number of studies in this topic during the last decade, an assessment of the suitability of microwave remote sensing soil moisture products for detecting and mapping irrigation over areas where high resolutions (1 km or less) are needed still lacks. This task represents one of the targets of the presented research.

2.2 Irrigation Quantification

Along with the detection of the irrigation extent and of the timing of irrigation practices, the estimate of the amounts of water applied for irrigation purposes is the third fundamental goal of the irrigation-related research field.

Remotely sensed observations of fluxes and of changes in stocks involved in the hydrological cycle can be used to estimate the amounts of irrigation water. Under this perspective, soil moisture and evapotranspiration have proven to be key variables to retrieve information on the applied irrigation amounts.

Several studies exploiting satellite soil moisture observations to estimate irrigation used the adapted version of the SM2RAIN algorithm for the quantification of irrigation (e.g., Brocca et al., 2018; Jalilvand et al., 2019). The algorithm was originally developed to retrieve rainfall from soil moisture observations through a bottom-up approach (Brocca et al., 2014) and later modified to estimate irrigation. For further details on this topic, please refer to Chapter 4.

The potential of the algorithm in retrieving water amounts applied for irrigation by exploiting coarse resolution soil moisture products was shown in Brocca et al. (2018). The adapted SM2RAIN algorithm was applied over nine pilot sites in Africa, Australia, Europe, and USA with remotely sensed soil moisture observations retrieved by SMAP, SMOS, ASCAT, and AMSR-2 as input. The study provided a qualitative assessment on the possibility to estimate irrigation amounts with the SM2RAIN approach, but the need of satellite products with low uncertainties over areas experiencing long periods of low rainfall rates was pointed out; furthermore, issues related to the spatial resolution suggested the need of high-resolution products (1 km or less). Jalilvand et al. (2019) applied the SM2RAIN approach to quantify irrigation amounts during the period 2012-2015 over the Miandoab plain, in Iran. Soil moisture from the AMSR-2 data set along with rainfall and evapotranspiration data from different sources were used as model input. In the irrigated pixels, good averaged performances (R = 0.86 and RMSE = 12.895 mm/month) in reproducing benchmark irrigation data were obtained. However, other approaches exploiting remotely sensed soil moisture to retrieve irrigation water amounts exist. Zaussinger et al. (2019) developed a methodology to estimate the irrigation water use (IWU) over the CONUS area by integrating the differences between remotely sensed an modeled soil moisture variations. The data sets used were SMAP, ASCAT, AMSR-2, and MERRA-2 (Modern-Era Retrospective analysis for Research and Applications-2) reanalysis. The results showed underestimates of the IWU with respect to benchmark irrigation water withdrawals data, mainly attributable to the coarse resolution of the considered data sets. However, IWU retrieved by exploiting SMAP data showed a good correlation with state-aggregated benchmark irrigation volumes (r = 0.80). Zohaib and Choi (2020) proposed a similar approach highlighting the

potential use of coarse resolution soil moisture data to estimate IWU at a global scale: soil moisture from ERA-5 (European ReAnalysis-5) and from the ESA CCI data set were used.

Another component of the hydrological cycle that proved to be a proxy of irrigation is the evapotranspiration rate. Romaguera et al. (2014), previously mentioned in the context of the irrigation detection, also addressed the irrigation quantification target by proposing an approach based on the differences between optical remote sensing and modeled evapotranspiration to estimate monthly evapotranspiration rates attributable to irrigation practices. Another evapotranspiration-based approach was proposed by van Eekelen et al. (2015); the authors produced maps of actual evapotranspiration over the Incomati basin in Southern Africa, obtained through the surface energy balance algorithm for land, SEBAL (Bastiaanssen et al., 1998). The distinction between evapotranspiration rates due to rainfall from those determined by irrigation practices was used to indirectly estimate annual values of water withdrawals due to irrigation. Peña-Arancibia et al. (2016) combined remotely sensed data and hydrological modelling to estimate the amounts of water consumptions in the form of evapotranspiration and their sources over two sub-basins of the Murray-Darling basin, in Australia.

Figure 2.2 provides a scheme summarizing the selected studies in the quantification of irrigation topic organized on the basis of the variable exploited (soil moisture or evapotranspiration).
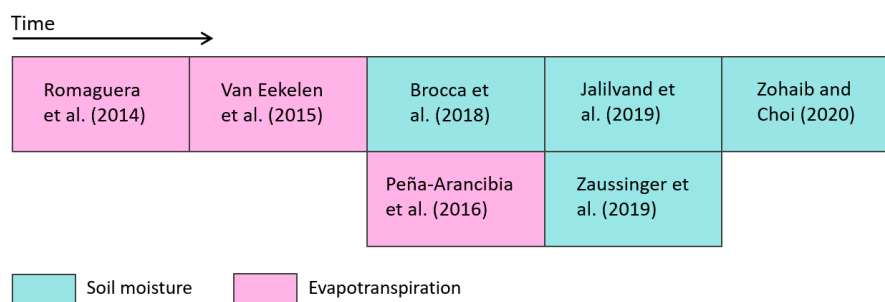
Figure 2.2. Selected relevant studies in the irrigation quantification framework divided according to the kind of remotely sensed hydrological variable used.

It is noteworthy that data assimilation represents an alternative approach to face the irrigation estimates topic (Lievens et al., 2017; Abolafia-Rosenzweig et al., 2019). Several studies investigated the benefits of ingesting remote sensing observations (assuming that they properly reproduce the changes occurring in the

land fluxes due to irrigation) into models (Kumar et al., 2015, 2019; Lei et al., 2020) in order to balance inconsistencies due to unmodeled processes. As an example, Girotto et al. (2017) investigated the possibility to correct errors due to groundwater extraction and irrigation in the Catchment land surface model by assimilating GRACE Total Water Storage (TWS). The authors pointed out not-negligible improvements in the estimation of some processes; nevertheless, the representation of other processes resulted to be impoverished. Nie et al. (2018) included a groundwater irrigation scheme and a data set of monthly time-varying greenness vegetation cover into the Noah-MP land surface model. However, the data assimilation framework is not further deepened here as it is not among the methodologies adopted in this thesis.

Despite the increasing interest and number of applications in this research field, the existing studies mainly discuss potential applications of exploiting remotely sensed data to estimate water volumes applied for irrigation, or they show the capability of remote sensing technology in deriving information and observations linked to irrigation practices. Studies reproducing the actually occurred irrigation amounts with a certain accuracy are still missing, and this issue represents one of the steps forward prosecuted in this thesis.

Chapter 3

Case Studies

The two pilot sites considered in this research are now presented. They are the Ebro basin, in the North East of the Iberian Peninsula (presented in Section 3.1) and the Upper Tiber basin, in central Italy (presented in Section 3.2). The location of the sites is shown in Figure 3.1. For both the pilot areas, a detailed description of the administrative organization of irrigated lands, of the irrigation practices and related techniques employed, and of the available irrigation benchmark data sets is provided. Additional information on topographic and land cover characteristics of sub-areas where the analyses have been focused on is provided.
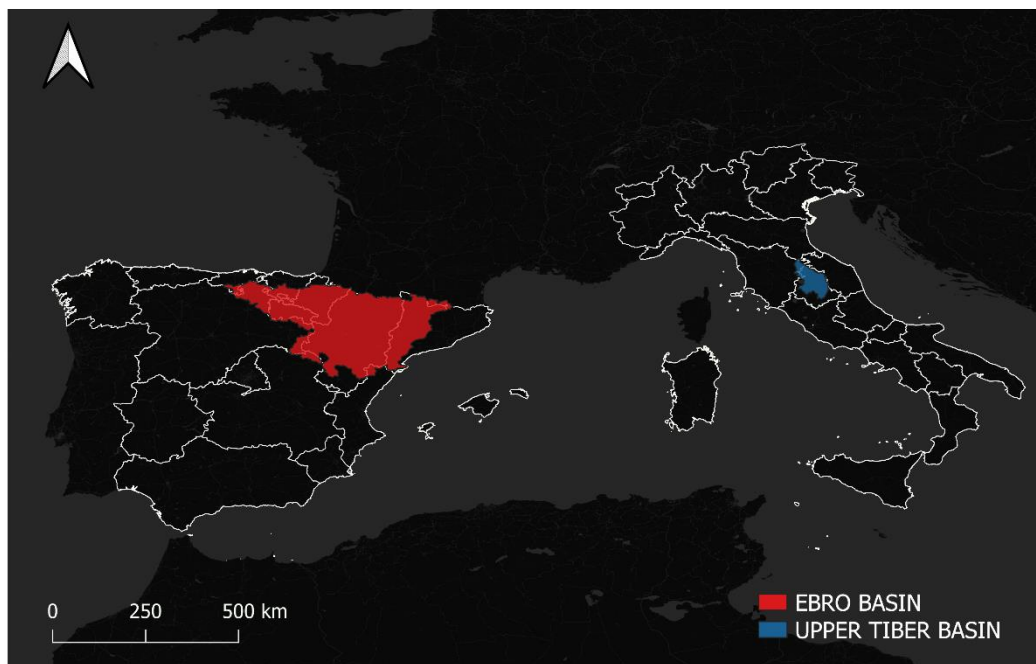
Figure 3.1. Location of the two pilot areas considered in this thesis: the Ebro basin (red) and the Upper Tiber basin (blue). The administrative edges of the regions of Spain and Italy are marked in white.

31

3.1 The Ebro Basin, Spain

The Ebro is the main Mediterranean river of the Iberian Peninsula, with a length of ~928 km; its basin has a drainage area of ~85,550 km^2. The domain is mainly characterized by a semi-arid climate, except for the Northwest, which has a continental influence, and for the Pyrenean area. Wide flat areas exist in the central part of the basin; the highest altitudes can be detected in its North side, where the Pyrenees and the Cantabrian Range are located. Within the basin, several clusters of irrigated lands exist (see Figure 3.2). Annual precipitation amounts are very heterogeneous in the area, ranging between ~2000 mm/year on the Pyrenean relief and ~200 mm/year in the central valley. The analyses presented in this thesis are mainly focused on the Eastern part of the basin, on a portion of 10,000 km^2 (125 km × 80 km) falling between Catalonia and Aragon. This tile has been chosen because it contains the widest irrigated area of the whole basin, with an extension higher than 2000 km^2. The spatial extent of the irrigated lands is shown in Figure 3.2.
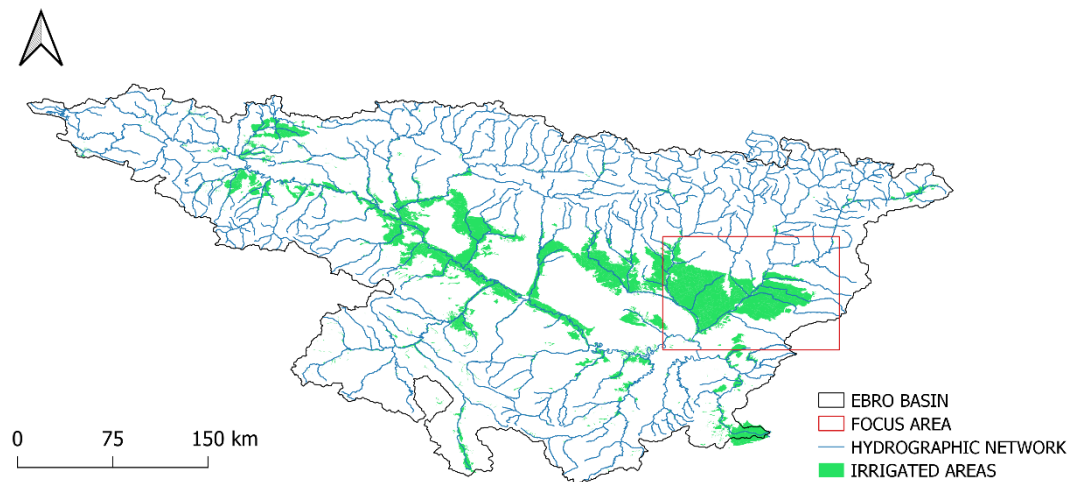
Figure 3.2. Irrigated areas within the Ebro basin, available at the website dedicated to the hydrological plan of the Ebro basin.[1]

The focus area is mostly flat and the fields in the irrigated portion are heavily irrigated each year. The prevalent crops are forage and summer cereals; fruit trees are spread on the South and in the middle of the irrigated land, along the river channel that crosses it. An area destined to vineyard is also present. On the East side, the irrigable land is surrounded by a large area of rainfed cropland, which is mixed with sparse forests, shrubs, and olive groves in the South side, in the context

---

[1] http://www.chebro.es/contenido.visualizar.do?idContenido=42695&idMenu=4780.

of a typical Mediterranean landscape. In general, this portion is dry during summer; this condition contributes in creating a homogeneous and extended dryland which contrasts with the lush irrigated areas. The different wetness conditions coexisting in the focus area, exacerbated during the dry and thus of highest-intensity irrigation season, makes the site particularly suitable to spot where irrigation occurs through remotely sensed data. In fact, the considered area has been object of several studies aimed at evaluating the detectability of irrigation signals by remote sensing products (Escorihuela and Quintana-Seguí, 2016; Fontanet et al., 2018; Gao et al., 2018; Bazzi et al., 2019). In the analysis aimed to the detection of irrigation and to the mapping of its extents, the irrigated land contained in the focus area has been divided into two macro-areas according to the organization of the irrigation canals: the Urgell area, which falls in Catalonia and is supplied by the Urgell and the Algerri Balaguer canals, and the Catalan and Aragonese area, which falls between Catalonia and Aragon and receives water from the Catalan and Aragonese canal. The organization of the study area considered in the irrigation detection framework, together with the land cover map and with the map of the area equipped for irrigation, are shown in Figure 3.3.
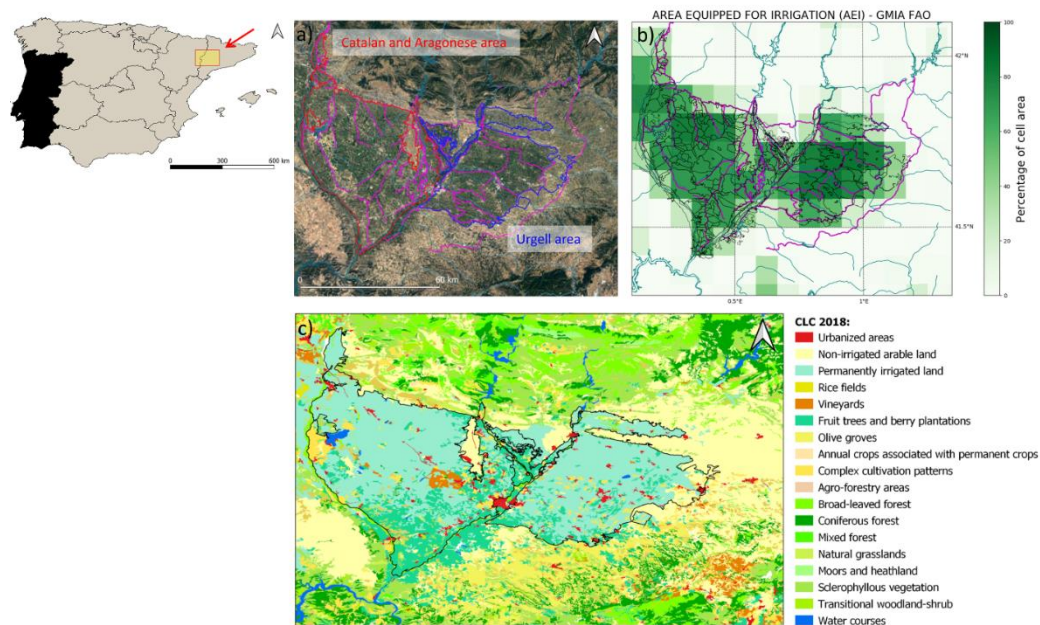
Figure 3.3. Characteristics of the pilot site: a) location with respect to Spain (top left map) and partition of the irrigated areas: Urgell area (East side) and Catalan and Aragonese area (West side), b) percentage of area equipped for irrigation according to the GMIA-FAO data set, and c) land cover map according to CLC for the year 2018. In a) and b) the irrigation canals are marked in magenta (Dari et al., 2021a).

The data on the area equipped for irrigation, expressed as a percentage of each cell area, is derived from the version 5.0 of the GMIA developed by FAO (Siebert et al., 2015). The data set has a spatial resolution of 5 arcminutes, equivalent to ~10 km at the Equator. The GMIA data set merges multi-source statistical surveys at a (sub)national scale of area equipped for irrigation and of actually irrigated area with geospatial information on irrigation practices (mainly the location and the extent) obtained by satellite imagery, land cover maps, and vector and raster data (Siebert et al., 2013). The land cover map is derived from the Corine Land Cover (CLC); it is referred to the year 2018 and it has a spatial resolution of 100 m. The map is provided by the Copernicus Land Monitoring Service. It is noteworthy that, the CLC map distinguishes between "non-irrigated arable lands" and "permanently irrigated areas".

In the analysis aimed at estimating the amounts of irrigation water, the attention has been focused on the four districts (*comunidades de regantes*) in which the irrigated area is organized: the Urgell district, the Algerri Balaguer district, the Pinyana district, and the Catalan and Aragonese district. The latter has been further divided in its Northern (North Catalan and Aragonese) and Southern (South Catalan and Aragonese) partitions, which receive water for irrigation from two different reservoirs located at North of the district. The organization of the study area according to the irrigation districts, the Digital Elevation Model (DEM) of the irrigated land, and the density of the irrigation equipment are shown in Figure 3.4; The panel a) of the figure also shows the stations exploited to derive the irrigation benchmark volumes used to validate the irrigation amounts obtained through the methodology here proposed in the irrigation quantification framework. The DEM is derived from the EU-DEM v1.1; it has a spatial resolution of 25 m and it is provided by the Copernicus Land Monitoring Service. The data on the density of irrigation equipment is part of the geospatial information attached to the hydrological Plan of the Ebro basin.

The irrigation districts have different characteristics in terms of dating, extension, and irrigation techniques adopted. The timing of the irrigation practices depends on several factors (mainly the crop type), but the highest-intensity irrigation period is between May and September; the irrigation frequency is determined by the adopted technique. The Urgell has a total area equal to 887.62 km² (88,762 ha). The irrigation system is traditional and mainly works by inundation; irrigation generally occurs by turns, every two weeks. The Algerri Balaguer has been recently modernized and extended. New irrigation systems have been installed and

irrigation can theoretically be practiced each day. Drip irrigation is used for fruit trees, while sprinkler is adopted for herbaceous crops. The district has a total area of 70.79 km^2 (7079 ha). Different irrigation techniques are employed in the Catalan and Aragonese district; sprinkler irrigation is the most widespread technique (employed over the 54% of the area), followed by drip irrigation (employed over the 28% of the area) and by flood irrigation (adopted over the 18% of the area). The total extension of the district is equal to 1161.52 km^2; the area of the Northern partition is equal to 657.04 km^2 (65,704 ha), while the Southern part has an area equal to 504.48 km^2 (50,448 ha). The Pinyana district has an area equal to 149.74 km^2 (14,974 ha) and it is fed by water coming from the homonymous canal, which is the most ancient of Catalonia. Unfortunately, the information about the irrigation techniques employed in the Pinyana district are unavailable, but mixed techniques are expected to be adopted.
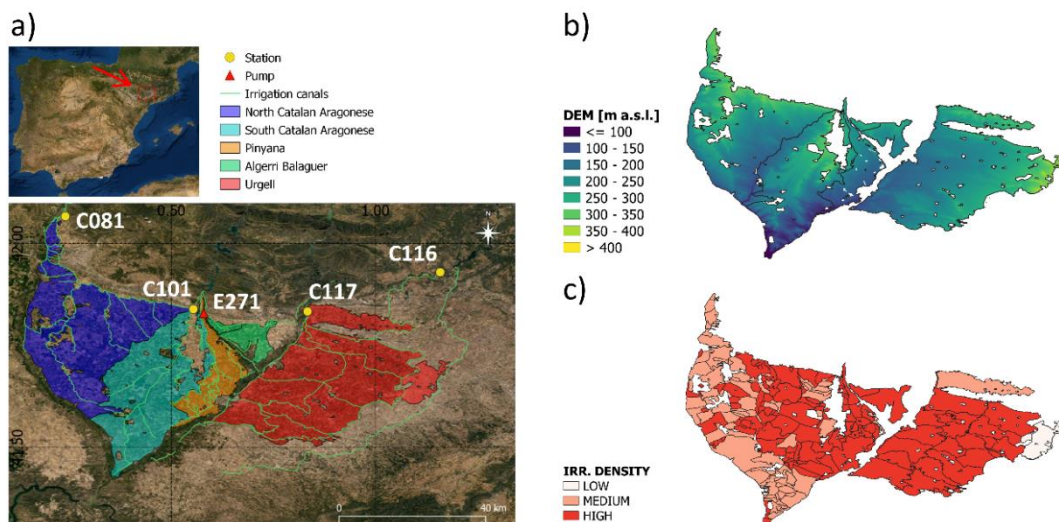
Figure 3.4. Details of the irrigated land within the area of interest: a) organization of the districts, b) DEM of the irrigated area derived by the Copernicus EU-DEM v1.1, and c) irrigation density derived by the Ebro hydrological plan (Dari et al., 2020).

3.2 The Upper Tiber Basin, Italy

The Upper Tiber Basin, located in central Italy, has a drainage area of ~5000 km^2 referred to a portion of the Tiber whose length is ~140 km. The basin mainly falls within the Umbria region and it is characterized by a complex orography determined by the Apennines. The highest altitudes can be detected in the East side, while the West side is mainly hilly, with values ranging between 100 m a.s.l and 800 m a.s.l. The mean annual rainfall of the Umbria region is ~900 mm; the

mean annual temperature varies between 3.3 °C (generally observed in January) and 14.2 °C (usually detected in July). The highest rates of monthly rainfall are concentrated in autumn and winter seasons.

In the performed analysis, a tile with an area slightly lower than 13,000 km² (~92.5 km × 138.5 km) that encloses the basin has been considered. This case study is deeply different from the precedent one in terms of management and organization of the irrigation practices. A first difference is imposed by the topography; in fact, the area is located in the upper central Apennines. For this reason, agricultural lands mainly arise over small flat areas placed between adjacent reliefs. Furthermore, the crop rotation is largely adopted, thus creating a complex irrigation mosaic each year. Another essential difference with the pilot site located in the Ebro basin is the general unavailability of accurate data on the kind of crops, as well as the lacking of information about the exact position and extent of irrigated areas. The only source of irrigation-related information are a few reports produced at a subnational scale.

On the basis of the abovementioned considerations and by merging the limited information available, four agricultural areas in the flat portion of the pilot site have been identified. These areas represent the spatial domain where irrigation can occur, but they are not expected to be completely and uniformly irrigated. The selected agricultural lands, shown in Figure 3.5, they are the Upper Tiber area (122.33 km²), the Trasimeno area (152.09 km²), the Right Tiber area (280.12 km²), and the Left Tiber area (292.12 km²).
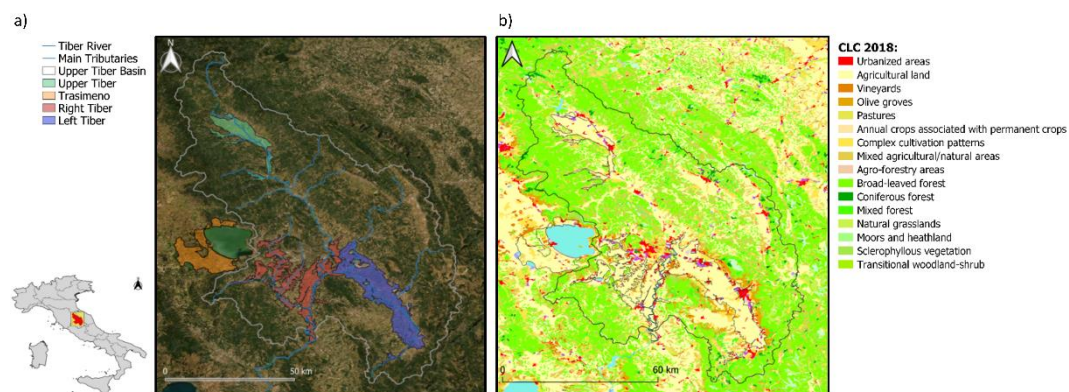
Figure 3.5. The Upper Tiber basin: a) location and b) land cover map according to CLC referred to the year 2018 (derived from Dari et al., 2021b).

The Upper Tiber area is immediately downstream of the Montedoglio dam, from which receives the predominant part of water amounts destined to irrigation

practices through the *Sistema Orientale Montedoglio* network. The area falls across two regions, Umbria and Tuscany; for this reason, the irrigation is managed by two consortia: the *Comprensorio Alto Tevere Umbro* for the portion in Umbria and the *Comprensorio Valtiberina Toscana* for the part in Tuscany. The Trasimeno area takes its name from the adjacent lake and receives water through the *Sistema Occidentale Montedoglio* network. The Right Tiber area contains the districts of the Central Tiber valley and of the Genna, Caina, and Nestore rivers' valleys. The Left Tiber area encloses the districts of the Umbrian valley; in this portion, the irrigation is managed by a consortium called *Consorzio della Bonificazione Umbra*. The figure also provides the land cover map at 100 m resolution referred to the year 2018, which is derived from the CLC data set. It is noteworthy that, in the land cover map referred to this domain the "permanently irrigated areas" class is not present. In addition, in order to avoid misunderstandings, the class "non-irrigated arable land" has been renamed as "agricultural land", as it is the class associated to the areas where irrigation can occur. Additional details on the study area are provided in Figure 3.6, which shows a topographic characterization of the site through the Copernicus EU-DEM v1.1 at 25 m resolution and the area equipped for irrigation (resolution of ~10 km) derived from the GMIA. According to this data set, the portions with the highest rates of area equipped for irrigation are located in the Upper Tiber area and in the North side of the Left Tiber area.
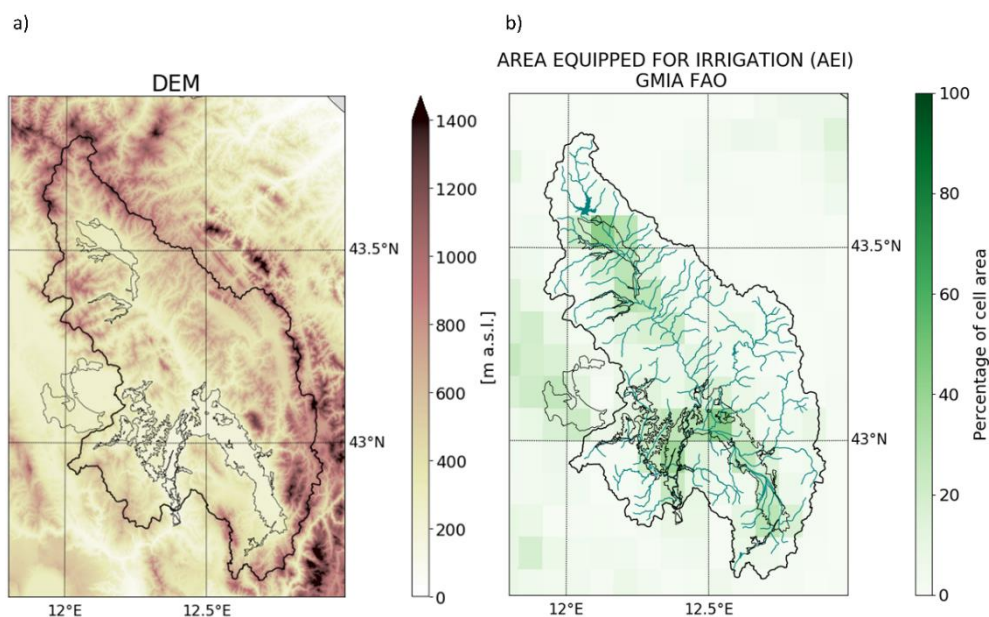
Figure 3.6. Additional details on the Upper Tiber basin: a) DEM derived by the Copernicus EU-DEM v1.1 and b) percentage of area equipped for irrigation according to the GMIA-FAO data set.

Over the pilot agricultural sites, the most widespread crops are maize, wheat, and tobacco, which is widely cultivated in the Upper Tiber area. Other crops (e.g., sunflower, forage, etc.), as well as areas destined to vineyards, are also present. Sprinkler irrigation is the most employed technique, followed by drip irrigation; in a small system within the Left Tiber area, surface irrigation is still practiced.

Chapter 4

Materials and Methods

In this chapter, the materials and methodologies used to detect irrigation and to estimate the amounts of water applied for this purpose are described. Section 4.1 provides information on the remotely sensed data employed, Section 4.2 presents the meteorological data sets used, Section 4.3 describes the SURFEX modeling platform and the performed simulations, and Section 4.4 presents the ground truth data sets. The proposed methodologies to detect and map irrigation extents and to quantify irrigation amounts are presented in Section 4.5 and Section 4.6, respectively.

4.1 Remote Sensing Data

In this section, the remotely sensed products used in this thesis are described. Within the framework of the detection and mapping of irrigation, six microwave soil moisture products have been exploited: SMAP at 1 km and 9 km, SMOS at 1 km, Sentinel-1 at 1 km and at a plot scale, and ASCAT at 12.5 km. In the irrigation quantification activity, only SMOS and SMAP at 1 km data sets have been used. However, optical products also have been exploited within this framework, namely the NDVI v2.2 and the Fraction of Vegetation Cover (FCover) v2 products delivered by the Copernicus Global Land Service. The high-resolution (1 km) versions of SMOS and SMAP products are obtained by downscaling the coarse resolution data through the DISPATCH algorithm (Merlin et al., 2013), which is described in Section 4.1.2.5. The downscaling has been executed by isardSAT. The plot scale version of Sentinel-1 is obtained by merging Sentinel-1 SAR-derived data with Sentinel-2 optical data. The description of the data sets used is preceded by a brief description of the principles of the remote sensing. Particular attention is given to the remote sensing of soil moisture. Figure 4.1 shows the satellites carrying aboard the sensors whose measurements have been exploited in this study: SMOS, SMAP, METOP-B (ASCAT), Sentinel-1, and PROBA-V.
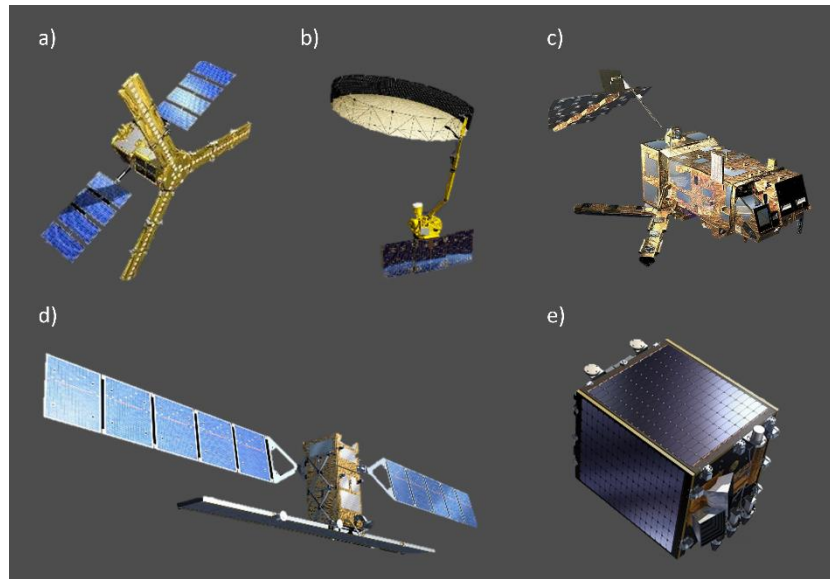
Figure 4.1. Satellites carrying aboard the sensors whose measurements have been used in this study: a) SMOS, b) SMAP, c) METOP-B (ASCAT), d) Sentinel-1, and e) PROBA-V. Note that satellites whose observations have not been directly used in this study but allowed the production of some of the data sets considered are not shown (i.e., MODIS and Sentinel-2).

4.1.1 Remote Sensing Principles

Remotely sensed data constitute the basis for all the analyses carried out in the presented thesis. Hence, in this section, a brief description of the principles beyond the remote sensing technology is provided.

In general, remote sensing is defined as the science that deals with acquiring information about the atmosphere and the Earth's surface through measurements of the electromagnetic radiation emitted or reflected from the Earth in one or more ranges of the electromagnetic spectrum. The fundamental classification in active remote sensing and passive remote sensing is based on a simple principle. In the passive remote sensing, the sensor aboard a satellite or an aircraft only receives the electromagnetic radiation reflected or emitted by the target object, which is produced by an external source (e.g., the Sun). Conversely, in active remote sensing the sensor is concurrently the source of the emitted electromagnetic radiation and the recorder of its reflection after interactions with the target object.

Electromagnetic waves (Figure 4.2) are the result of periodic disturbances of electric and magnetic fields. The propagation through space of an electromagnetic wave can be approximated by plane sine waves overlapped, with the electric field component and the magnetic field component generally orthogonal to each other

and both perpendicular with respect to the propagation direction. Defined the plane of incidence as the plane determined by the vertical and the direction of the propagation, the vertical polarization configuration is assumed when the electric field component is parallel to the plane of incidence, while in the horizontal polarization the same component is perpendicular to the plane of incidence.
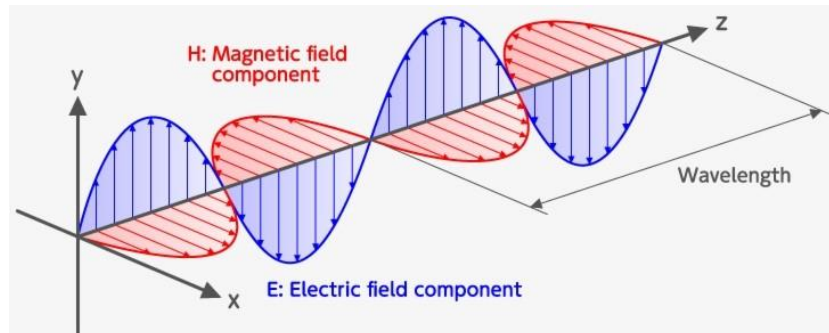
Figure 4.2. The electromagnetic wave.

Electromagnetic waves are characterized by their wavelength, λ, and their frequency, f. Between these two parameters the following relationship exists:

$$\lambda = \frac{c}{f} \tag{4.1}$$

in which c indicates the speed of light, c = 2.99792458×10^8 m/s. In the remote sensing technology, information on the Earth's surface is obtained by measuring the transmission of the energy associated to an electromagnetic wave. The whole range of all the possible wavelengths in which the energy associated to an electromagnetic wave can be distributed is the electromagnetic spectrum, which is organized in seven portions going from lower frequencies and longer wavelengths to higher frequencies and shorter wavelengths: radio waves, microwaves, infrared, visible light, ultraviolet, X-rays, and gamma rays. Figure 4.3 shows the electromagnetic spectrum. The remote sensing technology uses different adjacent portions of the spectrum for different purposes. The most common bands exploited are microwaves, infrared, and visible radiation. The particular band used allows the distinction between microwave products and optical products. The main advantages of microwave remote sensing with respect to optical remote sensing are that the cloud coverage is not an issue and the capability to collect measurements during day and night. Furthermore, optical remote sensing is less sensitive to the dielectric constant of surface characteristics (e.g., canopy structure or roughness) with respect to microwave remote sensing (Dobson and Ulaby, 1981; Ulaby et al., 1986). Although soil moisture can be remotely sensed in the visible

band (through measurements of the albedo, defined as the solar radiation reflected from the Earth's surface and which is linked with soil moisture), and in the infrared band (through measurements of the land surface temperature eventually combined with vegetation indices) also, the portion of the spectrum occupied by microwaves is the most exploited one for soil moisture measurements.

Active and passive microwave remote sensing techniques exploit electromagnetic radiations with wavelengths varying between 10^{-3} m and 3.3×10^{-1} m, corresponding to a range of frequencies between 1 GHz and 300 GHz. The microwave region sub-portion of interest in remote sensing application is provided in panel b) of Figure 4.3.
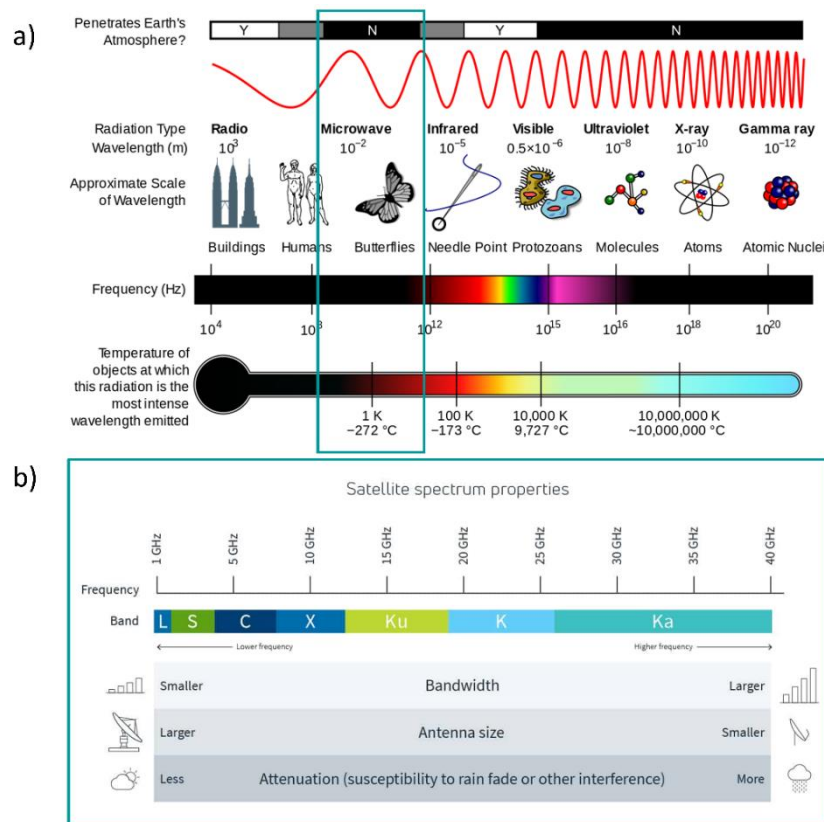
Figure 4.3. The electromagnetic spectrum in panel a) and microwave region sub-portion of interest in remote sensing application in panel b).

In general, interactions are higher when the wavelength and the dimension of the objects interacting with the radiation have similar magnitudes. For instance, L-band radiation is known to be more penetrating with respect to C-band radiation. In fact, L-band radiation is characterized by strong interactions with the vegetation macrostructure and by low interaction with small vegetation; conversely, C-band

radiation is not able to penetrate the vegetation cover because of strong interactions with the leaves.

In the active microwave remote sensing, a radar (Radio Detection And Ranging) system emits its own microwave radiation and the antenna measures the backscatter after the interaction between the signal and the target object. The backscatter is defined as the intensity of the signal scattering back to the sensor. The different backscatter entities recorded by the instrument allow to distinguish the different targets, while the time between the emitted and the received-back signal is useful to measure the distance from the target.

The scattering behaviour over a certain surface is mainly governed by its dielectric and geometric properties, while the backscattering is influenced by several factors, like the roughness of the target surface, the polarization, the dielectric constant of the surface characteristics, the soil moisture, the vegetation cover, the topography, the observation frequency, and the incidence angle (Schmugge, 1985; Su et al., 1996). In particular, in presence of vegetation, its contribution to the backscatter is determined by the sum of three terms, one linked to the direct backscattering from the plants, one referred to the direct backscatter from the soil, with canopy attenuation, and one due to multiple scattering between the plants and the soil.

The development of the SAR has opened new perspectives in radar applications. This technology allows to overcome a native radar issue, consisting in the inverse relation between the antenna length and the spatial resolution capability of the system. In a SAR system, a sequence of acquisitions obtained with an antenna of a certain length during its translation along the flight direction are properly combined together, thus simulating an acquisition by a much longer antenna.

Passive microwave remote sensing of soil moisture is based on measurements of the brightness temperature, which characterizes the intensity of the radiation emitted or reflected by the Earth's surface in the microwave portion of the electromagnetic spectrum, usually measured through a radiometer. In typical passive microwave applications, the brightness temperature mainly depends on the soil temperature. In order to estimate the soil moisture, the brightness temperature can be modeled through emissivity models or radiative transfer models. In emissivity models, the soil temperature is constant along the whole soil layer profile, while in radiative transfer models, the soil temperature varies along the different layers in which the soil is discretized. It is noteworthy that, the

brightness temperature depends on the vegetation cover and the surface roughness also.

4.1.2 Microwave Products

4.1.2.1 SMOS

The SMOS mission was launched by the European Space Agency (ESA) on November 2nd, 2009 (Kerr et al., 2010). The objectives of the mission were to collect surface soil moisture observations over the land with a target accuracy of 0.04 m³/m³ and measurements of salinity over the oceans. SMOS represents the second ESA's Earth Explorer Opportunity mission, developed in synergy with the Spanish *Centro para el Desarrollo Tecnológico Industrial* (CDTI) and the French *Centre National d'Estudes Spatiales* (CNES). SMOS has a revisit period of 3 days at the Equator, which is overpassed at 06:00 and 18:00 LST during the ascending and descending orbits, respectively.

The instrumentation aboard the SMOS satellite is an Y-shaped passive 2D interferometric radiometer operating at L-band frequency (1.4 GHz); the surface soil moisture is retrieved starting from multiangular observations of the brightness temperature collected by the antenna. The surface soil moisture data is retrieved through the Level-2 (L2) retrieval algorithm; auxiliary static (topography index, land use, soil texture) and dynamic (frost and thaw cycle, rainfall, temperature) data sets are exploited to produce the SMOS soil moisture product, which has a spatial resolution ranging from 35 to 50 km.

Both SMOS and SMAP radiometers operate in the protected frequency allocation of 1.4-1.427 GHz; despite this, problems due to Radio-Frequency Interference (RFI) in this protect band were found to affect SMOS observations. This issue helped the development of a special flight hardware to detect and filter RFI aboard the SMAP satellite.

In this work, a 1 km version of SMOS, obtained after downscaling the original coarse resolution data through the DISPATCH algorithm, has been used (Merlin et al., 2008).

4.1.2.2 SMAP

The SMAP mission, aimed to collect soil moisture observations and to monitor the freeze/thaw state at a global scale (Entekhabi et al., 2010), was launched by the

National Aeronautics and Space Administration (NASA) on January 31st, 2015. The revisit period of SMAP is of 2-3 days at the Equator, overpassed at 06:00 and 18:00 Local Solar Time (LST) during the descending and ascending orbits, respectively. The retrieved surface soil moisture has an accuracy of 0.04 m^3/m^3, thus accomplishing the mission targets (Colliander et al., 2017).

SMAP was originally designed to merge the benefits of active and passive remote sensing to improve the resolution of the retrievals obtained by the radiometer. For this reason, the native equipment was an L-band radiometer (1.4 GHz) and an L-band radar (1.26 GHz), which were expected to provide surface soil moisture measurements at 3 km, 9 km, and 36 km resolutions. Nevertheless, because of the premature fail of the radar in July 2015, only the 9 km and 36 km sampling version have been available during the post-radar phase. Recently, a 3 km version has been released (Das et al., 2019); this product is obtained by merging SMAP data with data retrieved by Sentinel-1A/Sentinel-1B, as Sentinel SAR-derived data has been identified as a suitable substitute of the observations that were originally supposed to be obtained through the SMAP radar.

The full name of 9 km sampling version is SMAP Level 2 Enhanced Passive Soil Moisture Product (L2_SM_P_E); the retrieval is based on the interpolation of the antenna temperature data in the SMAP original brightness temperature data through the Backus-Gilbert technique (Poe, 1990; Stogryn, 1978), followed by several calibrations and corrections (Chan et al., 2018).

In the analyses described in the presented thesis, the 9 km sampling version (O'Neill et al., 2016) and a 1 km resolution version obtained through the DISPATCH downscaling algorithm have been used.

4.1.2.3 Sentinel-1

The Sentinel-1 constellation consists of two identical satellites, Sentinel-1A and Sentinel-1B. The first one was launched on April 3rd, 2014, while the second one on April 25th, 2016. Sentinel-1 is the first of six missions developed by ESA for the European Earth Observation program, Copernicus.

The instrumentation aboard the Sentinel-1 spacecrafts is a single SAR operating at C-band frequency (C-SAR, 5.4 GHz). The two Sentinel-1 satellites have the same orbit and are 180° apart; their synergy, reached in 2016 when both the satellites became operational, ensures a coverage over Europe guaranteed with a revisit time of 1.5-4 days, but over the rest of the Earth the revisit time can drop up to 6

days. The C-SAR equipment aboard the Sentinel-1 satellites is able to collect observations in four different setups: the Interferometric Wide-swath mode (IW), the Wave Mode (WV), the Strip Map Mode (SM), and the Extra Wide-swath mode (EW). The main one over land, of interest for soil moisture, is the IW mode; in this setup, the Sentinel-1 C-SAR reaches a ground range detected (GRD) resolution of 20 m x 22 m (Bauer-Marschallinger et al., 2018).

In this work, two versions of Sentinel-1 soil moisture have been used. The first one is the Sentinel-1 Surface Soil Moisture (SSM) at 1 km delivered by the Copernicus Global Land Service. This product is obtained by adapting to high-resolution SAR data the change detection algorithm (Wagner et al., 1999; Hornáček et al., 2012), which was originally proposed by the Vienna University of Technology. The data is delivered as degree of saturation, i.e., ranging between 0 and 1. Furthermore, three masks are applied to the data set, one for pixels with low sensitivity, one for pixels with an excessive terrain slope, and one for pixels falling in water bodies. The second version of Sentinel-1 SSM used in this work has a plot scale resolution. The soil moisture maps at a plot scale are developed and delivered by a consortium led by the THEIA Data and Services Centre for Continental Surfaces. The soil moisture at a plot scale data set is obtained by merging Sentinel-1 SAR-derived data with observations from Sentinel-2 optical sensors. The maps are provided with a temporal resolution of 6 days and they are produced by applying over agricultural areas an inversion algorithm based on neural networks. The agricultural domain is obtained from several sources: the CLC, the THEIA Land Cover Scientific Expertise Centre (SEC), the French Registered Geographical Parcels data sets, and local land cover maps. Sentinel-2 images, after a correction for atmospheric effects, are used in the process chain to estimate soil moisture and to delimit homogeneous polygons to be extracted within the agricultural parcels' edges.

4.1.2.4 ASCAT

ASCAT is a real aperture active radar that uses vertically polarized antennas and whose operational frequency is the C-band (5.3 GHz). The instrument is on board of the EUMETSAT METOP (METeorological OPerational) satellites. The METOP series consists of three satellites launched in succession to ensure the continuity of the mission observations. The first one, METOP-A, was launched on October 19th, 2006; the second one, METOP-B, on September 17th, 2012, and finally METOP-C was launched on November 7th, 2018.

In its original design, ASCAT was not supposed to collect soil moisture observations, but wind speed and directions measurements over the oceans. Nevertheless, several studies focused on ESCAT, the precedent version of the instrument, showed the suitability of ASCAT in monitoring surface soil moisture (Pulliainen et al., 1998; Wen and Su, 2003; Wagner et al., 2007). The global coverage is reached by ASCAT every 1-3 days, while the Equator is crossed at 21:30 during the ascending pass and at 09:30 during the descending pass.

The ASCAT soil moisture product, delivered as degree of saturation and thus ranging between 0 and 1, is produced through the change detection algorithm developed by the Vienna University of Technology (Wagner et al., 1999; Bartalis et al., 2007; Naeimi et al., 2009; Wagner et al., 2013). The spatial resolution of the ASCAT data is 25 km. In this work, the H115 soil moisture product resampled on a 12.5 km grid has been used. The data set, available from 2007 to 2018, is delivered by EUMETSAT H SAF.

4.1.2.5 The DISPATCH Algorithm

The DISPATCH method (Merlin et al., 2008) allows to disaggregate the original coarse resolution surface soil moisture data to higher resolutions by merging with optical data. DISPATCH is an evaporation-based downscaling algorithm, which can be defined as both physically-based and theoretical (Peng et al., 2017). The downscaling process consists in a redistribution of the high-resolution product around the mean value of the related coarse resolution data. The disaggregation is possible by means of the partitioning of the evaporation part on the surface soil layer (first 5 cm) from the transpiration part in the root zone, which is attributable to the vegetation cover. In this way, the ratio of actual to potential evaporation, also known as the Soil Evaporative Efficiency (SEE), can be estimated over the bare soil. The spatial relation existing between the SEE and the near-surface soil moisture makes the abovementioned redistribution of high-resolution data around the average value of the original coarse resolution product possible. The temporal resolution of the outputs of this process is the same of the low-resolution input data. In the DISPATCH method, the SEE is calculated through two optical remotely sensed products, the land surface temperature data and the NDVI detected by the MODIS sensor on board of the Terra (EOS AM) and Aqua (EOS PM) satellites.

The main advantage of the DISPATCH algorithm is that in situ measurements are not required to disaggregate the original low-resolution data. A method's limitation is that its applicability is influenced by the cloudiness conditions (Peng et al., 2017), which affect the optical data necessary to realize the disaggregation. However, this limitation is overcome by the algorithm itself, which, in case of clouds coverage, keeps the soil moisture value of the input low-resolution data for the high-resolution pixel.

Merlin et al. (2013) compared three versions of SMOS soil moisture at 40 km, 3 km and 100 m with in situ observations aggregated at the same spatial scales. The 3 km and 100 m resolution versions were obtained through the DISPATCH algorithm. The analyses were carried out over pilot sites in Catalonia, an area studied also in the presented thesis. The authors highlighted a better representation of the spatio-temporal dynamics of soil moisture in terms of higher correlations with in situ measurements when using the downscaled products. In fact, the correlation between SMOS-derived and in situ soil moisture was equal to 0.59 for the 40 km resolution version, equal to 0.67 for the 3 km version, and equal to 0.73 and to 0.86 for two different configurations of the 100 m resolution product. Similar results were obtained by Malbéteau et al. (2015), which evaluated the performances of 1 km DISPATCH downscaled versions of SMOS and AMSR-E soil moisture against in situ data over the South East of Australia. An increase in the correlation during summer over a semi-arid region was highlighted (from 0.37 to 0.63 and from 0.47 to 0.73 for SMOS and AMSR-E in afternoon overpasses and from 0.63 to 0.78 and from 0.42 to 0.71 for SMOS and AMSR-E in morning overpasses). Molero et al. (2016) compared DISPATCH downscaled SMOS soil moisture with in situ observations under different climatic conditions, finding better correlation over semi-arid regions with respect to sub-humid areas.

4.1.3 Optical Products

The main application of optical products in the analyses described in this thesis can be found in the irrigation estimates framework, whose methodology is thoroughly described in Section 4.6.

The data used are the NDVI v2.2 and the FCover v2, which contains information of the portion of each 1 km x 1 km pixel covered by vegetation. Both products are delivered by the Copernicus Global Land Service with a spatial resolution of 1 km and a temporal frequency of 10 days; the indices are obtained after processing the

4. Materials and Methods

data observed by the SPOT-VEGETATION (*Satellite Pour l'Observation de la Terre –VEGETATION*) sensor and its successor PROBA-V (Project for On-Board Autonomy – Vegetation) according to the method explained in Sterckx et al. (2014). The VEGETATION instrument, on board of the SPOT 4 and 5 Earth observation missions, stopped working in May 2014 after 16 years of service. In order to continue the mission's observations, PROBA-V was launched by ESA in May 2013, with the new VEGETATION imaging instrument developed by adopting spectral channels close to those used in its precedent version. Detailed information about the PROBA-V mission are available in Dierckx et al. (2014).

The NDVI data vary between a physical range of (-0.08, 0.92), while the FCover data between a physical minimum of 0 (vegetation cover absent) and a physical maximum of 1 (fully covered by vegetation); validation reports are available at the Copernicus Global Land Service website: https://land.copernicus.eu/global/.

4.2 Meteorological Data

Ancillary meteorological data sets have been exploited to perform the analyses described in this thesis. Regarding the pilot site located within the Ebro river basin, the SAFRAN (*Système d'Analyse Fournissant des Reinsegnements Atmosphériques à la Neige*) meteorological analysis system has been used (Durand et al., 1993). SAFRAN exploits ground observations merged with a first guess coming from numerical weather prediction modeling into an optimal interpolation algorithm. The output of this process is a gridded data set of temperature, wind speed, rainfall rate, and other meteorological variables at 5 km spatial resolution, with hourly time step.

In the presented thesis, an updated version of the SAFRAN data set originally developed for Spain (Quintana-Seguí et al., 2016; 2017) with data until August 2014 has been used; in this new version, Portugal has been involved, hence, the whole Iberian Peninsula is covered and the data is available until August 2017. The code used is the same adopted for the implementation of SAFRAN in France, with minor changes (Quintana-Seguí et al., 2008; Vidal et al., 2010). In the adopted version, the modeling-derived first guess mainly comes from the ERA-Interim data set, with the only exception of the precipitation, which does not use a first guess. Ground observations are taken from AEMET (*Agencia Estatal de METeorología*) meteorological station network.

On the basis of the SAFRAN's outputs, a 5 km resolution gridded data set of potential evapotranspiration calculated according to the FAO Penman-Monteith method has been built. The data set covers the period from September 1st, 2010 to September 1st, 2017. As an example, Figure 4.4 shows the potential evapotranspiration calculated for the day September 15th, 2015. The data set has been produced by exploiting relative humidity, temperature, and wind speed data from SAFRAN; the solar radiation data, also necessary to calculate the potential evapotranspiration according to the FAO Penman-Monteith equation, has been taken from the ERA-5 reanalysis (Hersbach et al., 2020) and resampled to the finer SAFRAN's grid before the computations. Furthermore, rainfall rates produced by the SAFRAN system have been used as reference rainfall in the SM2RAIN elaborations carried out within the irrigation estimates framework, whose detailed explanation can be found in Section 4.6.
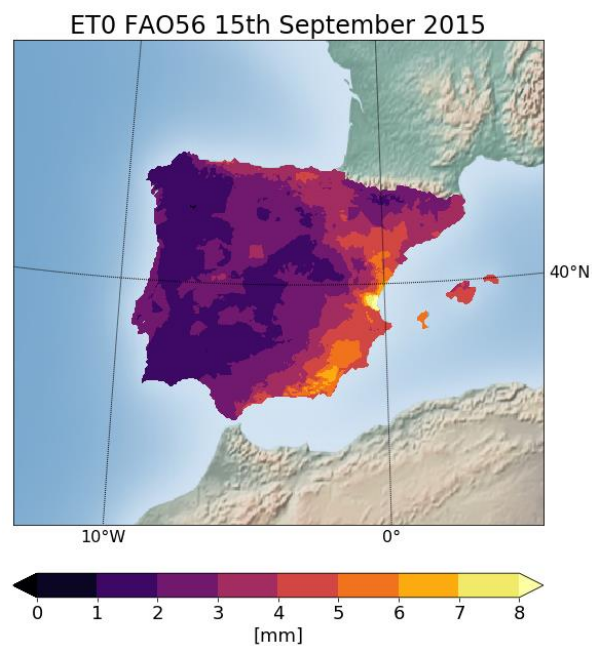
Figure 4.4. Example of the potential evapotranspiration calculated through the FAO Penman-Monteith equation and referred to September 15th, 2015. The data set, which has a spatial resolution of 5 km, has been built by exploiting atmospheric variables taken from SAFRAN and ERA-5. It covers the whole Iberian Peninsula for the period 2010-2017.

Regarding the Upper Tiber basin in Italy, only rainfall records from ground observations have been used as additional meteorological data set. The exploited stations are part of network used to monitor the Umbria region, to which the pilot

basin belongs almost entirely. The rain gauge network consists of more than 90 stations, which are shown in Figure 4.5.
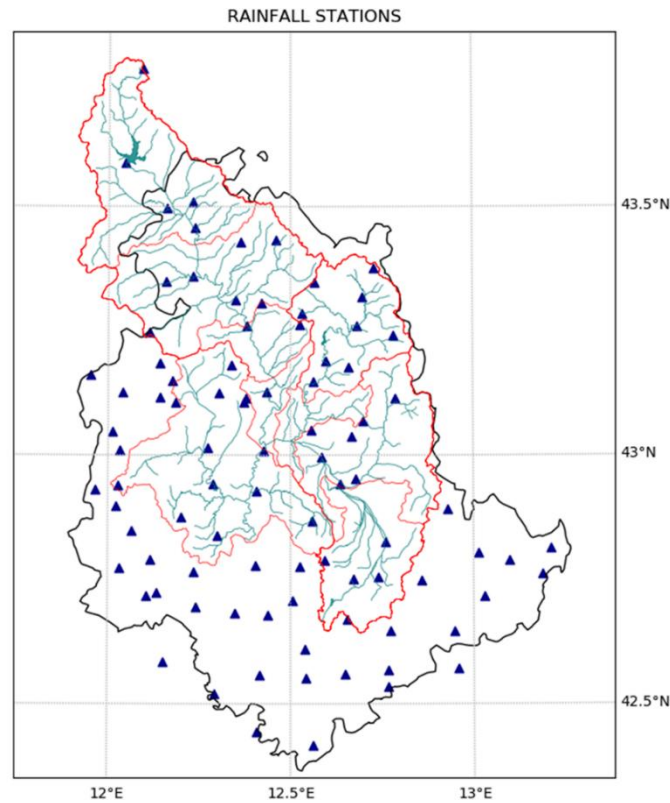
Figure 4.5. Rain gauge network of the Umbria region (central Italy), marked with black edges. The Upper Tiber basin is represented with red edges.

4.3 SURFEX Modeling Platform

This section describes the modeling aspects involved in the presented thesis. Simulations with a LSM have been carried out in order to build a data set of modeled soil moisture over the pilot areas to be used together with the remotely sensed data in the performed analyses. A short description of the SURFEX modeling platform (Masson et al., 2013) is provided in Section 4.3.1, while Section 4.3.2 describes the analyses performed over the two pilot areas.

4.3.1 Model Description

SURFEX is the surface modeling platform developed by Météo-France. SURFEX is composed of different and independent schemes that allow to calculate the exchange of fluxes (water, carbon, energy, snow, etc.) between the surface and the

atmosphere over four types of surfaces. Figure 4.6 shows a conceptualization of the modeling platform.
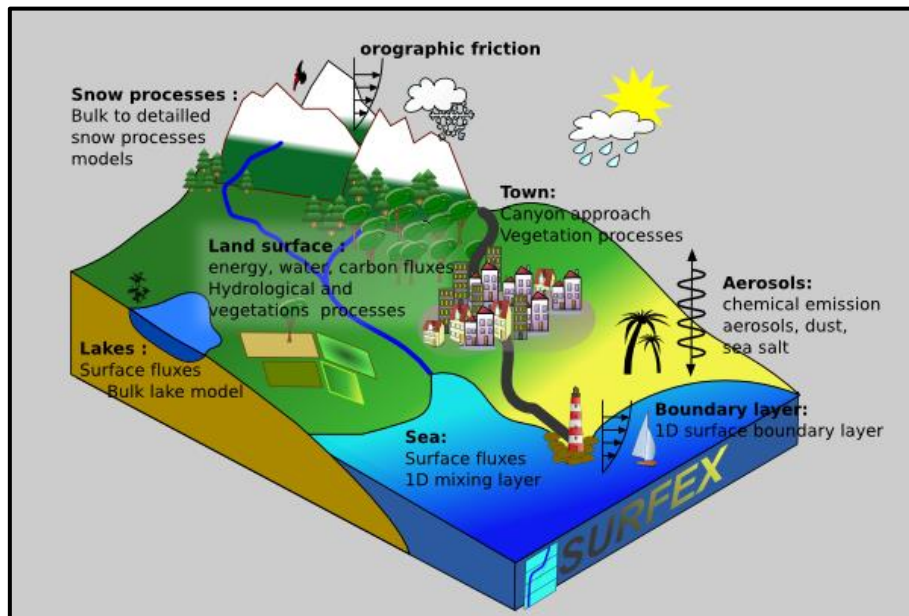
Figure 4.6. SURFEX modeling platform: modeled fluxes and their origin.[2]

SURFEX can be used in a stand-alone setting (offline mode), or it can be coupled with climate models and atmospherical models for numerical weather prediction. SURFEX can run at any user-defined spatial resolution; the heterogeneity existing within a generic pixel is taken into account through a tiling approach. The main tiles provided in the model are: natural surfaces, urbanized areas, inland water and oceans. For the natural areas, the ISBA scheme is used. Areas where towns exist are described by the Town Energy Balance (TEB) scheme; lakes and oceans are described through multiple approaches and models. Each tile of the generic pixel receives the same atmospheric forcing associated to that pixel; hence, for each tile present in the mesh grid, the fluxes are computed through the appropriate scheme. The fluxes are then aggregated and sent back to the atmosphere. It is noteworthy that, lateral flows are not considered. The distribution of water on the Earth's surface can be determined by post processing the SURFEX's runoff outputs for each cell through river routing models. The structure of the modeling platform, including some possible coupled settings, is shown in Figure 4.7.

---

[2] source: http://www.umr-cnrm.fr/surfex/
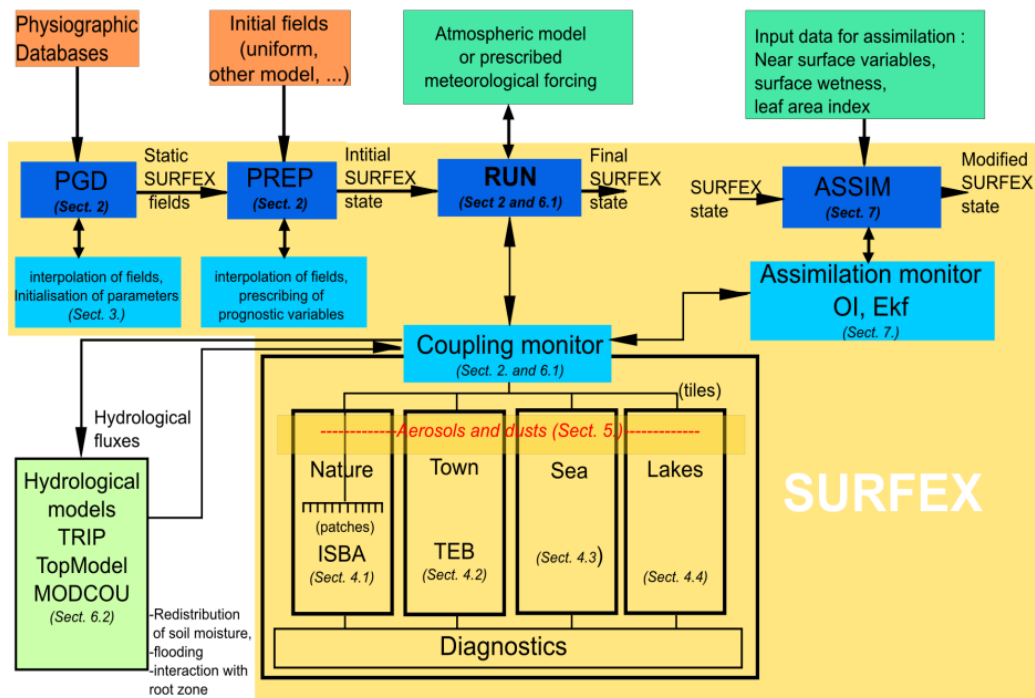
Figure 4.7. Flow chart showing the SURFEX's structure, involving several coupling options (taken from the material of the SURFEX training course).[3]

In the performed analyses only the ISBA scheme has been used, since natural surfaces only have been simulated. ISBA (Noilhan and Planton, 1989; Mahfouf and Noilhan, 1996; Noilhan and Mahfouf, 1996) incorporates multiple algorithms to estimate the exchanges of water and energy between the soil-vegetation-snow continuum and the atmosphere, which have been updated in time (Boone et al., 1999, 2000; Habets et al., 2003). Within the ISBA scheme, the surface is divided in patches linked to the land cover. Several versions of ISBA exist, that can be chosen before the simulation; they essentially differ in terms of the structure of the temperature and hydrology profiles modeled. In this thesis, simulations have been carried out by adopting the latest version of the model, SURFEX v8.1, which has been obtained from the *Centre National de Recherches Météorologiques*. The ISBA-DIF scheme has been used; in this version, the soil is divided in 14 layers by default and the root zone depends on the vegetation.

---

[3] http://www.umr-cnrm.fr/surfex/spip.php?article423

4.3.2 Land Surface Simulations

The simulations have been carried out at 1 km resolution over both pilot sites. The adopted resolution is rather unusual, as the model is often ran at coarser spatial resolutions. Because of the computational effort required to run the model at high spatial resolution, over the Spanish pilot site, not the whole Ebro basin, but the area enclosed between two sub-catchments (identified by the Cinca and Segre rivers) only, has been simulated. The domain has been chosen in such a way as to cover the area where irrigation occurs (see Figure 4.8). The simulation over the Spanish case study covers the period ranging from 01/09/2010 to 01/09/2018, while the simulation over the Italian site covers the time span from 01/09/2010 to 01/09/2019.
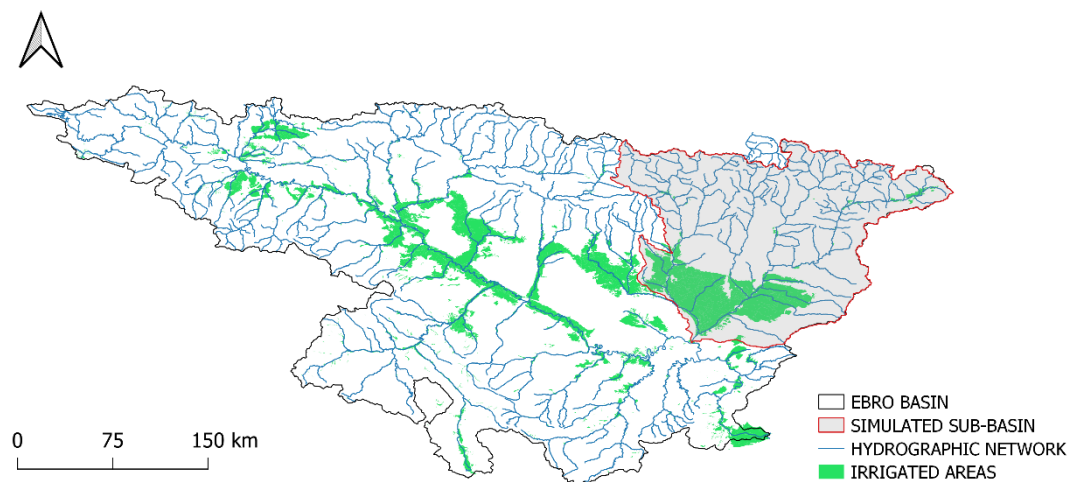
Figure 4.8. Portion of the Ebro basin simulated with SURFEX: area enclosed between the Cinca and Segre sub-basins, which is represented with red edges and shaded in grey.

Over the pilot site in Italy, it has been possible to simulate the whole basin. For the simulation over the Spanish pilot site, a regular 1 km grid of 208 × 173 pixels has been adopted; for the Upper Tiber basin, the grid has the same spatial resolution and consists of 89 × 136 cells. The panel a) of the Figures 4.9 and 4.10 show the overlap of the adopted grids with the Spanish and the Italian pilot sites, respectively. It is noteworthy that, the same spatial grids have been adopted for all the analyses presented in this thesis; hence, all the spatially distributed data sets used (observed data, modeled data, ground truth data) have been resampled to the SURFEX-ISBA grids before the analyses. The land cover map used for the simulations is ECOCLIMAP II (Faroux et al., 2013); it is the default one for SURFEX

and has a spatial resolution of 1 km. The model has been forced with atmospheric forcing from the ERA-5 reanalysis (Herbach et al., 2020) provided by the European Centre for Medium-Range Weather Forecast (ECMWF) and downloaded from the Copernicus Climate Data Store. In order to run SURFEX-ISBA, the following atmospheric variables are needed at an hourly time step: 2 m air temperature and relative humidity, downward visible and infrared radiation, precipitation, and wind speed. Despite the input atmospheric data being at an hourly time step, the model has a higher resolution internal step of 15 minutes. The data has a spatial resolution of 0.25° × 0.25°. Hence, before the simulations, the input atmospheric data have been resampled to the 1 km grids adopted. In addition, in order to solve possible vertical mismatches between the high-resolution relief implemented in SURFEX (GTOPO30) and the coarser resolution relief of ERA-5, a lapse rate correction to relative humidity and temperature has been performed. The advantages in forcing ISBA simulations with atmospheric data from the ERA-5 data set have been discussed in Albergel et al. (2018). In particular, input from ERA-5 proved to enhance the characterization of variables involved in the terrestrial hydrological cycle, e.g., soil moisture.

For both the simulations carried out, the adopted vegetation scheme is determined by the climatology of the Leaf Area Index (LAI); hence, the vegetation is the same every simulated year.

In the presented thesis, the SURFEX-ISBA simulations have been performed with the aim of building a modeled data set of soil moisture not taking into account of irrigation to be used, as a negative benchmark, together with remotely sensed data in the irrigation detection activity. The modeled surface soil moisture used in the analyses is obtained from the weighted average of the first two layers of the soil parametrization and it is representative of the first 4 cm of the soil. Although only the soil moisture has been actually used in the analyses, it is not the only output that has been kept; in fact, several output variables have been saved to be used in further analyses or in future studies linked to this thesis. Table 4.1 provides the list of the SURFEX-ISBA outputs that have been kept. Note that they are the same for both the simulations carried out.
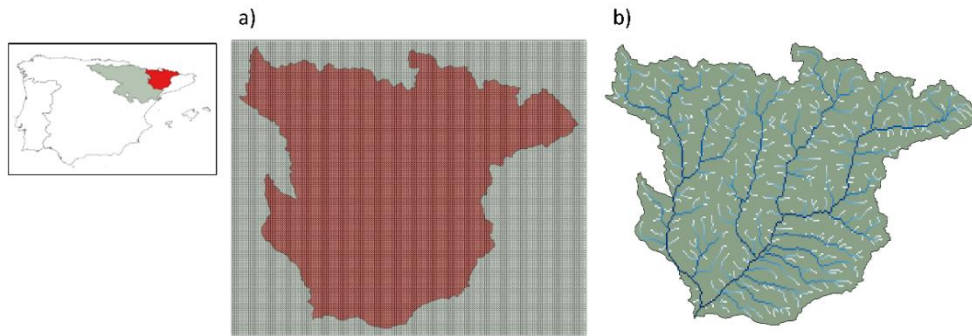
Figure 4.9. Area enclosed between the Cinca and the Segre sub-basins: a) the 1 km regular grid adopted for the SURFEX-ISBA simulations, b) the river network.
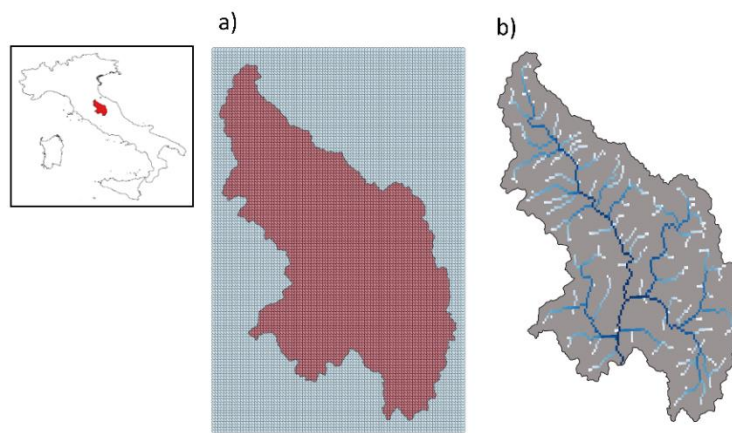
Figure 4.10. The Upper Tiber basin: a) the 1 km regular grid adopted for the SURFEX-ISBA simulations, b) the river network.

Finally, the river network has been implemented for both the study areas and it is shown in panel b) of Figures 4.9 and 4.10. The coupling is necessary to simulate river flow, as SURFEX only provides runoff and drainage rates for each grid cell as an output. Hence, these outputs need to be delivered to the river in order to compute river flow. This task has been addressed in the perspective of a future coupling with the RAPID (Routing Application for Parallel computatIon of Discharge) river routing model (David et al., 2011) within the Eaudyssée modeling platform. This coupled configuration is the SASER (SAfran-Surfex-Eaudyssèe-Rapid) hydrological model. For both study areas, the river network has been built by processing information on the DEM and on the flow direction and accumulation from the HYDROSHEDS (HYDROlogical data and maps based on SHuttle Elevation Derivaties at multiple Scales) data set. This procedure allowed to reconstruct the confluence order of the river network cells.

An example of the model's output is provided in Figure 4.11, which shows the spatial distribution of the mean surface soil moisture referred to the year 2016 over the pilot basin, obtained from the weighted average of variables WG1P1 and WG2P1 of Table 4.1.

Table 4.1. Output variables from the SURFEX-ISBA simulations that have been saved.

Name	Description	Unit
LEGC_ISBA	Bare ground evaporation for the tile nature	W/m^2
LEVC_ISBA	Total vegetation evaporation for the tile nature	W/m^2
EVAPC_ISBA	Total evaporative flux for the tile nature	kg/m^2/s
DRAINC_ISBA	Drainage for the tile nature	kg/m^2/s
RUNOFFC_ISBA	Runoff for the tile nature	kg/m^2/s
SNOMLTC_ISBA	Snow melting rate	kg/m^2/s
WG1PI	Soil moisture in the first soil layer	m^3/m^3
WG2P1	Soil moisture in the second soil layer	m^3/m^3
WG3P1	Soil moisture in the third soil layer	m^3/m^3
TS_ISBA	Total surface temperature over the tile nature	K
SWI1_ISBA	Soil wetness index in the first soil layer	-
TSWI1_ISBA	Total soil wetness index (liquid + solid) in the first soil layer	-
SWI2_ISBA	Soil wetness index in the second soil layer	-
TSWI2_ISBA	Total soil wetness index (liquid + solid) in the second soil layer	-
SWI3_ISBA	Soil wetness index in the third soil layer	-
TSWI3_ISBA	Total soil wetness index (liquid + solid) in the third soil layer	-
TSWI_T_ISBA	Total soil wetness index in the whole soil column	-
PSNG_ISBA	Snow fraction over ground averaged over the tile nature	-
PSNV_ISBA	Snow fraction over vegetation averaged over the tile nature	-
PSN_ISBA	Total snow fraction over the tile nature	-
WGTOT_T_ISBA	Total water content	kg/m^2/s
DSN_T_ISBA	Total snow depth	m
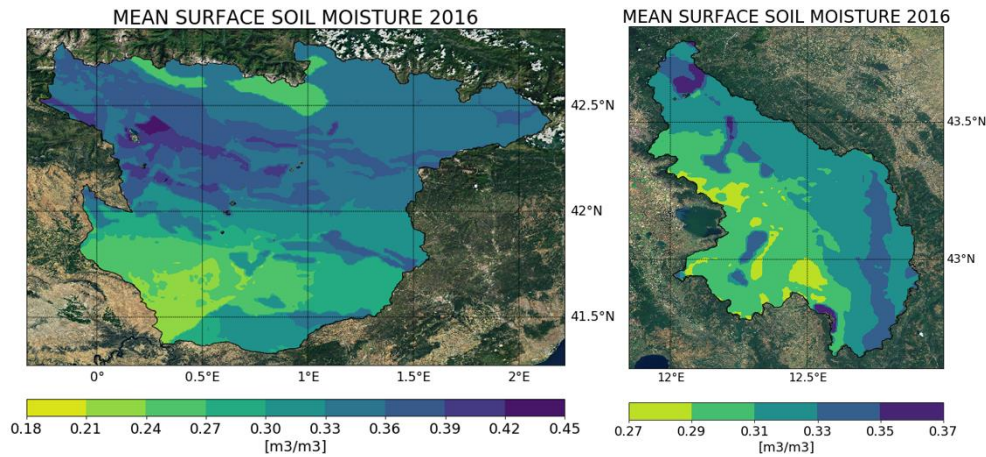
Figure 4.11. Example of SURFEX-ISBA model output: mean surface soil moisture in 2016 over the two pilot basins in the Spanish focus area (left side) and in the focus area in Italy (right side).

4.4 Ground Truth Data Sets

In this section, the ground truth data sets exploited as a benchmark to validate the proposed methodologies to map irrigation and to quantify how much water is used for this purpose are described. As explained in Chapter 3, the Ebro basin is a data rich area in terms of irrigation. For this area, detailed information on where irrigation occurs and on how much water is used for these practices is easily available. Conversely, for the Upper Tiber basin, it has been possible to collect only confidential information about irrigation practices occurring over selected pilot fields.

4.4.1 Information on the Irrigation Extent

For the pilot area within the Ebro basin, the ground truth data set on the spatial occurrence of irrigation is the map of crops in Catalonia. It is an open access database produced on the same spatial domain of the SIGPAC, delivered by the *Department d'Agricultura, Ramaderia, Pesca i Alimentació*. The source of the information contained in the maps of crops is the DUN (*Declaració Unica Agrària*), a mandatory document describing the agricultural activities that each owner of productive parcels must provide each year. In order to create the geospatial information, the DUN is integrated with the agricultural parcels data produced by SIGPAC. Prior to their publication, the maps of crops are optimized through some corrections. All the non-agricultural areas (i.e., pastures, unproductive areas, forests, urbanized areas) are masked out. Furthermore, parcels with incomplete

DUN documentation, as well as those with extensions lower than 50 m² are discarded; finally, occasional complex geometries are simplified. It is noteworthy that, the combined effects of the abovementioned correction produce a reduction in the declared area by less than 1%. The resulting maps provide, for each field, the extension, the geographic and administrative localization, the kind of crop, and the irrigation coefficient (a binary irrigated/non-irrigated information). The data set is available at: http://agricultura.gencat.cat/ca/serveis/cartografia-sig/aplicatius-tematics-geoinformacio/sigpac/mapa-cultius/. It is noteworthy that the ground truth data are characterized by a few shortcomings, mainly attributable to incomplete declarations provided in the DUN document; in fact, it may happen that when two crops are planted during the same year (e.g., winter cereals and summer cereals), only one of them is declared. Also, sometimes it happens that irrigation is declared but not performed over a certain parcel.

For the Upper Tiber basin in Italy, only scattered confidential information on a few pilot fields has been collected. Hence, an organized and detailed geospatial data set of irrigation ground truth is not available.

4.4.2 Benchmark Irrigation Volumes

Benchmark irrigation volumes applied over the districts in the pilot area in Spain have been collected from several sources. The main one is the database of the volumes of water flowing through the irrigation canals network supplying water to the districts. This kind of data is provided by the Automatic Hydrologic Information System of the Ebro river basin (SAIH Ebro), available at: http://www.saihebro.com/saihebro/index.php?url=/datos/canales. Figure 4.12 provides an overview on the SAIH portal and on the available data.

For the Pinyana district, the only one not belonging to the SAIH system, monthly volumes of irrigation water have been provided by the canal's technical office. Another alternative source of benchmark irrigation amount is the hydrological plan of the Ebro basin, which provides yearly cumulated estimates determined on the basis of a twelve-years collection of historical data, from 2000 to 2012.

Regarding the Upper Tiber basin, the data on the irrigation amounts and on the kind of crop for four pilot fields, two within the Upper Tiber area and two within the Left Tiber area, have been collected. The location of the fields, as well as the kind of cultivated crop, are shown in Figure 4.13.
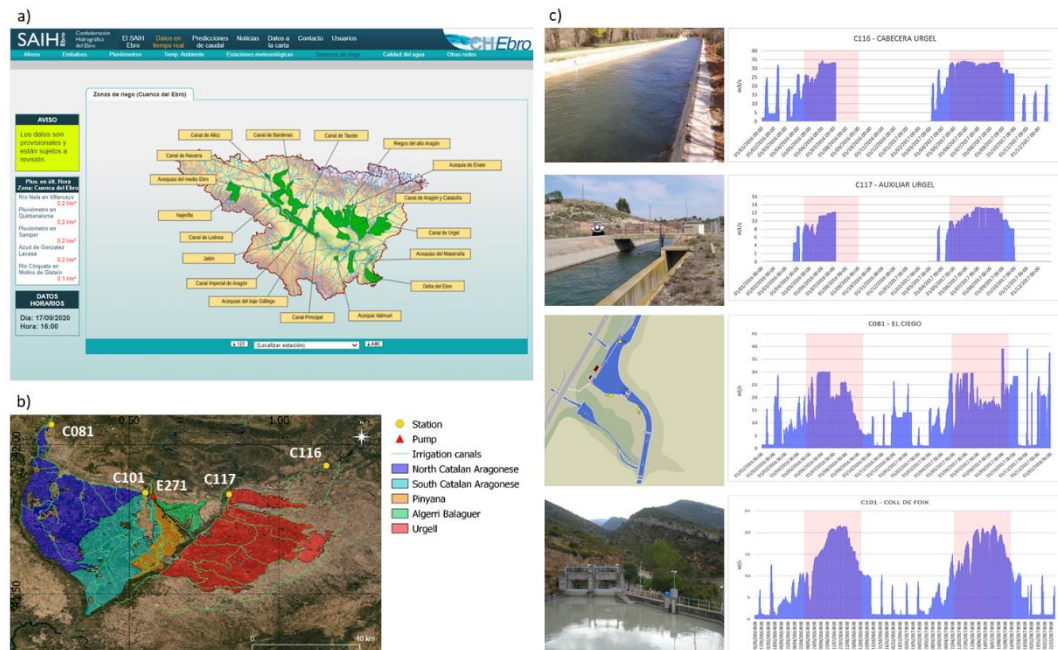
Figure 4.12. The SAIH system: a) irrigation data page interface, b) study area and considered stations, c) example of data from some of the stations used.

The data in the Upper Tiber domain covers the period 2017-2019. The UT1 pilot field has been irrigated in 2017 and 2018. Wheat has been planted but not irrigated in 2019. In 2017 and 2018, the crop types have been tobacco and maize, respectively. Conversely, the pilot field UT2 has not been irrigated in 2017, but in 2018 and 2019. Sunflower has been cultivated in 2017, while tobacco in 2018 and 2019. For the plots in the Left Tiber area, only the data for 2019 is available; the both pilot fields have been irrigated, tobacco has been planted in LT1 while pea in LT2.

It is noteworthy that, while in the pilot area in the Ebro basin a district scale information has been exploited, for the Upper Tiber basin a plot scale information has been considered.
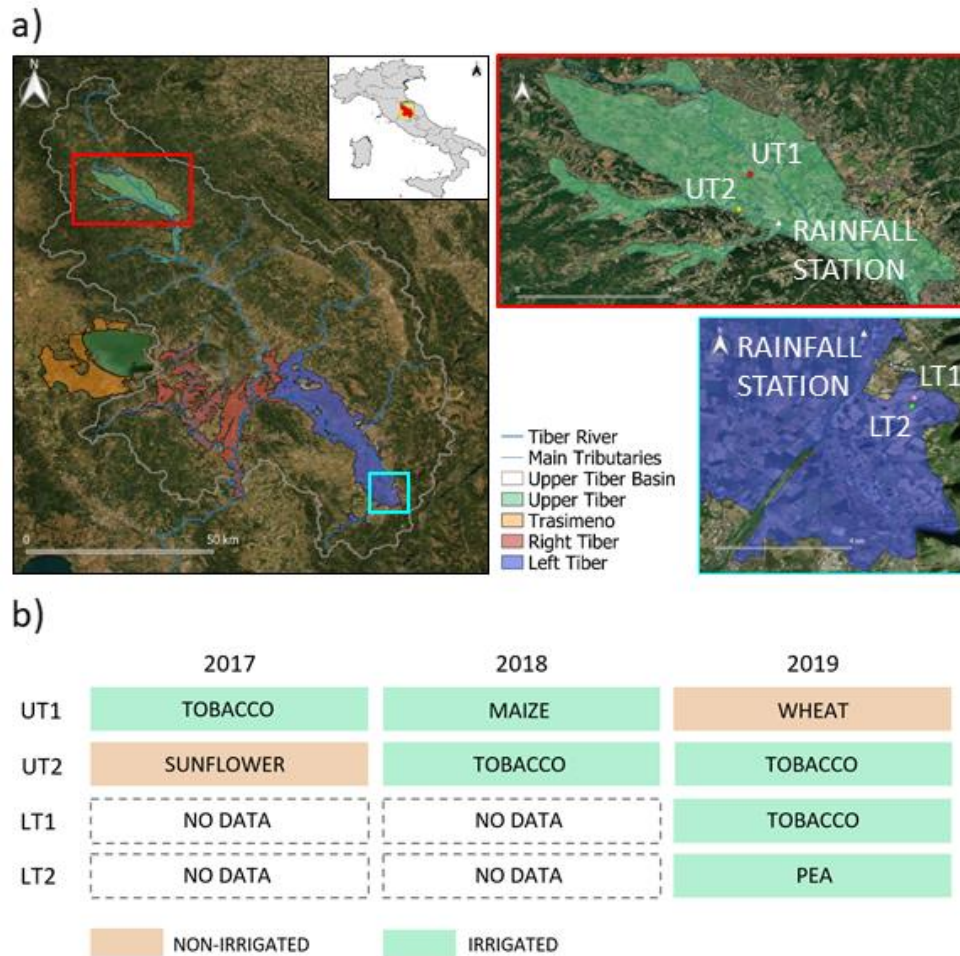
Figure 4.13 Pilot fields in the Upper Tiber basin for which irrigation amounts have been collected: a) location with respect to the whole study area, b) kinds of crops and related binary information on irrigation (irrigated/non-irrigated). Adapted from Dari et al. (2021b).

4.5 Methodology for Detecting and Mapping Irrigation

In this section, the theories at the basis of the methodology developed to detect and map irrigated areas over the two considered pilot sites at different spatial resolutions through remotely sensed soil moisture are described. Within this framework, the major novelty proposed in this thesis is to exploit under a new perspective the indices derived from the temporal stability theory, a well-established technique widely used to optimize the in-situ monitoring of soil moisture. In fact, the temporal stability theory allows to calculate indices describing the spatio-temporal behaviour of soil moisture; hence, they can be used to detect if particular irrigation-related patterns occur under certain conditions. The activity aimed to the irrigation mapping carried out in the Spanish pilot site

consists of two main phases. The flow chart describing the methodology adopted to produce maps of irrigated areas over this domain through remote sensing soil moisture is provided in Figure 4.14. In the first step, the capability to detect irrigation of several remote sensing soil moisture products has been assessed through the temporal stability derived indices. The data sets used are DISPATCH downscaled versions of SMOS and SMAP at 1 km, SMAP at 9 km, Sentinel-1 at 1 km, and ASCAT at 12.5 km. The surface soil moisture simulated at 1 km resolution by SURFEX-ISBA has been used as a support for the analyses. In the second step, maps of irrigated areas referred to the periods May-September 2016 and 2017 have been produced through the K-means algorithm; the best performing products arising from the first phase have been exploited for this purpose. The resulting maps have been validated according to two different validation procedures.

Over the Upper Tiber area, which is characterized by a more complex topography than the pilot area in Spain, a double-scale analysis on the detectability of irrigation through remote sensing soil moisture has been performed. The temporal stability derived indices have been exploited to assess if 1 km resolution is enough to spot where irrigation occurs in such a complex domain; hence, soil moisture data at a plot scale has been used as an input for the K-means clustering algorithm to develop maps of irrigated/not irrigated fields for the periods June-September 2017, 2018, and 2019. In the analysis at 1 km spatial resolution the data sets used are SMAP downscaled through the DISPATCH algorithm, the Sentinel-1 product delivered by the Copernicus Global Land Service, and the Sentinel-1 product delivered by THEIA at a plot scale resolution and aggregated at 1 km; furthermore, surface soil moisture at 1 km simulated with SURFEX-ISBA has been used as additional data sets. In the analysis at a plot scale resolution, the Sentinel-1 soil moisture data developed by THEIA and aggregated at 100 m resolution has been used.

The results of the analyses aimed at detecting and mapping irrigation extents performed in this thesis are presented and widely discussed in Chapter 5.

In the following, the temporal stability theory, the K-means algorithm, and the validation procedures adopted within this framework are explained.
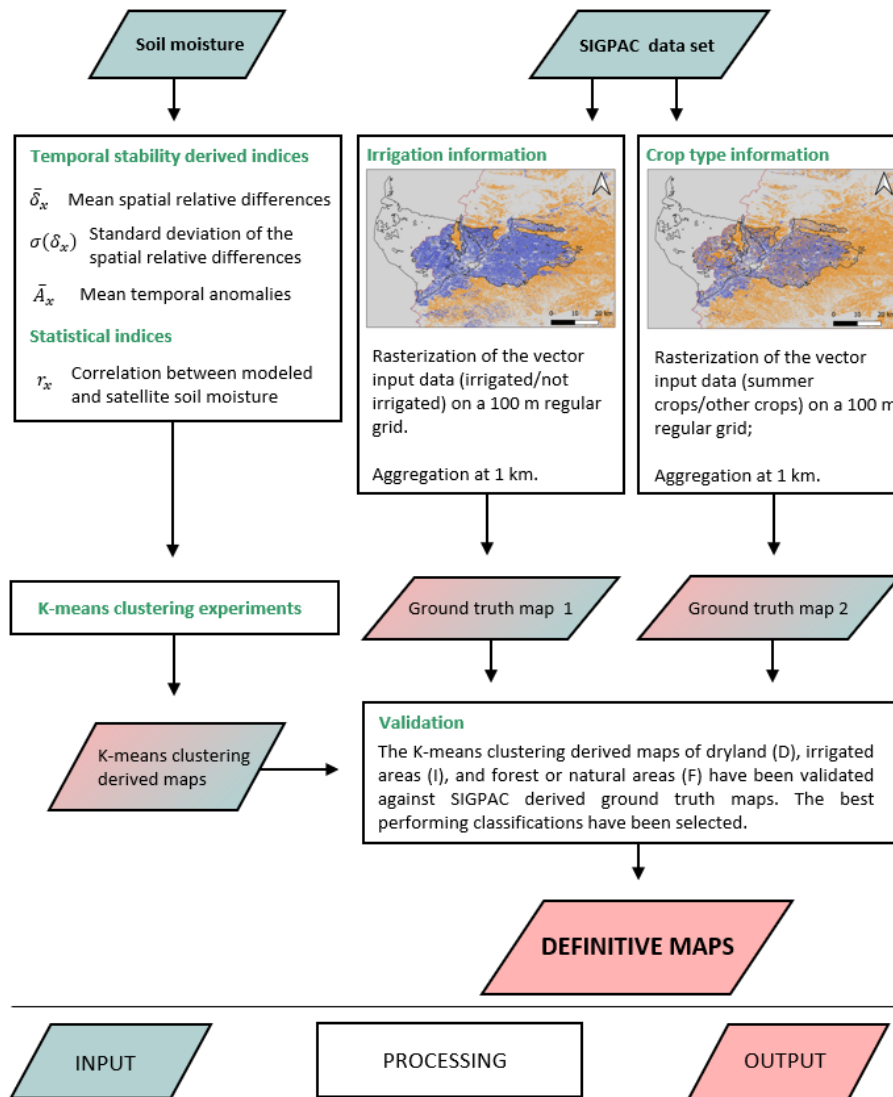
Figure 4.14. Flow chart describing the proposed methodology to map irrigated areas in the pilot site located within the Ebro basin, in Spain (Dari et al., 2021a).

4.5.1 Temporal Stability Theory

The temporal stability theory was originally proposed by Vachaud et al. (1985). The method has been widely used to optimize the soil moisture monitoring; in fact, through the relative differences approach, it is possible to find optimal measurement points, representative of the average wetness of the whole monitored area. Obviously, this aspect is of paramount importance for the in-situ monitoring of large areas, as it allows to reduce waste of time, energy, and fatigue. Several studies adopted the temporal stability methodology to optimize soil moisture monitoring at several spatial scales (Brocca et al., 2010; Gao et al., 2015;

63

Dari et al., 2019). Recently, Morbidelli et al. (2019) investigated the possibility of adopting the same techniques to optimize the rain gauge network design. In this work, the indices at the basis of the theory are exploited under a new perspective, aimed to evaluate the capability of remotely sensed soil moisture products to detect irrigation signals. The idea mainly relies on the capability of the temporal stability derived indices to express the spatial and temporal dynamics of soil moisture.

Let θ_{xt} be the soil moisture value at a certain pixel x of a grid at the observation day t. By indicating, for each day, the spatial mean referred to the entire considered area with $\bar{\theta}_t$, the relative differences for each pixel and for each observation day, δ_{xt}, are expressed by:

$$\delta_{xt} = \frac{\theta_{xt} - \bar{\theta}_t}{\bar{\theta}_t} \tag{4.2}$$

the temporal mean, $\bar{\delta}_x$, and the standard deviation, $\sigma(\delta_x)$, of the relative differences can be calculated for each pixel x by the following Equations (4.3) and (4.4), respectively:

$$\bar{\delta}_x = \left(\frac{1}{T}\right)\sum_{t=1}^{T}\delta_{xt} \tag{4.3}$$

$$\sigma(\delta_x) = \sqrt{\left(\frac{1}{T-1}\right)\sum_{t=1}^{T}\left(\delta_{xt} - \bar{\delta}_x\right)^2} \tag{4.4}$$

in which T is the total number of observation days considered.

In the canonical applications of the temporal stability theory, measurements points showing $\bar{\delta}_x$ close to 0 and low values of $\sigma(\delta_x)$, are chosen as optimal points, as they provide soil moisture observations stably representative of the mean areal value. For instance, Dari et al. (2019) applied this methodology to a data set of soil moisture observations collected during 23 measurements campaigns at 20 pilot sites within a catchment with heterogeneous topography located in the Umbria region (central Italy). The authors found that, during wet periods, just one optimal point was enough to represent the mean value of an area of ~500 km² with R² = 0.857 and RMSE = 1.2% vol/vol; during dry periods, the catchment-mean soil wetness conditions were reproduced with R² = 0.846 and RMSE = 1.6% vol/vol by exploiting two optimal points concurrently. The main results of the study by Dari et al. (2019) are summarized in Figure 4.15.

The relative difference is an index describing the spatial variability of soil moisture. Mittelbach and Seneviratne (2012) proposed an alternative perspective focused on the temporal dynamics of soil moisture. In order to quantify the

deviation of the soil moisture at a certain pixel x from its temporal mean, the temporal anomalies, A_{xt}, can be calculated as:

$$A_{xt} = \frac{\theta_{xt} - \bar{\theta}_x}{\bar{\theta}_x} \tag{4.5}$$

in which $\bar{\theta}_x$ indicates the temporal mean calculated for the pixel x. The spatial and the temporal mean of the anomalies are indicated with $\bar{A}_x$ and $\bar{A}_t$, respectively.

The temporal stability theory provides indices able to express how a soil moisture data set varies both in space and time. For this reason, in this research, the spatial relative differences and the temporal anomalies have been used to evaluate the capability of remotely sensed soil moisture product to detect irrigation over the pilot areas at different spatial scales. Hence, a new application for key variables of a well-established theory born for other purposes has been found. Furthermore, the temporal stability derived indices have been also exploited as input parameters for mapping irrigated areas through the K-means clustering algorithm, which is described in the following section.
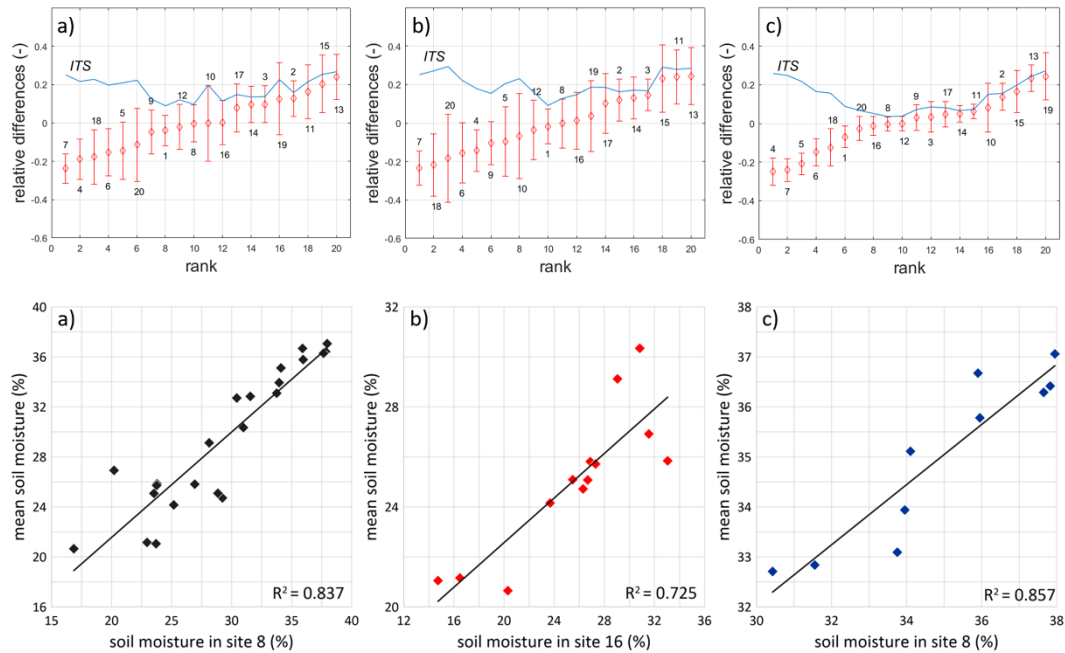
Figure 4.15. Main results obtained by Dari et al. (2019). In the upper panel, the mean (markers) and the standard deviation (vertical bars) for the 20 measurement points referred to: a) the whole measurement campaign, b) dry periods, and c) wet periods. In the lower panel, the areal mean is compared with the optimal points during: a) the whole period, b) the dry periods, and c) the wet periods.

4.5.2 The K-means Algorithm

K-means is a well-known clustering algorithm that allows the grouping of n data points into k clusters on the basis of precise input data features. The algorithm is thoroughly described in MacQueen (1967); it delimits each cluster by assigning a centroid that is determined through an iterative process starting with a random choice among the available input data. The grouping is performed by assigning each data point to the nearest centroid. In this way, clusters of data point with the same features are identified. The method is based on the minimization of the Euclidian distance, d, between the input vector of the data points and the vector of the centroids, calculated as:

$$d = \sum_{i=1}^{k} \sum_{j=1}^{n} \|x_j - C_i\|$$ (4.6)

in which x_j is the j-th element of the input data vector, with $j = 1, ..., n$, while C_i is the i-th element of the centroids vector, with $i = 1, ..., k$.

In this work, the K-means algorithm has been used in different configurations to produce maps of irrigated areas at different spatial scales over the two pilot areas. More in detail, in the analysis performed over the pilot area in Spain, the algorithm has been used to classify three different kinds of surfaces by exploiting remotely sensed and modeled soil moisture as input. Maps of the actually irrigated areas, the dryland, and forest or natural areas have been produced at 1 km spatial resolution. Hence, three clusters have been considered. In order to group the data according to the clusters, four sets of features have been used. The first one consists in the standard deviation of the spatial relative differences and the mean temporal anomaly calculated for the remote sensing soil moisture, in the second one the mean of the spatial relative differences and the mean of the temporal anomalies have been exploited; in the third one, the correlation between the modeled and the remotely sensed soil moisture has been added to the features used in the first set. Similarly, in the fourth set, the correlation has been added to the input data already used in the second set. In all the clustering experiments carried out, all the input features exploited are referred to the period when irrigation mainly occurs over the pilot area, i.e., from May to September of each considered year.

Over the pilot area in Italy, the K-means algorithm has been used to produce binary maps of irrigated or non-irrigated areas at a plot scale. Hence, only two clusters have been considered over this domain. Furthermore, only one set of features has been used as input for the clustering, composed by the mean of the

spatial relative differences and the mean of the temporal anomalies, both calculated over the highest irrigation intensity period of the pilot area, i.e., from June to September of each considered year.

4.5.3 Validation

Regarding the irrigation mapping activity carried out over the pilot area in the Ebro basin, maps of the three prevalent classes detectable, i.e., dryland (D), forest or natural areas (F), and irrigated areas (I) have been produced for the periods May-September 2016 and 2017. The maps have been validated according to two alternative validation procedures described in the following. They differ from each other for the kind of information contained into the SIGPAC crops maps data that has been considered to derive the benchmark ground truth maps; in fact, in the first validation the irrigation coefficient information is considered, while in the second one the attribute referred to the kind of crop has been exploited. As explained in Section 4.4.1, the SIGPAC crops maps are produced for the Catalonia autonomous community only, while the study area belongs to a lesser extent to the Aragon autonomous community also; hence the validation procedures have been performed over an area equal to the 71% of the total.

For both the validations carried out, the SIGPAC data have been pre-processed. In the first validation procedure, benchmark maps of dryland (D), forest or natural areas (F), and irrigated areas (I) have been produced starting from the irrigation attribute. It consists of a binary information (irrigated/not irrigated) for each parcel of the domain. The SIGPAC data set was born at a plot scale resolution; hence, as a first step, this information has been projected on a 100 m regular grid. As a result of this procedure, maps at 100 m resolution of irrigated and non-irrigated pixels have been obtained. The portions where the data set is not available have been interpreted as forest or natural areas pixels. In fact, the SIGPAC data is produced on agricultural areas only, after masking out natural areas, urbanized areas, and water bodies. This issue is not expected to introduce errors, as in the proposed method urban areas and water bodies are masked out before the validation. As a second step, the 100 m resolution maps have been aggregated at 1 km resolution on the grid adopted for the SURFEX-ISBA simulation. In this step, the predominant class among those of the 100 m × 100 m contained in a 1 km × 1 km pixel has been assigned to the latter. A supplementary condition has been considered for disentangling the dryland from the forest or natural areas: a 1 km × 1 km pixel has been considered as forest or natural area only in case of a

predominant kind of 100 m x 100 m pixels contained in it with this attribute and in double quantity compared to the dryland pixels. This additional constraint has been adopted to assign a homogeneous class to complex areas, e.g., the dryland portion in the South of Urgell, where shrubs, forest, and olive trees are highly mixed together and difficult to distinguish.

The choice of performing a second validation is led by considerations on the SIGPAC classification between irrigated/not irrigated used for the first validation procedure. Actually, this partition is referred to the possibility of a certain field to be reached by the irrigation infrastructure, but this condition does not ensure that the field is actually irrigated (e.g., it may happen that the field irrigation instrumentation is not installed). Hence, a second validation exploiting another kind of information contained in the SIGPAC data set has been performed. It is the attribute referred to the kind of cultivation. Crops that for sure are irrigated in the period of interest (May - September) have been considered: forage, summer cereals, and fruit trees. From this perspective, the parcels with the selected crops have been considered as irrigated, those with other crops have been treated as dryland, and finally the remaining portions have been considered as forest or natural areas. Starting from this partitioning of the SIGPAC data at a plot scale, benchmark maps at 1 km resolution have been developed according to the same procedure previously described for the first validation method. Figure 4.16 shows the different kinds of information contained in the SIGPAC data set exploited to perform the two validations.
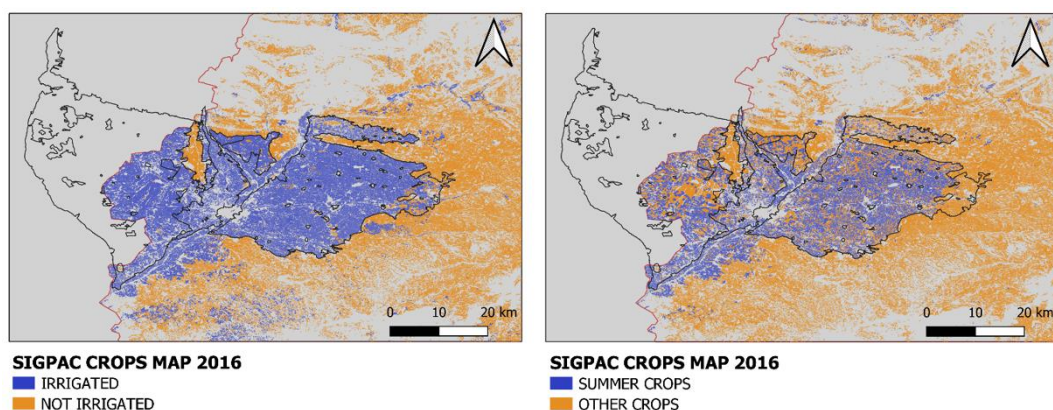
Figure 4.16. SIGPAC-derived information on the irrigation coefficient (left side) and the kind of crops (right side) adopted in the first and the second validation procedures, respectively. The data set is available for Catalonia only, whose edges are marked in red.

4.6 Methodology for Estimating Irrigation Amounts

This section describes the method developed to retrieve the amounts of water applied for irrigation. It is noteworthy that the approach has been applied over the pilot site in the Ebro basin only.

Within this framework, two irrigation-estimate experiments have been carried out at a spatial resolution of 1 km: one exploiting DISPATCH downscaled SMAP data and another one using DISPATCH downscaled SMOS data. The SMAP experiment covers the period from January 2016 to September 2017, while an extension back to January 2011 has been possible with the SMOS experiment. By merging the two experiments, a data set of almost seven years of estimated irrigation from remotely sensed soil moisture has been built.

The irrigation water amounts have been obtained through a modified version of the SM2RAIN algorithm (Brocca et al., 2014; 2015; 2016), originally developed to estimate rainfall from soil moisture variation as input and later adapted to retrieve irrigation (Brocca et al., 2018). In this thesis, a finer modeling of the evapotranspiration process has been introduced into the SM2RAIN algorithm. In order to do this, the modeling of the crop evapotranspiration according to the FAO-56 (Food and Agriculture Organization) model has been implemented into the algorithm. The results of this activity are presented in Chapter 6. In the following sections, the SM2RAIN algorithm and its configuration developed in this study to quantify irrigation, as well as the procedure for the validation of the results, are described.

4.6.1 The SM2RAIN Algorithm

SM2RAIN is a "bottom-up" approach originally developed for estimating precipitation rates through an inversion of the water balance with soil moisture observations as input. The algorithm has been initially implemented with in situ observations over pilot sites in Italy, Spain, and France (Brocca et al., 2013). In Brocca et al. (2015) the method has been tested over a large number of case studies in Europe. As a further development, the algorithm has been applied over large domains with remotely sensed soil moisture products as input (Brocca et al., 2014; Koster et al., 2016). A comparison between "bottom-up" approaches, involving SM2RAIN also, can be found in (Brocca et al., 2016). In the same work, the authors have proved the benefits in merging well consolidated rainfall products with "bottom-up" methods. A similar approach has been adopted by Ciabatta et al.

(2017) over Italy. It is noteworthy that, the SM2RAIN algorithm has led to the production and release of three global rainfall data sets freely available: SM2RAIN-ASCAT (Brocca et al., 2019), GPM+SM2RAIN (Massari et al., 2020), and SM2RAIN-CCI (Ciabatta et al., 2018). SM2RAIN-ASCAT covers the period 2007-2019, has a spatial resolution of 12.5 km and a daily temporal resolution. GPM+SM2RAIN is produced for the period 2007-2018 with a spatial resolution of 0.25° and a daily temporal resolution. Finally, SM2RAIN-CCI has the same spatial and temporal resolution of GPM+SM2RAIN, but it is delivered for the period 1998-2015.

Recently, the SM2RAIN algorithm has been adapted to quantify irrigation from soil moisture observations. The method has been applied with both coarse resolution satellite soil moisture (Brocca et al., 2018; Jalilvand et al., 2019) and in situ measurements (Filippucci et al., 2020). The idea beyond this new approach is that over agricultural areas the total amount of water entering into the soil, which is the algorithm's output, is the sum of rainfall plus irrigation. As an example, the simplification provided in Figure 4.17 can be a useful support.
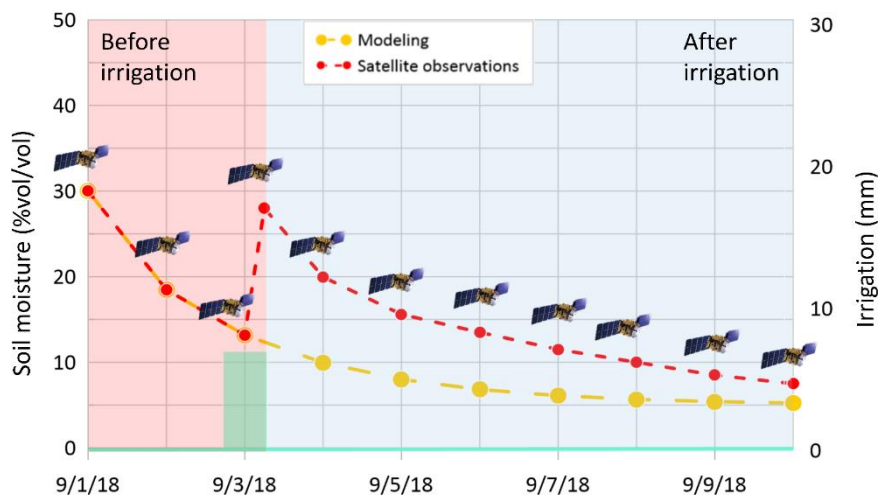
Figure 4.17. Conceptualization explaining the potential of remotely sensed soil moisture and of SM2RAIN in estimating irrigation.

In a hypothetical condition of absence of rainfall, a modeled soil moisture data set would show a decreasing trend in time, following a drying law. The model is expected to not take into account of irrigation; hence, even in case of irrigation occurrence, the trend would remain the same. Conversely, by assuming that a certain remote sensing product is able to detect irrigation, the trend of the observed soil moisture would show an increase as a consequence of irrigation before starting a new decrease. In general, the remotely sensed soil moisture can be affected by

70

both rainfall and irrigation. The sum of these two magnitudes is the total water entering into the soil in a certain range of time and it is quantified by SM2RAIN. If the rainfall is removed from this amount, the irrigation rate can be theoretically estimated. Figure 4.18 shows the flow chart of the proposed methodology to estimate irrigation over the pilot area in Spain, which is described in the following.

The soil water balance equation can be expressed in a general form as:

$$nZ\frac{dS(t)}{dt} = i(t) + r(t) - g(t) - sr(t) - e(t) \tag{4.7}$$

where n [-] indicates the soil porosity, Z [mm] is the considered soil layer depth, $S(t)$ [-] is the relative soil moisture, t [days] represents the time, $i(t)$ [mm/day] is the irrigation rate, $r(t)$ [mm/day] indicates the rainfall rate, $g(t)$ [mm/day] represents the drainage rate, determined by the sum of deep percolation and subsurface runoff, $sr(t)$ [mm/day] is the surface runoff and $e(t)$ [mm/day] indicates the actual evapotranspiration. Equation (4.7) can also be written as:

$$nZ\frac{dS(t)}{dt} = W_{in}(t) - g(t) - sr(t) - e(t) \tag{4.8}$$

in which the total amount of water entering into the soil, $W_{in}(t) = i(t) + r(t)$ [mm/day] is pointed out. The adoption of determined assumptions for specific cases, which are described in the following sections, allows to compute the $W_{in}(t)$ term through Equation (4.8). Hence, the irrigation rate can be computed by removing the rainfall rate from the total amount of water entering into the soil. In this thesis, the SM2RAIN algorithm has been used in two different configurations over the pilot area in the Ebro basin: one for the calibration of the model's parameters and another one for estimating the irrigation water amounts. The details of the two configurations are provided in the next two sections.
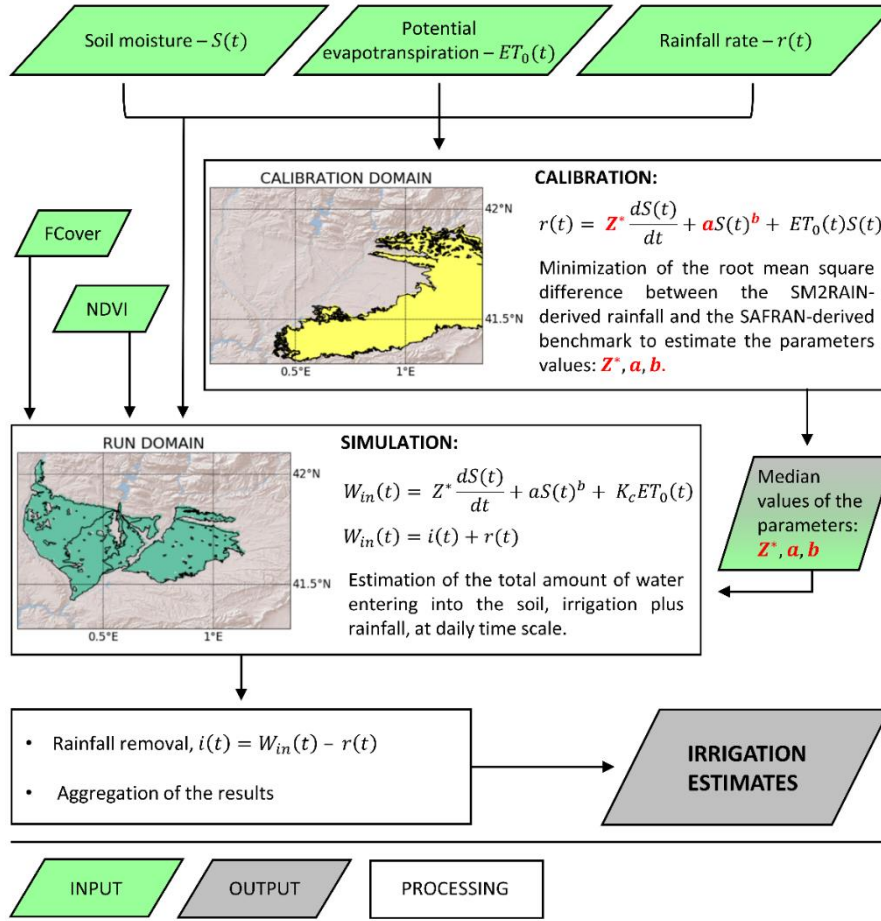
Figure 4.18. Flow chart of the method developed in this work of thesis to estimate irrigation water amounts (Dari et al., 2020).

4.6.1.1 Calibration

The calibration step has been carried out over the wide dryland area located on the East side of the irrigation districts (see Figure 4.18). As explained in Chapter 3, this portion is mainly constituted by rainfed cropland mixed with sparse forest and shrubs. The whole area is not irrigated; hence, the irrigation rate term, $i(t)$, is assumed equal to zero and the total amount of water that enters into the soil is determined by rainfall only, $W_{in}(t) = r(t)$. Equation (4.8) is rewritten as:

$$Z^* \frac{dS(t)}{dt} = r(t) - g(t) - sr(t) - e(t) \tag{4.9}$$

where $Z^* = nZ$ [mm] is the water capacity of the soil layer. A power law is adopted to describe the relation between the drainage rate and the soil moisture:

$$g(t) = aS(t)^b \tag{4.10}$$

in which a and b are drainage parameters. The surface runoff rate is assumed to be negligible (Brocca et al., 2015):

$$sr(t) = 0 \tag{4.11}$$

The actual evapotranspiration rate is assumed to be equal to the potential evapotranspiration, $ET_0(t)$ [mm/day], limited by the water content available in the investigated soil layer:

$$e(t) = ET_0(t)S(t) \tag{4.12}$$

In the proposed approach, the FAO Penman-Monteith method (Allen et al., 1998) has been used to calculate the potential evapotranspiration:

$$ET_0(t) = \frac{0.408\Delta(R_n - G) + \gamma\frac{900}{T+273}u_2(e_s - e_a)}{\Delta + \gamma(1 + 0.34u_2)} \tag{4.13}$$

in which Δ [kPa/°C] is the slope of the vapour pressure curve, R_n [MJ/m²day] indicates the net radiation at the crop surface, G [MJ/m²day] represents the soil heat flux density, T [°C] is the mean daily air temperature at 2 m height, u_2 [m/s] is the wind speed at 2 m height, e_s [kPa] represents the saturation vapour pressure, e_a [kPa] is the actual vapour pressure, and γ [kPa/°C] indicates the psychrometric constant. The Equation (4.13) is derived from the original Penman-Monteith formulation (Penman, 1948; Monteith, 1965) under the assumption of a terrestrial surface covered by a standard grass crop of 12 cm height, with a fixed surface resistance of 70 s/m and a fixed value of albedo equal to 0.23. As explained in Section 4.2, the potential evapotranspiration has been calculated starting from four fundamental atmospheric variables, three of them taken from the SAFRAN data set (the wind speed, the air relative humidity, and the air temperature) and one of them obtained by the ERA-5 data set (the solar net radiation).

As a result of the above discussed assumptions, Equation (4.8) can be formulated as follows:

$$r(t) = Z^* \frac{dS(t)}{dt} + aS(t)^b + ET_0(t)S(t) \tag{4.14}$$

then, the rainfall rate over the dryland area can be calculated and compared with reference rainfall from SAFRAN in order to calibrate the three model's parameters: Z^*, a, b. More in detail, the calibration has been performed through a proper objective function by minimizing the root mean square difference between the SM2RAIN-derived rainfall, calculated according the Equation (4.14), and the benchmark rainfall from the SAFRAN data set. For both the experiments carried out within this framework, the calibration process has been performed by working

at 5-days temporal aggregation, which maximized the performances in reproducing the actually occurred rainfall rates. As an output of the procedure, the spatial distributions of Z^*, a, and b over the calibration domain are obtained; the median values have been then used as fixed parameters for the irrigation estimates step.

4.6.1.2 Irrigation Quantification

The irrigation quantification step has been carried out for the pilot districts. Over the irrigated crops in this domain, the total amount of water entering into the soil is the sum of the rainfall and irrigation rates, $W_{in}(t) = i(t) + r(t)$. The previously described assumptions adopted for the drainage rate and for the surface runoff in the calibration step and reported in Equation (4.10) and (4.11), respectively, can be considered still valid. In this step, the dual crop approach proposed in the FAO paper n. 56 (Allen et al., 1998) has been integrated into SM2RAIN to adequately represent the evapotranspiration rate, $e(t)$. According to this approach, the crop evapotranspiration is obtained from the reference potential evapotranspiration, calculated through the Equation (4.13), multiplied by the crop coefficient, K_c [-], a parameter describing the crop status and its development:

$$e(t) = K_c ET_0(t) \tag{4.15}$$

according to the dual crop coefficient approach, the contributions of the crop transpiration is calculated separately from the evaporative contribution from the bare soil; hence, the crop coefficient is determined as the sum of two terms:

$$K_c = K_{cb} + K_e \tag{4.16}$$

in which K_{cb} [-] is the basal crop coefficient and quantifies the transpiration rate due to the plant, while K_e [-] is the soil water evaporation coefficient, referred to the evaporation rate from the soil surface. The Equation (4.16) can be generalized to take into account of the possible occurrence of stress conditions due to scarce water availability as follows:

$$K_c = K_s K_{cb} + K_e \tag{4.17}$$

where K_s [-] is the water stress coefficient. The three terms of Equation (4.15) K_s, K_{cb}, and K_e can be calculated through proper equations furnished in the FAO guidelines. Nevertheless, the application of these formulas over a wide and crop-composite area as the pilot site is difficult, since plenty of variables and a detailed knowledge of each single crop at plot scale are required for the rigorous

calculation. To overcome this issue, in this thesis empirical parametrizations based on optical remotely sensed data have been developed to approximate each term of Equation (4.17). Optical products have been widely used to assess and model the evolution of the crops (Simonneaux et al., 2008). In many studies, a linear relation existing between K_{cb} and the NDVI has been pointed out (to cite a few, Ray and Dadhwal, 2001; Calera-Belmonte et al., 2005; Duchemin et al., 2006; Er-Raki et al., 2007; Toureiro et al., 2016). In the approach proposed in this thesis, the basal crop coefficient, K_{cb}, has been obtained by scaling the NDVI between its maximum and a minimum value equal to 0.2 for each pixel in the irrigated domain. Hence, dynamic values of K_{cb} ranging between 0.2 and 1 have been obtained. The minimum has been chosen on the basis of reference crop production curves referred to the most widespread crops in the area of interest. Stress conditions due to water limitation have been taken into account through the following equation, which puts in relation K_s and the relative soil moisture:

$$\begin{cases} K_s = \frac{S(t)}{p}, \ S(t) < p \\ \quad K_s = 1, \ S(t) \geq p \end{cases} \tag{4.18}$$

where the p [-] parameter is defined as a soil moisture threshold below which stress occurs. If the relative soil moisture is higher than the p threshold, there is no stress (K_s = 1), while a drop below the p threshold of the relative soil moisture determines the beginning of stress conditions, modeled as a linear decrease of K_s. A p value equal to 0.45 has been adopted for both the irrigation-estimate experiments carried out over the pilot area in the Ebro basin presented in this thesis. Hence, stress is assumed to begin when the relative soil moisture drops below the 45%. Some clarifications about the choice of this value are necessary. The value of 0.45 has been chosen because it has proven to be the most suitable one in reproducing the long-term magnitudes of actually occurred irrigation over the pilot area. It is important to highlight that, in the proposed approach, the beginning of stress conditions is determined through a surface soil moisture threshold, but in the real physics of the process plants can take water from the root zone also. Finally, it is noteworthy that, in both the experiments carried out severe stress conditions rarely occur. The FAO guidelines propose an energy-based limitation for determining K_e; according to this approach, the coefficient has an upper limit that depends on the fraction of soil surface wetted and exposed, over which the evaporation process occurs, and on the maximum K_c value ensuring the non-exceedance of the available energy. In the methodology proposed in this

thesis, a water-limitation approach is adopted instead of an energy-based approach. The coefficient describing the evaporation from the soil surface is formulated as:

$$K_e = (1 - f_c)S(t) \tag{4.19}$$

in which f_c represents the fraction of vegetation cover, taken from the Copernicus FCover data set (see Section 4.1.3). The proposed formulation is equivalent to assume that, over the bare soil portion of an irrigated pixel, the evaporation is limited by the available water in the soil layer. It is noteworthy that, Equation (4.19) is consistent with the formulation of the actual evapotranspiration adopted over the dryland area in the calibration step, where the contribution of the transpiration is not predominant. For this reason, a coarser approach for representing the evapotranspiration process has been adopted over the calibration domain with respect to the finer modeling used for the irrigated land. The above discussed assumptions led to the building of a dynamic K_c both in space and time. As an example, the spatial distributions of the mean values of the coefficients K_s and K_c calculated for the period May-September 2016 are shown in Figure 4.19.
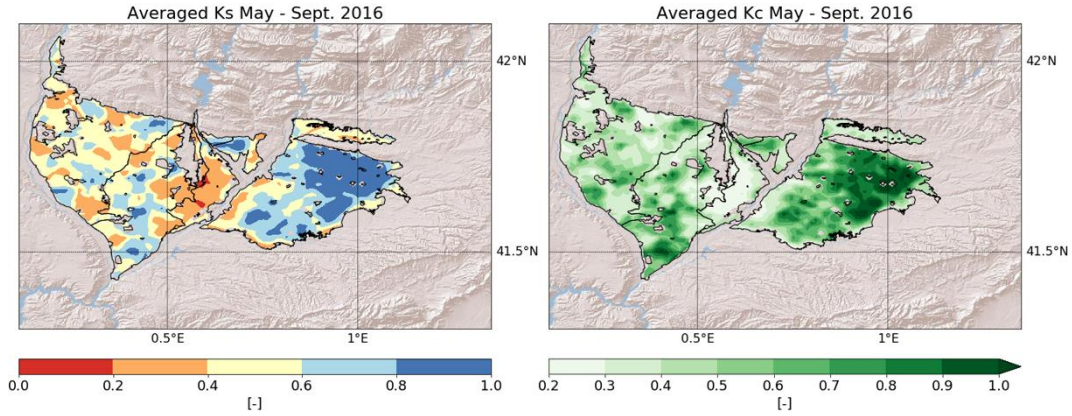
Figure 4.19. Spatial distributions of the mean values of the coefficients K_s and K_c calculated for the period May-September 2016.

The above discussed assumptions allow Equation (4.8) to be rewritten as follows:

$$W_{in}(t) = Z^* \frac{dS(t)}{dt} + aS(t)^b + K_c ET_0(t) \tag{4.20}$$

where the SM2RAIN parameters Z^*, a, and b are fixed to the median values of their distributions resulting from the calibration. Equation (4.20) allows to compute the total amount of water entering into the soil layer at a daily temporal resolution. Then, the irrigation rates can be retrieved by removing the rainfall rates from the

total, $i(t) = W_{in}(t) - r(t)$. If the $i(t)$ term assumes negative values, it is assumed equal to zero.

4.6.1.3 Assessment of the Model's Parameters Uncertainty

An analysis aimed to assess the model sensitivity to its parameters has been performed for the SMAP experiment, which is referred to a shorter period with respect to the SMOS experiment. The uncertainty to the three canonical SM2RAIN parameters involved in the calibration phase (Z^*, a, and b) has been investigated apart from the uncertainty due to the soil-moisture-based stress threshold p.

The computations aimed at estimating the irrigation water amounts have been performed by keeping the values of Z^*, a, and b fixed to the median values of their spatial distributions over the calibration domain. The model sensitivity to Z^*, a, and b has been assessed through a set of alternative simulations, in which random combinations of the three parameters have been adopted. The additional simulations have been carried out by adopting all the possible combinations of the 25th, 50th, and 75th percentiles of the distributions of the three parameters resulting from the calibration step. A total of twenty-six additional simulations have been performed to build a confidence interval around the main one, which is carried out by adopting the median values of each parameter's distribution, corresponding to the 50th percentile. The model's sensitivity to the stress threshold, p, has been assessed by adopting the main simulation (in whose configuration Z^*, a, and b are equal to the median values of their distributions) and by increasing p from 0.3 to 0.6 with steps of 0.01. The thirty additional simulations resulting from this procedure allowed to build the confidence interval around the main elaboration used to assess the sensitivity to p.

4.6.2 Validation

The validation of the estimated irrigation amounts over the pilot districts within the study area in the Ebro basin has been carried out through comparisons with the benchmark irrigation volumes from different data sets described in Section 4.4.2. For each district, the sources of the benchmark volumes adopted are shown in Table 4.2. Please note that the stations belonging to the SAIH system are shown in the panel b) of Figure 4.12.

In the SMAP experiment, the volumes of water flowing through the irrigation canals C116, "*Cabecera Urgell*", and C117, "*Auxiliar Urgell*", have been exploited to

derive the benchmark values for the Urgell district. Unfortunately, the data about the water supplying this district are missing for the period July 2016 – February 2017. For this reason, the alternative source of data represented by the Hydrological Plan of the Spanish Part of the Ebro River Basin has been used for the 2016. Conversely, the SAIH-derived data have been exploited for the sub-period from January to September 2017, by assuming that the missing amounts referred to January 2017 are negligible. The benchmark irrigation volumes for the Algerri Balaguer district and for both the partitions of the Catalan and Aragonese district have been deduced from the SAIH system. The water pumped at the station E271 has been considered for the Algerri Balaguer, while the volumes recorded at the stations C081 ("*El Ciego*") and C101 ("*Coll de Foix*") have been used for the Northern and Southern partitions of the Catalan and Aragonese district, respectively. As explained in the Section 4.4.2, the monthly irrigation amounts for the Pinyana district have been furnished by the canal's technical office.

In order to be compared with SM2RAIN-derived irrigation estimates, the benchmark irrigation volumes have been converted to the equivalent thickness of water (in mm) by dividing them by the area of interest; hence, a homogeneous layer of irrigation water has been compared with the satellite-derived estimates over each pilot district. It is noteworthy that a very small part of the Urgell located in its East side and characterized by low irrigation density has not been considered. It is important to point out that only the portion of water actually reaching the soil can be detected through remote sensing techniques. Hence, the gross benchmark irrigation amounts have been adjusted by considering possible losses due to the irrigation efficiency. Several parameters have been evaluated to estimate the entity of the losses: the employed irrigation techniques, the dating of the irrigation systems, and statistics derived from studies on this topic carried out over the area of interest. Canela et al. (1991) studied the efficiency (defined as the rate of applied water reaching the root zone) of the flood irrigation system existing in Urgell. Higher efficiencies (mean of 90%) in the lower part of the district with respect to lower efficiencies (mean of 66%) in the upper part were found. Cots et al. (1993) determined a mean irrigation efficiency of 77% over the Urgell. Maté et al. (1994) selected various crops in the Catalan and Aragonese district where studying the efficiency of the irrigation systems there; the authors obtained efficiencies ranging between 62% for the sunflower and 89% for fruit trees. In general, higher efficiencies for sprinkler systems with respect to flood irrigation systems are

expected; in addition, among all the existing irrigation techniques, drip irrigation should ensure the maximum efficiencies.

The entities of the losses adopted for each district have been established on the basis of the abovementioned considerations. For the Urgell district, where irrigation mainly occurs through its old flood system, a reduction equal to the 30% of the total amount of delivered water has been assumed. For the Catalan and Aragonese district, where mixed irrigation techniques are adopted, losses equal to the 15% of the total have been assumed. A reduction of the 10% has been applied to the water pumped to the Algerri Balaguer district, whose irrigation system is the most recent one of the entire study area. Finally, losses equal to the 30% of the total have been assumed for the Pinyana district, which is the most ancient system among those considered.

Regarding the irrigation-estimate experiment carried out by exploiting SMOS data, the same sources of benchmark irrigation previously described have been adopted. The prevision based on historical data already used for the Urgell in 2016 has been kept for the previous years also over the same domain; for the Algerri Balaguer and for the Catalan and Aragonese district, SAIH data have been exploited. Unfortunately, the benchmark irrigation volumes referred to the period 2011-2015 for the Pinyana district are not available. The net irrigation benchmark values adopted for comparisons with satellite-derived estimates have been firstly converted in water layer thickness (in mm) and later reduced according to the losses due to the efficiency of the irrigation systems by following the same procedure previously described for the SMAP experiment. Table 4.2 provides, for each district, the areas considered to convert the irrigation volumes to irrigation thicknesses, the sources of the benchmark data, and the assumed losses.

Table 4.2. Areas of the irrigation districts used to convert the benchmark irrigation volumes to irrigation thicknesses, sources of benchmark data adopted, and assumed losses due to the irrigation systems efficiency (Dari et al., 2020).

District	Area [km²]	Irrigation Benchmark Source	Losses
Urgell	811.67	Ebro Hydrological Plan / Water flowing through the irrigation canals (SAIH Ebro, stations C116 and C117)	30%
Catalan and Aragonese - North	657.04	Water flowing through the irrigation canals (SAIH Ebro, station C081)	15%
Catalan and Aragonese - South	504.48	Water flowing through the irrigation canals (SAIH Ebro, station C101)	15%
Algerri Balaguer	70.79	Water pumped to the district (SAIH Ebro, station E271)	10%
Pinyana	149.74	Data furnished by the canal's technical office	30%

Chapter 5

Results of the Irrigation Detection and Mapping Activity

In this chapter, the results achieved in the irrigation detection and mapping activity are presented. In detail, the results obtained over the pilot area located in the Ebro basin are described in Section 5.1, while Section 5.2 provides a description of the analyses carried out over the Upper Tiber basin. It is noteworthy that, for all the analyses whose results are described in this chapter and in the next one, all the gridded data sets used have been resampled on the 1 km spatial resolution regular grids used for the SURFEX-ISBA simulations (see Figures 4.9 and 4.10). Hence, spatially coherent data sets have been obtained through this procedure.

5.1 Results over the Pilot Area in the Ebro Basin

In this section, the results of the investigation on the capability of several remotely sensed data sets in detecting the irrigation signals are firstly presented; the data sets used are: SMAP at 1 km resolution (downscaled through the DISPATCH algorithm) and at 9 km sampling, SMOS at 1 km resolution (downscaled through the DISPATCH algorithm), Sentinel-1 at 1 km resolution, and ASCAT at 12.5 km. Henceforth, the downscaled products are called "SMOS at 1 km" and "SMAP at 1 km", while the other data sets "SMAP", "Sentinel-1", and "ASCAT". Table 5.1 summarizes the main characteristics of the remote sensing soil moisture used. The analysis proposed in this ambit is mainly oriented to high-resolution (1 km) products; however, the SMAP and ASCAT products have been involved in the analysis to investigate the detectability of irrigation signals over the study area through coarser resolution products also. Unlike for SMAP, coarse resolution SMOS data has not been considered along with its downscaled version; the reason relies in the lower accuracy often detected for SMOS with respect to SMAP data (Chen et al., 2018). In general, the performances of each remote sensing data set in spotting irrigation is evaluated by means of the temporal stability derived indices,

useful to characterize the spatial-temporal variability of the retrieved soil moisture observations. The surface soil moisture modeled with SURFEX-ISBA also has been involved in the analysis; its role is that of negative benchmark, as in the model irrigation is not taken into account. Hence, the modeled data reproduces a natural, non-human-altered, situation.

Table 5.1. Overview of the main features of the remote sensing soil moisture products used in the analysis aimed to evaluate the detectability of irrigation over the pilot area in the Ebro basin: sensor aboard the satellite, operating band, and spatial resolution.

Product	Sensor	Operating Band	Spatial Resolution
SMOS at 1 km	Y-shaped passive 2D interferometric radiometer	L-band (1.4 GHz)	1 km – downscaled through the DISPATCH algorithm
SMAP at 1 km	radiometer radar – not working	radiometer: L-band (1.4 GHz) radar: L-band (1.26 GHz) – not working	1 km – downscaled through the DISPATCH algorithm
SMAP	radiometer radar – not working	radiometer: L-band (1.4 GHz) radar: L-band (1.26 GHz) – not working	9 km sampling
Sentinel-1	SAR	C-band (5.4 GHz)	1 km
ASCAT	real aperture active radar	C-band (5.3 GHz)	12.5 km sampling

The analyses aimed at evaluating the capability of the considered data sets in detecting irrigation are described in Section 5.1.1, while Section 5.1.2 presents the following step of this study, namely the irrigation mapping. In fact, the best performing products in detecting irrigation arising from the precedent step have then been exploited as an input for the K-means clustering algorithm to map irrigated areas. Although the analyses carried out over the pilot area in Spain cover the period 2016-2017, many results are focused on the time span going from May

to September of the two selected years, which is when irrigation mainly occurs over the study area.

5.1.1 Temporal Stability Derived Indices

The spatial relative differences quantify how much the soil moisture value in a certain pixel differs from the spatial mean of the entire area considered during the same observation day. For this reason, the index is particularly suitable to evaluate the capability of a remotely sensed data set in detecting irrigation. In fact, it is expected to assume higher values over the irrigated areas, human-induced to be adequately wet during the dry season, with respect to the dryland. The particular landscape that characterizes the study area is expected to emphasize this behaviour, thus making the pilot site particularly suitable for the proposed purposes. In Figure 5.1, the panels a.1), b.1), and c.1) show the time series of the areal mean relative differences calculated for the Urgell area, for the Catalan and Aragonese area, and for the dryland area, which are represented in panels a), b), and c), respectively. The volumes of water flowing through the irrigation canals that supply water to the Urgell area and to the Catalan and Aragonese area are shown in panels a.2) and b.2), respectively. These data are taken from the SAIH system. More in detail, the flow data supplying the Urgell has been recorded by the stations "C116-*Cabecera Urgell*" and "C117-*Auxiliar de Cabecera Urgell*", while for the Catalan and Aragonese area the stations exploited are "C081-*El Ciego*" and "C101-*Coll de Foix*". It is noteworthy that, during the period from July 2016 to February 2017, the data about irrigation data supplying the Urgell area are missing because of an interruption in the recording.

The time series provides a first insight on the capability to detect irrigation at a district scale of the selected data sets. The evaluation is performed by looking at which product shows higher values of the spatial relative difference in the irrigated areas concurrently with lower values in the surrounding dryland during the highest-intensity periods, which are shaded in grey in Figure 5.1.
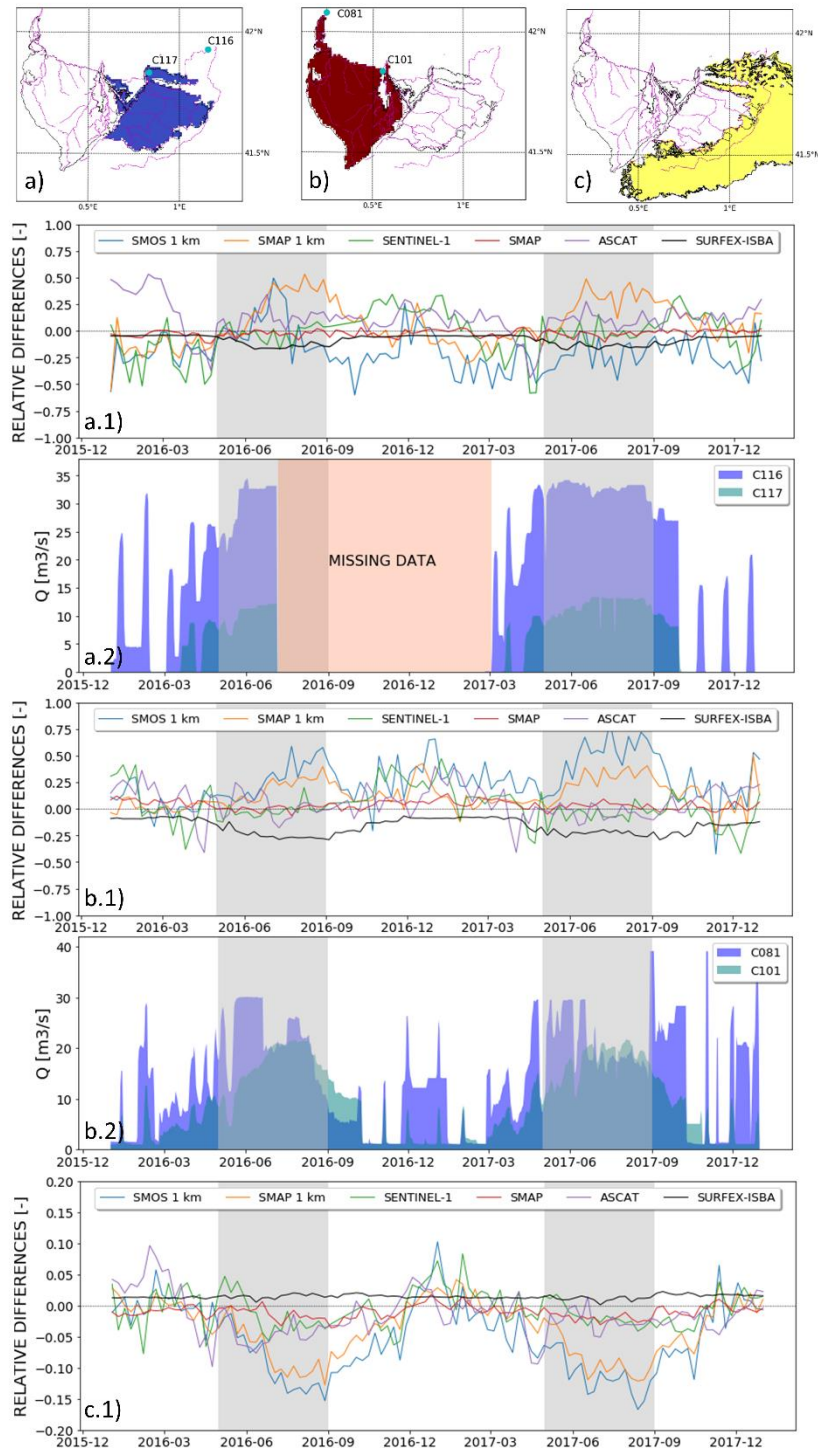
Figure 5.1. The panels a.1), b.1) and c.1) show the time series of the weekly spatial relative differences averaged inside the corresponding areas: a) Urgell area, b) Catalan and Aragonese area, and c) the dryland. The daily flow recorded in the canals feeding the Urgell and the Catalan and Aragonese areas are shown in panels a.2) and b.2), respectively. Note that for panel c.1) a different y-axis range has been adopted (Dari et al., 2021a).

SMAP at 1 km results the best performing high-resolution (1 km) product over the Urgell area; in fact, for this data set, mean relative differences equal to 0.274 during May-September 2016 and equal to 0.266 during May-September 2017 in face of values equal to -0.078 and to -0.088, respectively, obtained during the same periods over the dryland surrounding the irrigation districts are obtained. Good performances are observed for SMOS at 1 km in the first half of the highest-intensity irrigation period of 2016; in the second half of the same period, as well as during May-September 2017, the relative differences drop down. Sentinel-1 seems not to show irrigation signals detected over the Urgell area. Regarding the coarser resolution data sets, ASCAT performs better than SMAP; ASCAT-derived mean relative differences are equal to 0.121 for the period May-September 2016 and to 0.111 for May-September 2017. The values referred to the dryland area during the same periods are equal to -0.045 and to -0.023.

Over the Catalan and Aragonese area, mean relative differences equal to 0.286 and to 0.481 referred to the periods May-September 2016 and 2017, respectively, have been obtained with SMOS at 1 km, which results the best performing product over the area. For the same product, values equal to -0.100 and to -0.112 are obtained over the dryland area during the same periods. The performances of SMAP at 1 km over the Catalan and Aragonese area are comparable to those of SMOS at 1 km. Conversely, Sentinel-1 keeps on not showing irrigation signals according to the considered metric. Unsatisfactory performances over the Catalan and Aragonese area are obtained for the coarser resolution products involved in this analysis.

For both the irrigated macro-areas, the mean relative differences calculated with the SURFEX-ISBA modeled soil moisture show similar trends, consisting in slightly lower values than the spatial mean during the summer seasons in 2016 and 2017 with respect to the rest of the investigated period. Over the dryland, the trend is almost constant in time. The reasons for this behaviour mainly rely in the absence of the irrigation information in the modeled soil moisture, whose spatial distribution is determined by the soil map and by the vegetation scheme implemented in the model. In fact, in the ISBA version used in this research, the vegetation scheme is prescribed and it is based on the climatology of the Leaf Area Index (LAI); hence, the cycle of the vegetation is the same every simulated year.

Along with spatial-averaged time series providing information at an irrigation district spatial scale, the analysis of the spatial distribution of the relative differences is helpful in highlighting possible sub-areas where irrigation actually

occurs. In fact, by considering the averaged value for each irrigated macro-area only can be misleading, as it is not always true that the entire irrigable area is actually irrigated. The maps of the spatial relative differences averaged in time during the highest-intensity irrigation periods (May-September) of 2016 and 2017 are provided in Figures 5.2 and 5.3. More in detail, the maps referred to the high-resolution (1 km) products are shown in Figure 5.2, while the maps produced for the coarser resolution data sets are provided in Figure 5.3.

For both DISPATCH downscaled products, the spatial distribution of the mean relative differences during the focus period in 2016 shows expected higher values over the irrigated land with respect to the dryland area. During May-September 2017, the contrast between the irrigated areas (wet) and the surrounding dryland (dry) are still well reproduced by SMAP at 1 km; conversely, during the same period, slightly negative values of the relative differences are obtained for SMOS at 1 km over the Urgell. In the maps of the relative differences computed with soil moisture data retrieved by Sentinel-1, negative values can be observed over the Urgell area; slightly positive values are detected in the middle of the Catalan and Aragonese area. The dryland is not well reproduced, except for its Northern side, where rainfed croplands are located. As previously said, the maps derived from SURFEX-ISBA soil moisture represent a reference for a situation not taking into account of irrigation. In fact, they show a dry condition over the flat agricultural areas. Finally, the maps referred to SMAP and ASCAT clearly point out their limitations over the pilot area for this kind of application, due to the coarse resolution.

The temporal anomalies allow to evaluate the capability of the considered microwave soil moisture products to detect irrigation by analysing the same problem under a temporal perspective rather than a spatial one. In fact, this second index quantifies the difference between the soil moisture value observed in a certain pixel during a certain observation day and its temporal mean, which in this application has been calculated for the entire study period. The time series of the weekly-aggregated temporal anomalies spatially averaged over the Urgell area, the Catalan and Aragonese area, and the dryland are provided in Figure 5.4. The main advantage of the analysis in terms of temporal anomalies is that by looking at the temporal dynamics of soil moisture, the results are not influenced by static patterns, e.g., soil texture, that may affect soil moisture observations. Similarly to the analysis in terms of spatial relative differences, in the temporal analysis good performances in detecting irrigation are represented by higher values of the

considered metric within the irrigable lands with respect to the dryland over the irrigation seasons.
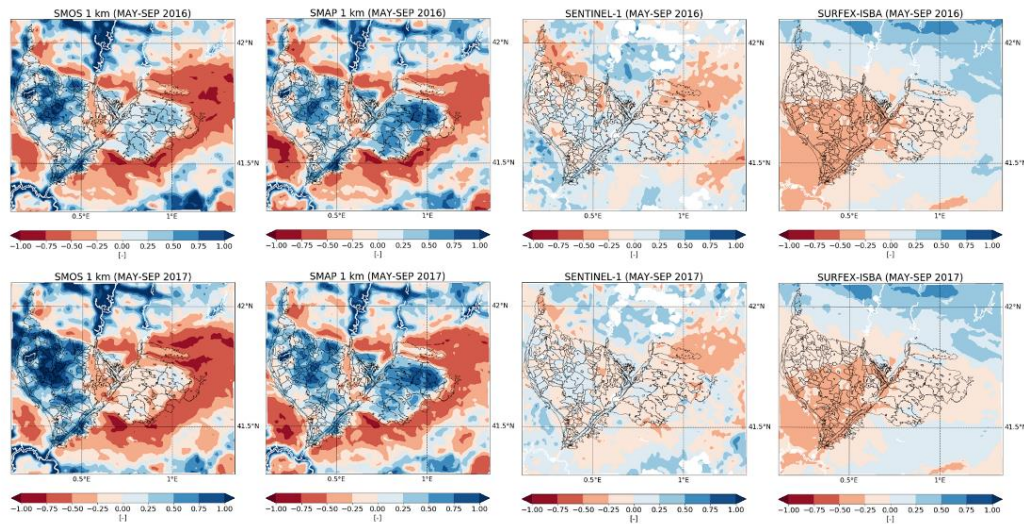
Figure 5.2. Maps of the spatial relative differences averaged during the periods May-September 2016 (upper panel) and 2017 (lower panel). The maps are referred to the high-resolution (1 km) products used in this analysis (Dari et al., 2021a).
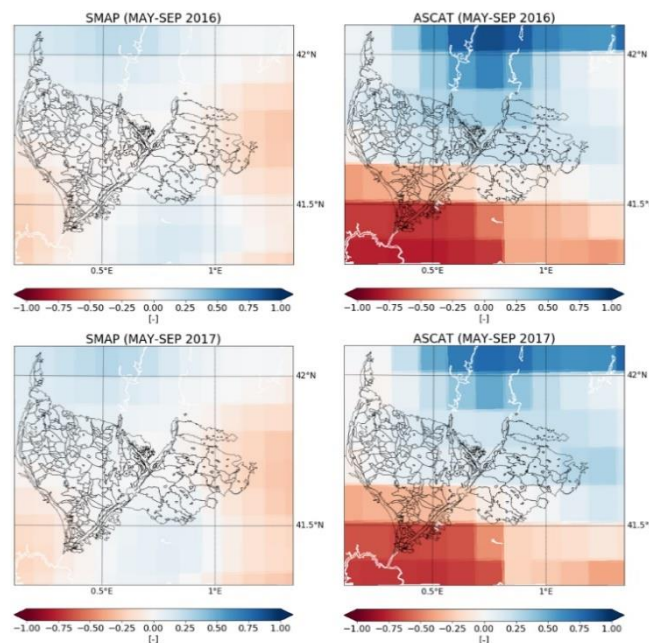
Figure 5.3. Maps of the spatial relative differences averaged during the periods May-September 2016 (upper panel) and 2017 (lower panel). The maps are referred to the coarser resolution products used in this analysis (Dari et al., 2021a).

Both SMOS and SMAP at 1 km show mean temporal anomalies calculated for the irrigated macro-areas higher than those calculated for the dryland during the highest-intensity irrigation periods of 2016 and 2017, which are shaded in grey in Figure 5.4. The only exception is detectable for SMOS at 1 km over the Urgell area during the period May-September 2017. Mean positive temporal anomalies can be observed for Sentinel-1 over the irrigable lands; however, the same happens for the dryland too. Hence, the different wetness conditions coexisting in the pilot area are not well reproduced. In general, SURFEX-ISBA data show lower temporal anomalies during the highest irrigation intensity periods. This is an expected result from a modeled data set not considering irrigation, in which the temporal dynamics of soil moisture are mainly determined by precipitation events. Finally, no clear discrepancies attributable to irrigation between the time series of the temporal anomalies over the irrigated areas and the dryland can be observed for SMAP and ASCAT.
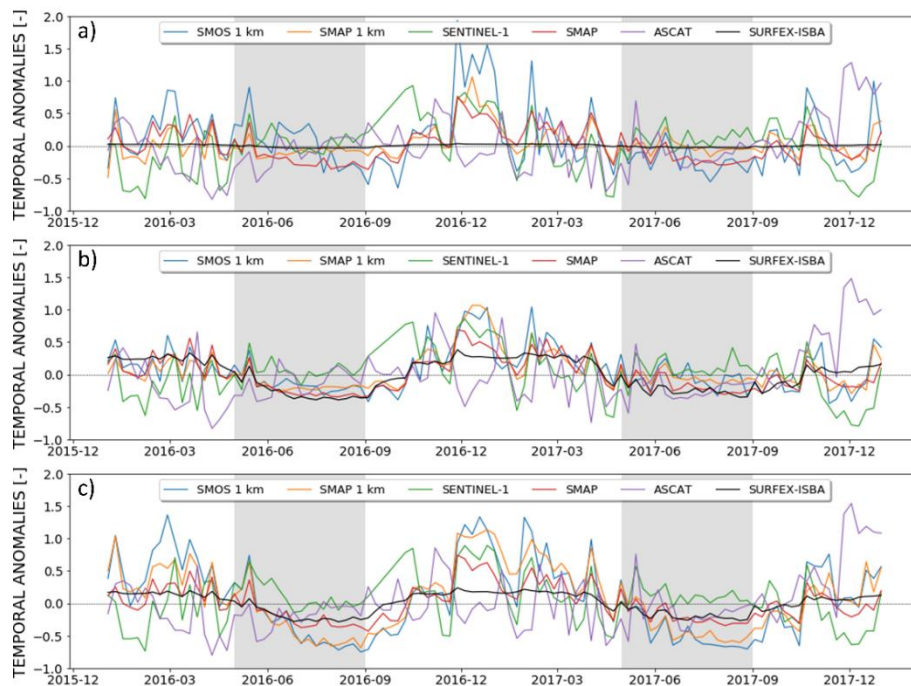
Figure 5.4. Time series of the weekly-aggregated temporal anomalies averaged over: a) the Urgell area, b) the Catalan and Aragonese area, and c) the dryland (Dari et al., 2021a).

In line with what said for the analysis performed through the spatial relative differences, the analysis of the district-averaged indices must be coupled with a spatially distributed information if the aim is to spot the actually occurrence of

irrigation. Hence, maps of the temporal anomalies averaged during the periods May-September 2016 and 2017 are provided in Figures 5.5 and 5.6.
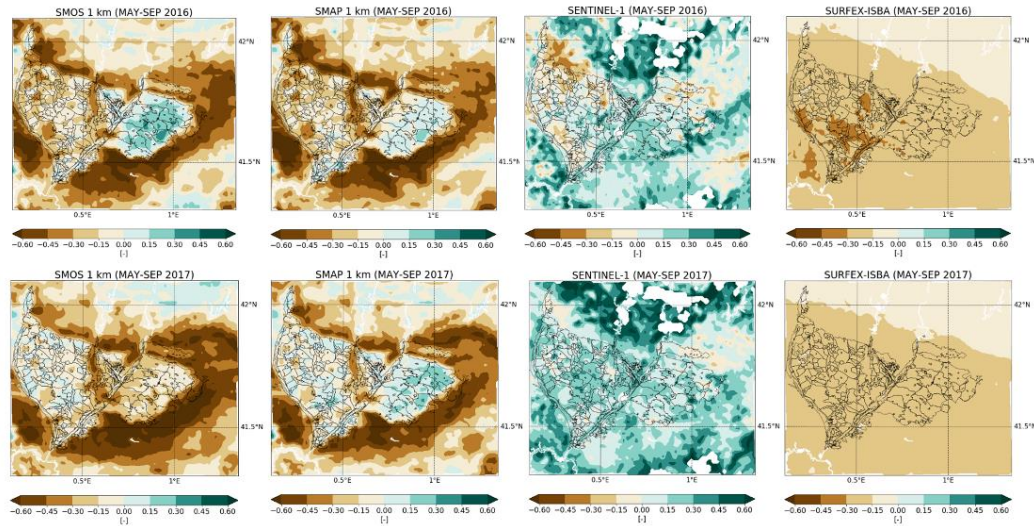
Figure 5.5. Maps of the temporal anomalies averaged during the periods May-September 2016 (upper panel) and 2017 (lower panel). The maps are referred to the high-resolution (1 km) products used in this analysis (Dari et al., 2021a).
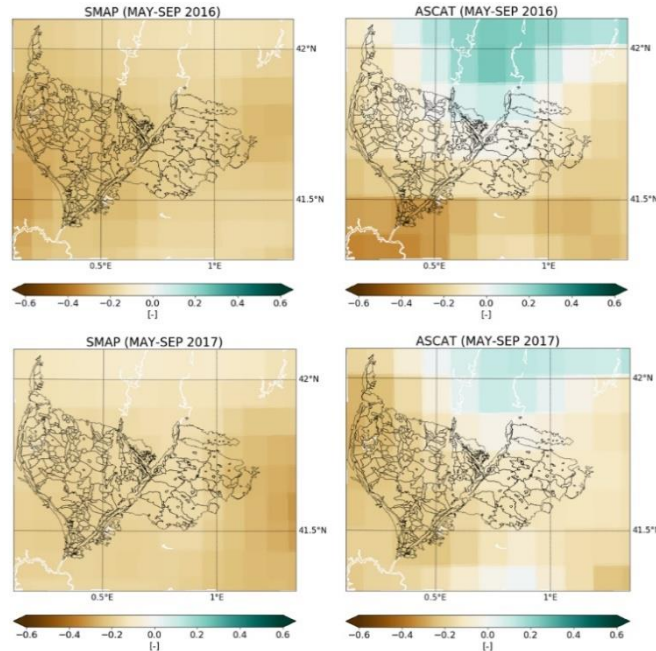
Figure 5.6. Maps of the temporal anomalies averaged during the periods May-September 2016 (upper panel) and 2017 (lower panel). The maps are referred to the coarser resolution products used in this analysis (Dari et al., 2021a).

In this case, good performances in detecting irrigation evaluated through the temporal anomalies are represented by both positive (pixel wetter to its two-years

temporal mean during the irrigation season) or close to zero (pixel close to its two-years temporal mean during the irrigation season) values of this metric over the irrigable lands concurrently with lower values over the dryland.

Satisfactory results are obtained for both the downscaled products during the periods May-September 2016 and 2017; in fact, the mean temporal anomalies calculated for these data sets are generally higher than or equal to zero over the irrigated areas. In particular, a homogeneous pattern of positive temporal anomalies recurs over the Urgell (except for the maps referred to SMOS at 1 km during the focus period in 2017). Over the Catalan and Aragonese area, higher temporal anomalies during the irrigation season in 2017 with respect to the same period of 2016 can be observed for both downscaled products. It is noteworthy that, the maps referred to SMAP and SMOS at 1 km show higher anomalies within the irrigable lands with respect to the dryland at East of the Urgell area. Sentinel-1 data provide an unexpected and mostly uniform humid condition, thus corroborating the unsatisfactory results previously described. The maps referred to SMAP and ASCAT still highlight their limitations over the pilot area for this kind of application due to the coarse resolution. Finally, the SURFEX-ISBA-derived maps provide a uniform dry situation, which is expected during the dry season from a modeled data set in which irrigation is not considered.

5.1.2 Correlation Analysis

An additional statistical feature that can be interpreted as a proxy of irrigation is the correlation between remotely sensed and modeled soil moisture during the irrigation season. Hence, the correlation between each remotely sensed soil moisture data set and the SURFEX-ISBA soil moisture during the highest-intensity irrigation periods in 2016 and 2017 has been calculated. The Pearson correlation coefficient ($\bar{r}$) between the remote sensing products and the SURFEX-ISBA output and averaged over the Urgell area, over the Catalan and Aragonese area, and over the dryland is provided in Figure 5.7. Considering that in the adopted configuration the modeled soil moisture does not take into account of irrigation, and by assuming that precipitations are correct, low (scarce correlation) or negative (inverse correlation) $\bar{r}$ values obtained for an irrigated area can be attributed to the capability to contain the irrigation information of the remotely sensed product. According to this approach, SMOS at 1 km is the data set showing the clearest signal attributable to the irrigation, as it is less correlated with modeled soil moisture over the irrigated macro-areas with respect to what happens over the

dryland. A similar result was obtained, over the Urgell, by Escorihuela and Quintana-Seguí (2016). For SMAP at 1 km, the lowest correlation values are obtained over the Urgell area; then, $\bar{r}$ increase over the Catalan and Aragonese area, but it remains lower than over the dryland, where the highest values for this product are obtained. In line with the results presented in the previous section, Sentinel-1 does not provide clearly irrigation-related results. SMAP retrieved soil moisture is the most correlated with modeled soil moisture from SURFEX-ISBA, independently by the area or the period considered. Hence, this data set does not show any kind of signal interpretable as irrigation. Finally, ASCAT provides the lowest correlation values, which are often negative. However, this happens over the irrigated areas and over the dryland indiscriminately; hence, this issue cannot be interpreted as an irrigation signal.
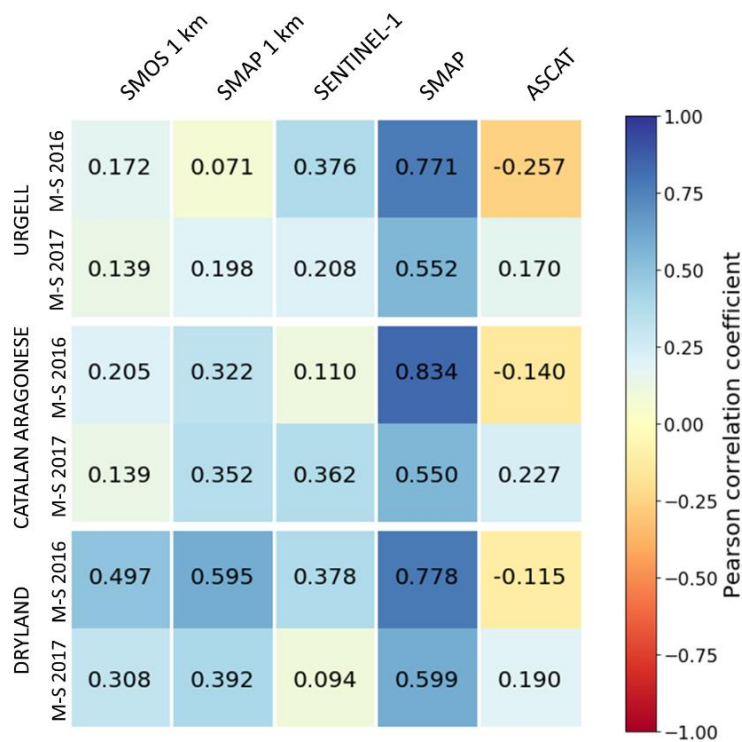
Figure 5.7. Heatmap showing the areal mean correlation between satellite and modeled soil moisture data sets during the periods May-September 2016 and 2017 over the Urgell area, the Catalan and Aragonese area and the dryland area surrounding the irrigation districts.

This result can be likely attributed to the coarse resolution of the data set, too low with respect to the extent of the irrigated areas over the pilot site to properly disentangle the signal from the irrigated pixels from the signal coming from the adjacent dryland.

The spatial distribution of the correlation values during May-September 2016 and 2017, calculated for the high-resolution (1 km) soil moisture product only, is provided in Figure 5.8. Comparable distributions are obtained for the DISPATCH downscaled products. During the highest-intensity irrigation periods in 2016, both SMOS and SMAP at 1 km show a low correlation pattern in the Urgell. This behaviour is less visible during the focus period in 2017, but correlation over the irrigable land still remains lower than over the dryland, especially in its Northern part, which is mainly occupied by rainfed croplands. Unclear correlation patterns are detected for Sentinel-1 in May-September 2016. During the same season in 2017, except for the upper part of the dryland, the correlation patterns are almost the opposite of what expected.
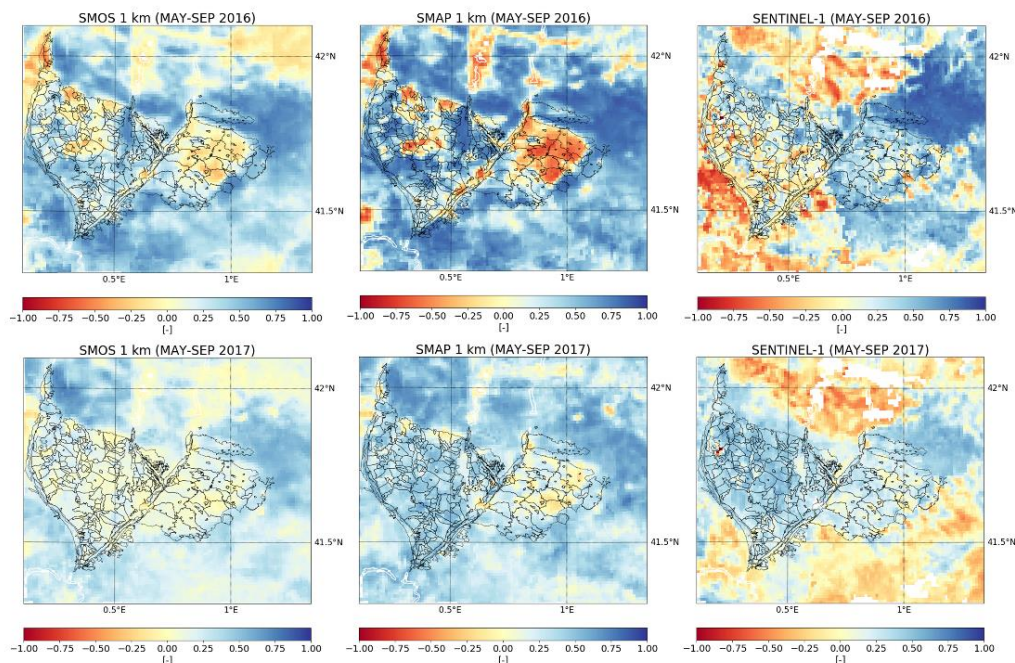
Figure 5.8. Maps of the spatial distribution of the correlation between satellite and modeled soil moisture for the periods May-September 2016 (upper panel) and May-September 2017 (lower panel). The maps are referred to the high-resolution (1 km) products used in this analysis (Dari et al., 2021a).

5.1.3 K-means Clustering Classification

On the basis of the best performing products arising from the previously described investigation, namely SMOS and SMAP at 1 km, the analysis aimed to map irrigated areas has been refined. The DISPATCH downscaled products have been exploited to map the three prevalent classes of natural surfaces detectable over the

pilot area (irrigated areas, dryland, and forest or natural areas) through the K-means algorithm; hence, three clusters have been considered. The classification has been performed by merging information derived from satellite and modeled soil moisture as input for the clustering. The method does not require any training step, as it is only based on statistical and temporal stability derived features, which are expected to assume a determined behaviour over the irrigable lands during the highest-intensity irrigation periods; the input parameters are summarized in Table 5.2.

Table 5.2. The sixteen parameters combinations adopted to perform the clustering (adapted from Dari et al., 2021a).

MAY-SEPTEMBER 2016			MAY-SEPTEMBER 2017		
Category	*Input parameters*	*Code*	*Category*	*Input parameters*	*Code*
Satellite soil moisture based	$\sigma(\delta_x)$, $\bar{A}_x$ from SMOS at 1 km	ST.A.SMOS16	Satellite soil moisture based	$\sigma(\delta_x)$, $\bar{A}_x$ from SMOS at 1 km	ST.A.SMOS17
	$\sigma(\delta_x)$, $\bar{A}_x$ from SMAP at 1 km	ST.A.SMAP16		$\sigma(\delta_x)$, $\bar{A}_x$ from SMAP at 1 km	ST.A.SMAP17
	$\bar{\delta}_x$, $\bar{A}_x$ from SMOS at 1 km	D.A.SMOS16		$\bar{\delta}_x$, $\bar{A}_x$ from SMOS at 1 km	D.A.SMOS17
	$\bar{\delta}_x$, $\bar{A}_x$ from SMAP at 1 km	D.A.SMAP16		$\bar{\delta}_x$, $\bar{A}_x$ from SMAP at 1 km	D.A.SMAP17
Merging modeled and remotely sensed soil moisture	$\sigma(\delta_x)$, $\bar{A}_x$, r_x from SMOS at 1 km	ST.A.C.SMOS16	Merging modeled and remotely sensed soil moisture	$\sigma(\delta_x)$, $\bar{A}_x$, r_x from SMOS at 1 km	ST.A.C.SMOS17
	$\sigma(\delta_x)$, $\bar{A}_x$, r_x from SMAP at 1 km	ST.A.C.SMAP16		$\sigma(\delta_x)$, $\bar{A}_x$, r_x from SMAP at 1 km	ST.A.C.SMAP17
	$\bar{\delta}_x$, $\bar{A}_x$, r_x from SMOS at 1 km	D.A.C.SMOS16		$\bar{\delta}_x$, $\bar{A}_x$, r_x from SMOS at 1 km	D.A.C.SMOS17
	$\bar{\delta}_x$, $\bar{A}_x$, r_x from SMAP at 1 km	D.A.C.SMAP16		$\bar{\delta}_x$, $\bar{A}_x$, r_x from SMAP at 1 km	D.A.C.SMAP17

The parameters exploited as input for the clustering are the mean relative difference, $\bar{\delta}_x$, the standard deviation of the relative differences, $\sigma(\delta_x)$, the mean of the temporal anomaly, $\bar{A}_x$, and the correlation between satellite and modeled soil moisture, r_x; $\bar{\delta}_x$ and $\bar{A}_x$ are expected to assume higher values over the irrigated land, while $\sigma(\delta_x)$ and r_x are supposed to show lover values over irrigated areas. The modeled data has been involved in the clustering experiments to investigate whether it can add information in the irrigation mapping with respect to considering remotely sensed data only. Eight combinations of the input

parameters have been used to produce an equal number of classifications referred to May-September 2016 and 2017, for a total of sixteen experiments carried out. The performed experiments can be divided in two groups: one exploiting soil moisture only as input for the algorithm (clustering with two input parameters and three clusters) and another one merging information from modeled and remotely sensed soil moisture as input for the algorithm (clustering with three input parameters and three clusters). The maps resulting from this process have been validated according to two alternative validations, which are described in the following.

5.1.3.1 First Validation Procedure

As explained in Chapter 4, in the first validation procedure carried out the information about the irrigation attribute of the SIGPAC ground truth data set has been exploited to produce benchmark maps of dryland (D, corresponding to non-irrigated fields), irrigated areas (I, corresponding to irrigated fields), and forest or natural areas (F, corresponding to the remaining portions). These maps have been compared with those derived from the clustering process. It is noteworthy that the data outside the Catalan edges (not available in the ground truth data set), the urban areas, and the inland water bodies have been masked out before the validation. The confusion matrices synthetizing the performances of the various experiments in reproducing the ground truth are provided in Figure 5.9. In each matrix, referred to a specific experiment, the classes derived from the clustering process are provided on the X-axis, while on the Y-axis the ground truth classes are shown. High values along the matrices' diagonals indicate well-performing classifications.

During the highest-intensity irrigation period in 2016, overall better results are obtained for classifications exploiting SMAP at 1 km data rather than SMOS at 1 km data as input. The dryland area is satisfactory reproduced in all the experiments referred to the period May-September 2016, with percentages of dryland pixels well classified by the proposed method ranging between 61% and 83%. Several experiments show not-negligible confusion between forest or natural areas and irrigated land. Nevertheless, in the classification identified by the code ST.A.SMAP16, the 60% of natural pixels and the 51% of the irrigated pixels are well classified. Low rates of dryland pixels wrongly classified as irrigated pixels can be detected in all the experiments carried out, with percentages ranking between 0% and 7%; it is noteworthy that, in four classifications referred to the

highest-intensity irrigation season in 2016, this percentage is equal to 0%. The percentages of irrigated areas wrongly classified as dryland, ranging between 6% and 26% (a value higher than 20% is reached in one experiment only), are satisfactory. Hence, even if not all the experiments carried out are expected to work properly, the method provides overall satisfactory results in disentangling between irrigated areas and the dryland.
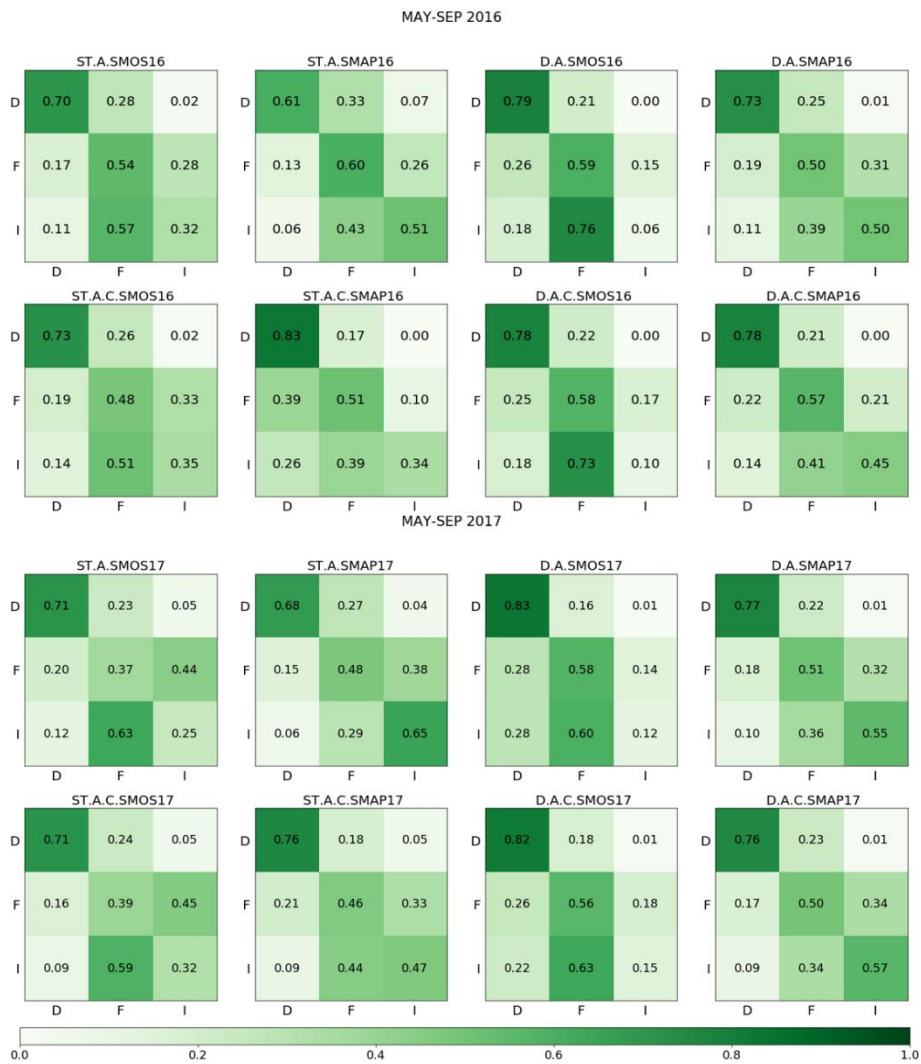
Figure 5.9. Confusion matrices resulting from the first validation referred to May-September 2016 (upper panel) and 2017 (lower panel). The ground truth classes are represented on the Y-axis, while the clustering-derived classes are shown on the X-axis. D indicates the dryland, F the forest or natural areas, and I the irrigated land (Dari et al., 2021a).

Similar results are obtained during the period May-September 2017. In the classifications referred to this period, the dryland is still well reproduced, with percentages ranging between 68% and 83%. Although in the experiment ST.A.SMAP17 the 65% of the ground truth irrigated pixels are well reproduced and in the classification with code D.A.SMOS17 the 58% of the forest or natural areas are well classified, confusion between natural and irrigated areas still persists in many experiments. The overall better performances of the experiments exploiting SMAP at 1 km data as input are confirmed, as well as the overall satisfactory performances in distinguishing irrigated areas from the dryland. In fact, the percentage of dryland pixels misinterpreted as irrigated varies between 1% and 5%; the rates of irrigated areas confused with the dryland range between 6% and 28% (values higher than 20% reached in two experiments only).

5.1.3.2 Second Validation Procedure

An alternative procedure exploiting the information on the crop type provided in the ground truth data set rather than the irrigation information has been performed. This validation, specific for summer crops, is based on the consideration that it may happen that a certain parcel carries the irrigation attribute associated to it, as it can be reached by the irrigation infrastructure, but it has not been actually irrigated during the focus period to which the clustering-derived maps have been produced, namely from May to September 2016 and 2017. In this second validation, SIGPAC-derived maps of selected summer crops (forage, fruit trees, and summer cereals), other crops, and remaining portions have been used as benchmark maps of irrigated areas (I), dryland areas (D), and forest or natural areas (F), respectively. The confusion matrices referred to the second validation carried out in this study are shown in Figure 5.10.

For both focus periods, a systematic enhancement in the classification of irrigated areas and of the natural areas along with slightly less-performing detections of the dryland can be observed. The percentages of dryland pixels properly classified during May-September 2016 range between 54% and 78%, while during May-September 2017 the percentage varies between 60% and 78%. For both considered highest-intensity irrigation periods, the experiment configuration that best represent the forest or natural areas is the same: D.A.SMOS16 in 2016 (62% of natural pixels well classified) and D.A.SMOS17 in 2017 (59% of natural pixels well reproduced). The best performing experiments in correctly classifying the

irrigated areas are: ST.A.SMAP16 (65% of irrigated pixels well classified) and ST.A.SMAP17 (78% of irrigated pixels well recognized).
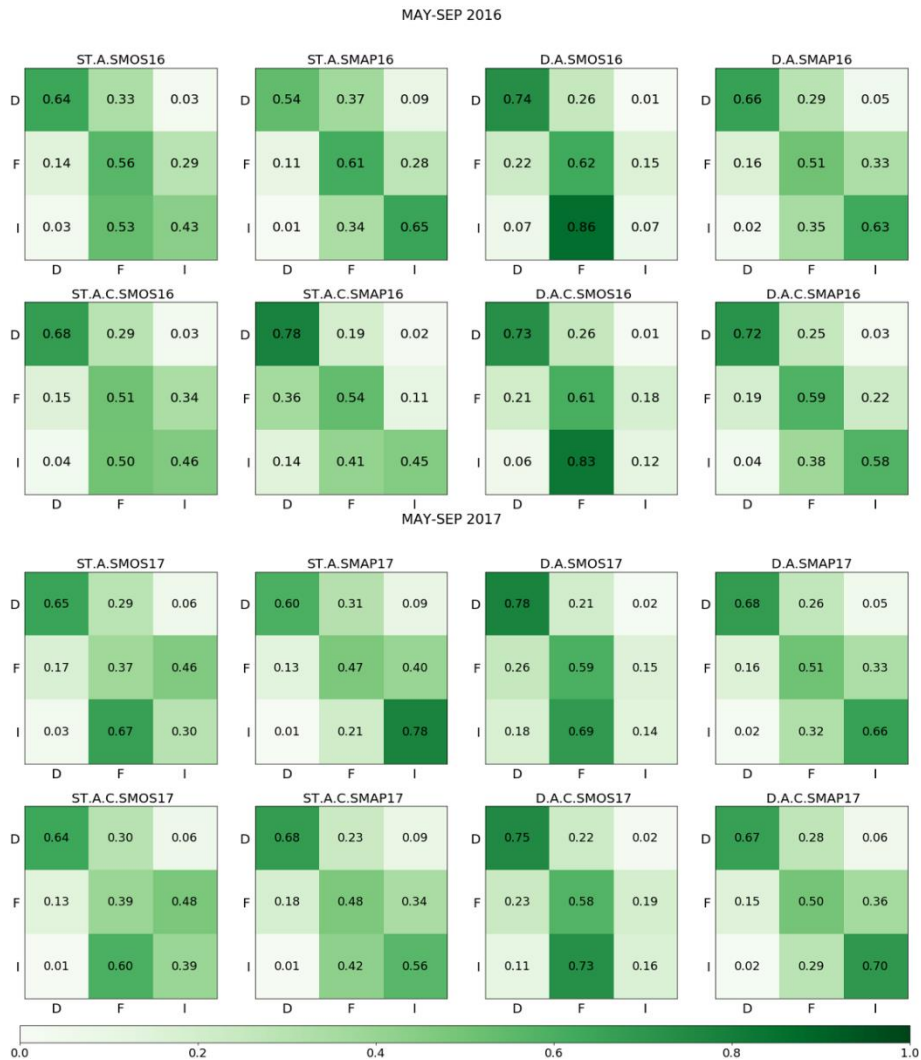
Figure 5.10. Confusion matrices resulting from the second validation referred to May-September 2016 (upper panel) and 2017 (lower panel). The ground truth classes are represented on the Y-axis, while the clustering-derived classes are shown on the X-axis. D indicates the dryland, F the forest or natural areas, and I the irrigated land (Dari et al., 2021a).

The overall better performances obtained for experiments exploiting SMAP at 1 km data as input, as well as the almost total lack of confusion between irrigated areas and the dryland are common aspects between the two validations carried out. In fact, in this second validation the rate of dryland pixels confused with irrigated pixels varies between 1% and 9% during the focus period in 2016 and between 2% and 9% during the focus period in 2017. The percentage of irrigated

pixels misinterpreted as dryland ranges between 2% and 14% during the focus period in 2016 and between 1% and 18% during the focus period in 2017. It is noteworthy that not negligible percentages of irrigated pixels wrongly classified as forest or natural pixels still persist.

5.1.3.3 Sensitivity to the Aggregation Threshold

As thoroughly explained in Chapter 4, the ground truth data set used in this analysis has been aggregated from a plot scale to 1 km resolution in order to be compared with the clustering-derived maps. In order to assess the loss of information due to this pre-processing step and how it impacts on the performances of the proposed classifications, two data sets containing binary information have been derived from the irrigation and the crop type attributes used to perform the validations. Each data set contains the irrigated crops only and the summer crops only, respectively, within the irrigable lands. These data sets have been obtained through two steps. In the first one, the plot scale data have been projected on a 100 m spatial resolution regular grid; then, the 100 m resolution data have been aggregated at 1 km by assigning to each 1 km × 1 km pixel the irrigated class (or the summer crops class) in presence of rates of 100 m × 100 m pixels contained in it higher than 30%, 40%, 50%, 60% of the total. Sixteen alternative ground truth data sets (eight for 2016 and eight for 2017) have been obtained through this procedure; they contain information on irrigated pixels or summer crops pixels only at different aggregation thresholds: 0.3, 0.4, 0.5, and 0.6. Figure 5.11 provides the percentages of the irrigated pixels (or summer crops pixels) well classified by the clustering for the different aggregation thresholds considered.

For both kinds of exploited information and both focus periods, the already well performing classifications further increase the related scores, even reaching the 90% of pixel with summer crops well recognized by the clustering. Conversely, the adoption of less restrictive aggregation thresholds does not reflect in an enhancement of the already unsatisfactory performing experiments. What proposed in this section is a simplified experiment, in which only binary distinctions and not three classes are concurrently adopted, but it provides the magnitudes of the partial loss of information that occurs in the aggregation of the plot-scale-born data set to the remotely sensed data resolution (1 km). Furthermore, this experiment further validates the capability of the proposed method in reproducing well homogeneous irrigation patterns.
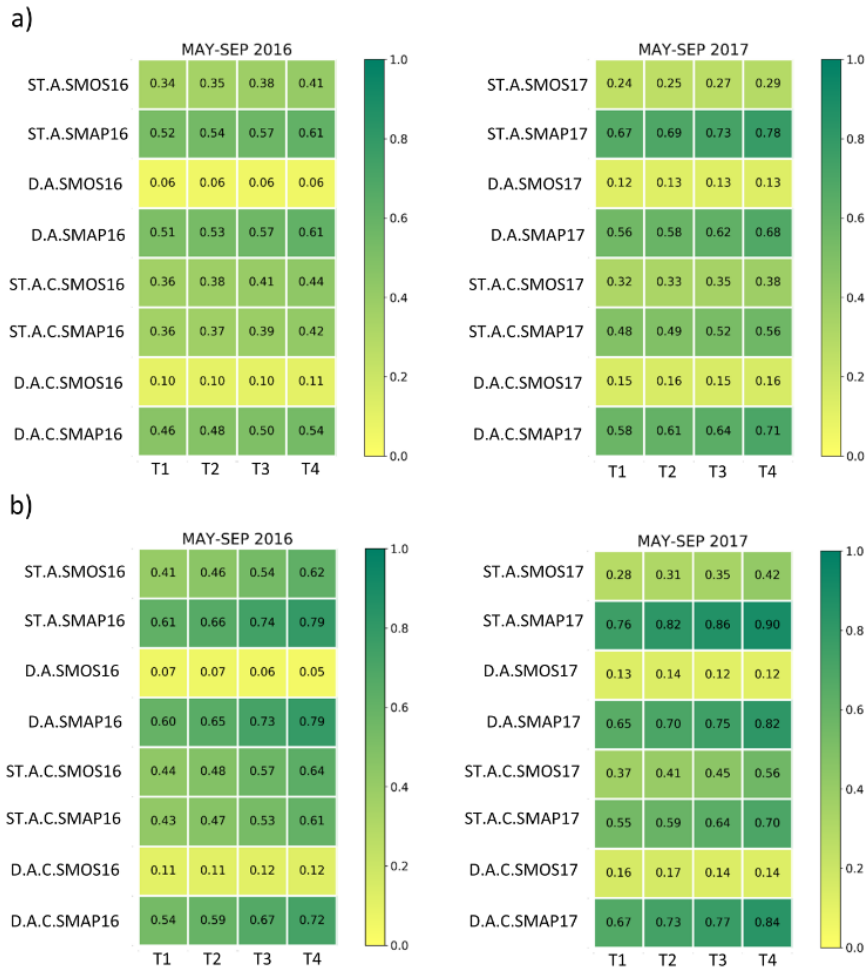
Figure 5.11. Heatmaps representing the classification accuracy of the irrigated pixels at different aggregation thresholds (T1 = 0.3, T2 = 0.4, T3 = 0.5, T4 = 0.6) considering: a) all the pixels inside the irrigable land marked as irrigated in the ground truth data set (SIGPAC) and b) only the pixels in the same domain carrying the information about the selected summer crops: forage, summer cereals, and fruit trees (Dari et al., 2021a).

5.1.3.4 Definitive Classifications

Among all the experiments carried out, whose results have been presented in the Sections 5.1.3.1 and 5.3.1.2, the best ones for each focus period have been kept as definitive classifications. According to both validation procedures, the best performing experiments exploit the same input parameters. For each focus period, two classifications have been selected: the experiment that overall best reproduces the irrigated land, namely ST.A.SMAP16 for 2016 and ST.A.SMAP17 for 2017, and the best-performing experiment in well classifying all the three classes concurrently, namely D.A.C.SMAP16 for 2016 and D.A.C.SMAP17 for 2017. The

definitive classifications proposed, together with the reference ground truth maps, are provided in Figure 5.12. The irrigated areas are represented in blue, the dryland in brown, and the forest or natural areas in green; the irrigation canals network is also shown (magenta lines). As explained in Chapter 4, inland water bodies and cities have been masked out. The maps also show the border which separates Catalonia, for which the ground truth data set is available, and Aragon, over which it has not been possible to quantitatively validate the proposed maps. Despite good agreement between the proposed classifications and the benchmark can be observed, some disturbances due to a system of reservoirs in the North side and to the presence of evergreen forests in the South-East can be detected.

5.1.4 Discussion and Remarks

The activity aimed to detect and map irrigation over the study area in the Ebro basin provide an assessment of the best performing products among those evaluated; furthermore, a method to map irrigated areas is proposed. The enhanced resolution L-band passive microwave based products prove to be the most skilful ones in detecting irrigation over the pilot area. The analysis of the spatial dynamics of soil moisture, carried out through the spatial relative differences, indicates SMOS at 1 km as the best performing product over the Catalan and Aragonese area and SMAP at 1 km as the most capable to detect irrigation over the Urgell area. The analysis of the temporal dynamics of soil moisture, carried out through the temporal anomalies, shows a strong irrigation-related pattern for both SMAP and SMOS at 1 km during May-September 2016 over the Urgell, where flood irrigation is the most employed technique. The same pattern is not observed for SMOS at 1 km during the focus period in 2017, because of a source of RFI detected in the Urgell since the end of 2016 onwards and not properly solved by the post-processing through the RFI filter. The probability of RFI occurrence over the Urgell area is provided in Figure 5.13. Starting from the second half of 2016, the RFI probability begins increasing up to values of ~0.7 reached in 2017. It is noteworthy that this issue does not affect SMOS at 1 km data over the Catalan and Aragonese area during 2016. The SMAP at 1 km data is not affected by RFI because SMAP's radar and radiometer electronics, as well as the algorithms, are more recent than the SMOS mission. Hence, on the basis of the SMOS mission experience, the SMAP mission has been designed to include on board filters to mitigate RFI effects (Entekhabi et al., 2010).

a)

b)
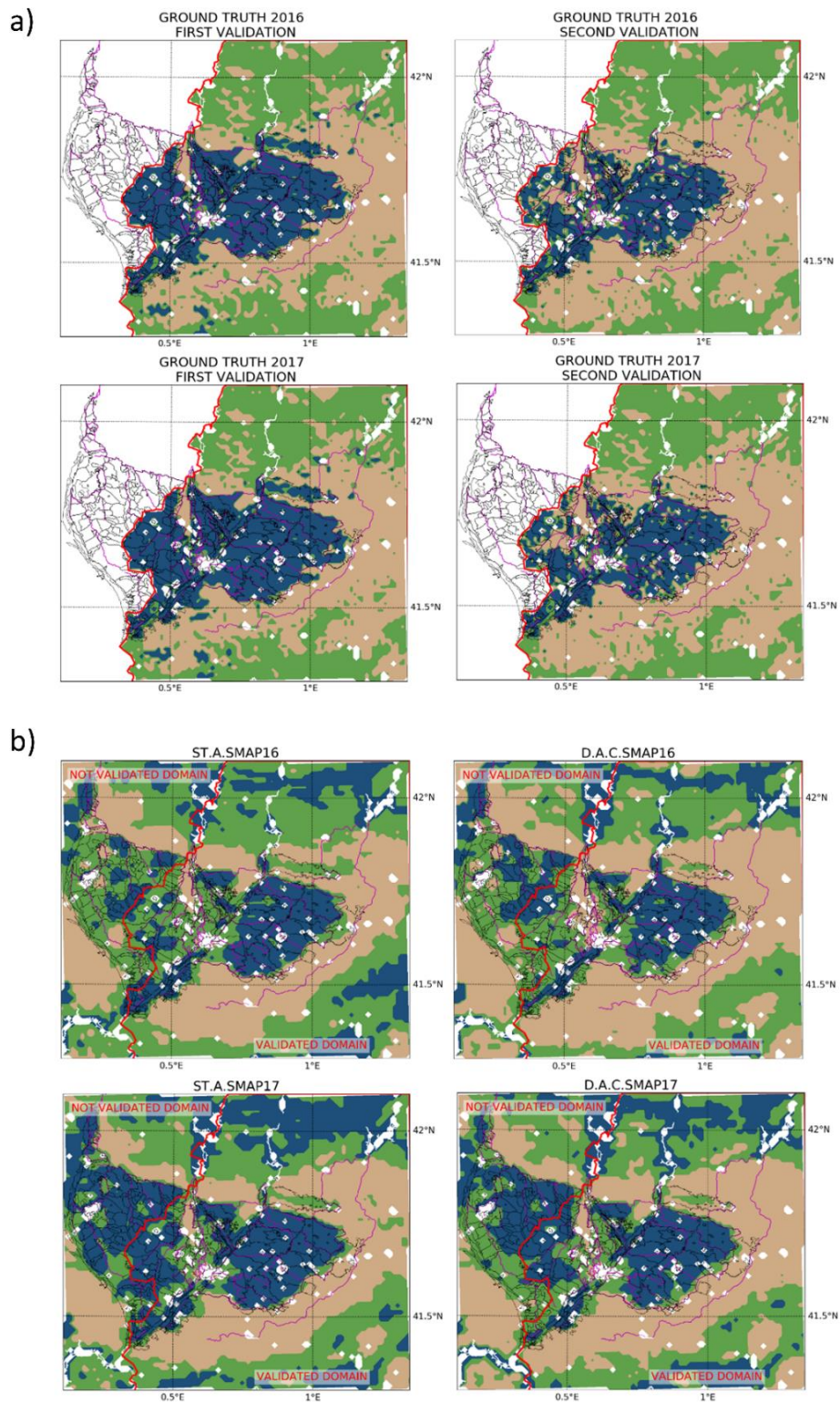
Figure 5.12. Ground truth (a) and definitive clustering derived (b) maps for the periods May-September 2016 and May-September 2017. The irrigated areas are represented in blue, the forest or natural areas in green and the dryland in brown (Dari et al., 2021a).

101
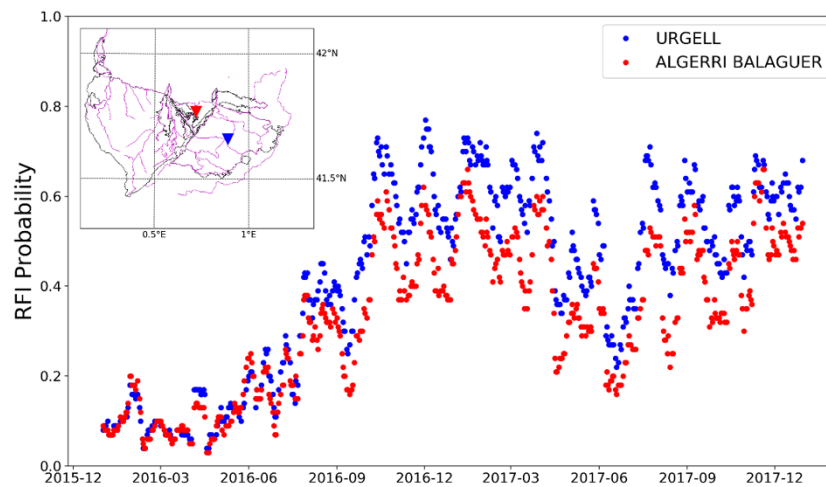
Figure 5.13. Time series of the probability of RFI occurrence referred to two locations: Algerri-Balaguer (red) and Urgell (blue). Taken from Dari et al. (2021a).

Sentinel- 1 provides unsatisfactory performances in both spatial and temporal analyses; this issue can be mainly attributed to a higher sensitivity to surface characteristics (e.g., the roughness and the vegetation cover) characterizing the C-band SAR data with respect to observations retrieved by L-band passive sensors. A complementary reason for the unsatisfactory performances obtained with Sentinel-1 can be the missing implementation of corrections for seasonal vegetation effects in the retrieval algorithm. The coarser resolution products evaluated (SMAP and ASCAT) are not able to detect the finer-scale differences existing over the pilot site landscape and thus spotting irrigation, mainly because of their resolution. In fact, these products showed potential in detecting irrigation over large areas in the continental US (Kumar et al., 2015; Lawston et al., 2017).

As a difference with many existing classification methods that need training processes before to be applied or decision tree structures (Thenkabail et al., 2007; Ozdogan and Gutman, 2008; Jin et al., 2016; Teleguntla et al., 2017), the methodology proposed in this thesis does not require any training. Its strength relies on the temporal stability derived indices, which are expected to assume precise different behaviours over the irrigated land and over the other surfaces. Both procedures adopted in the performed study point out the capability of the method in separating irrigated areas from rainfed agricultural areas. This aspect is very useful to spot the actually irrigated portion of areas known to be equipped for irrigation. The recursive confusion occurring between irrigated areas and forest or natural areas represents the main limitation of the proposed methodology. The

rate of forest or natural pixels wrongly classified as irrigated pixels in the North of the focus area is mainly attributable to a system of reservoirs providing water to the irrigation districts. These water bodies alter the soil wetness conditions retrieved by the satellite and leads to wrong classifications. The percentages of irrigated pixels wrongly classified as natural pixels are mainly due to the limits of the methods in adequately reproducing areas where fruit trees are the main cultivation and strongly mixed areas, like the one located in the North of the Urgell, where fruit trees coexist with abandoned fields and corn crops. Nevertheless, the fact that these areas are misinterpreted as natural areas instead of dryland is comforting. The wrong classification of fruit trees, already experienced in Gao et al. (2018), is mainly attributable to the irrigation technique employed; areas where fruit trees exist are drip irrigated, so they generally result less humid than areas destined to other crops. This issue determines a wrong classification during the clustering.

The clustering experiments highlight better performances of SMAP at 1 km with respect to SMOS at 1 km. Although if the higher accuracy of coarse resolution SMAP data with respect to coarse SMOS data is a well-known issue (Chen et al., 2018), both the DISPATCH downscaled versions of the products perform well in detecting irrigation, but in the clustering the RFI problems affecting the SMOS at 1 km product make its performances drop down.

Finally, the analysis on the sensitivity to the aggregation threshold highlights that the adoption of less restrictive thresholds when aggregating the ground truth data to 1 km lead to a gain in accuracy for already well performing experiments only.

The following remarks can be drawn from the above discussed results:

1. The spatial scale of the irrigation practices over the pilot area in the Ebro basin point out the need of high-resolution (1 km or less) soil moisture data sets to detect irrigation;
2. the temporal stability derived indices are suitable to evaluate the capability to detect irrigation of remotely sensed products, as they express the spatial-temporal dynamics of soil moisture;
3. SMOS and SMAP at 1 km are the best performing products in detecting irrigation; the downscaling through MODIS optical data surely represents an enhancement making the DISPATCH downscaled products able to obtain reliable information on where irrigation actually occurs;

4. the proposed methodology is particularly performing in disentangling irrigated areas from rainfed areas;

5. for both focus periods, the best classifications are the same; more in detail, ST.A.SMAP16 and ST.A.SMAP17 are the experiments that best reproduce the irrigated areas and exploit remotely sensed soil moisture only. This is comforting, as a very low number of models running at 1 km over large regions exist;

6. the experiments D.A.C.SMAP16 and D.A.C.SMAP17 are those that overall best reproduce all the three classes concurrently; note that they merge modeled and remotely sensed soil moisture as input.

5.2 Results in the Upper Tiber Basin

In this section, the results obtained over the agricultural pilot areas in the Upper Tiber basin are presented. The more complex topography of this case study with respect to the study area in the Ebro basin has led to the choice of performing a double-scale analysis. The results obtained from analyses carried out at 1 km spatial resolution are provided in Section 5.2.1, while Section 5.2.2 describes the results obtained at a plot scale. Discussion and remarks are provided in Section 5.2.3. Henceforth, the Sentinel-1 product at 1 km delivered by the Copernicus Global Land Service is called "Copernicus Sentinel-1", while the plot-scale data set produced by THEIA and aggregated at 1 km is called "THEIA Sentinel-1 at 1 km". The 100 m aggregated version used in the field scale analysis is called "THEIA Sentinel-1". The DISPATCH downscaled SMAP data set is called "SMAP at 1 km", in accordance with the previously described analysis. Table 5.3 summarizes the main characteristics of the remote sensing soil moisture used.

Table 5.3. Overview of the main features of the remote sensing soil moisture products used in the double-scale analysis aimed to evaluate the detectability of irrigation over the pilot area in the Upper Tiber basin: sensor aboard the satellite, operating band, and spatial resolution.

Product	Sensor	Operating Band	Spatial Resolution
SMAP at 1 km	radiometer radar – not working	radiometer: L-band (1.4 GHz) radar: L-band (1.26 GHz) – not working	1 km – downscaled through the DISPATCH algorithm
Copernicus Sentinel-1	SAR	C-band (5.4 GHz)	1 km
THEIA Sentinel-1 at 1 km	SAR	C-band (5.4 GHz)	Plot-scale obtained by merging with Sentinel-2, aggregated at 1 km
THEIA Sentinel-1	SAR	C-band (5.4 GHz)	Plot-scale obtained by merging with Sentinel-2, aggregated at 100 m

5.2.1 Analysis at 1 km Spatial Resolution

The main aim of the analysis at 1 km is to investigate if products at this spatial resolution are capable to detect irrigation occurring at the scale of the agricultural sites in the Upper Tiber basin. The 1 km resolution has proven to be suitable to detect irrigation practices over the pilot area in the Ebro basin; hence, this analysis represents an extension of the proposed methodology over a more complex area. For this reason, the same approach has been adopted; namely, the detectability of irrigation by the considered products has been carried out by investigating the spatial and temporal dynamics of retrieved soil moisture through the temporal stability derived indices. Again, the surface soil moisture output from SURFEX-ISBA simulations has been involved into the analysis with the aim of representing a not irrigated benchmark situation.

Figure 5.14 shows the weekly time series of the spatial relative differences averaged over the four pilot agricultural areas (see Figure 3.5). For each domain, the spatially-averaged time series of the NDVI are also provided. Note that the modeled soil moisture data set ends in September 2019.
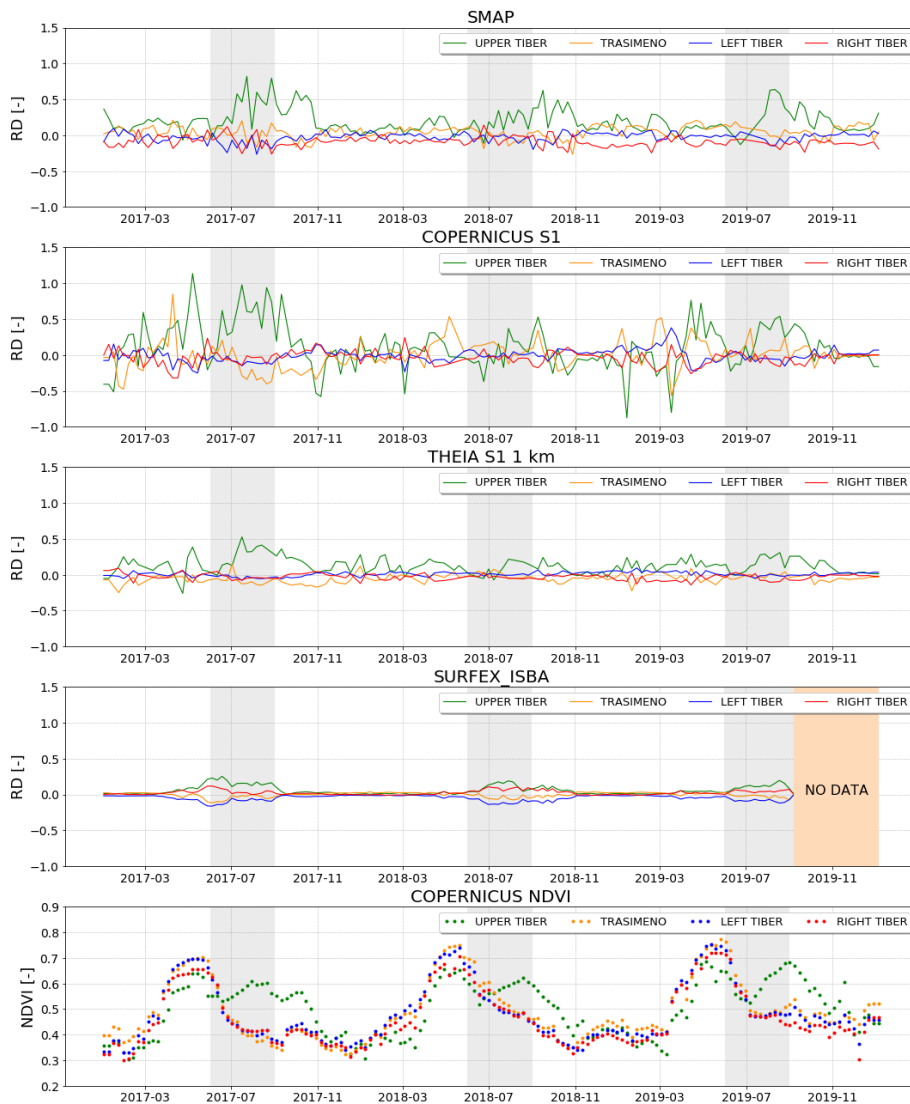
Figure 5.14. Weekly time series of the spatial relative differences according to all the considered data sets and averaged over the four pilot agricultural areas: Upper Tiber, Trasimeno, Left Tiber, and Right Tiber. For each domain, the spatially-averaged time series of the NDVI are also shown (adapted from Dari et al., 2021b).

As explained in Section 5.1.1, if a remotely sensed soil moisture product carries the irrigation information, it is expected to show high anomaly values of relative differences during the highest irrigation intensity season, corresponding in this case with the period June-September. Note that the comparison between the irrigated land and the dryland performed for the study area in Spain is not possible over this case study. In fact, in the Upper Tiber basin, large uniform irrigated and not irrigated zones in clear contrast to each other and with similar topographic features do not exist. Actually, the irrigated and not irrigated portions within the

pilot agricultural areas are highly mixed together. For this reason, it is interesting to investigate if products at 1 km spatial resolution are skilful enough in adequately solving the signal from adjacent irrigated and not irrigated areas. The performed spatial analysis provides promising results over the Upper Tiber agricultural area for all the remotely sensed data sets evaluated. Increases in spatial relative differences can be detected for the SMAP at 1 km data during the focus periods in 2017, 2018, and 2019. Copernicus Sentinel-1 show a similar behaviour in 2017 and 2019. During June-September 2018, the spatially averaged values of the relative differences remain lower than during the same period of the remaining considered years. The THEIA Sentinel-1 at 1 km data set shows a behaviour similar to the one observed for the Copernicus Sentinel-1 data, with positive relative differences over the Upper Tiber area during the highest-intensity irrigation season clearer in 2017 and 2019 with respect to 2018. An interesting result is that an analogous behaviour can be observed in the time series of modeled soil moisture over the Upper Tiber area and the Right Tiber area; this data set surely does not contain the irrigation information. This issue leads us to think that the promising results obtained by the spatial analysis at 1 km over the Upper Tiber agricultural area are not exclusively attributable to irrigation. The fact that positive relative differences are detected during June-September for the SURFEX-ISBA data set also suggests that the results obtained through the remotely sensed data sets are affected by static patterns (e.g. soil texture). Another factor potentially affecting the promising results over the Upper Tiber agricultural area can be deduced by the NDVI time series (lower panel of Figure 5.14). For all the pilot agricultural portions except for the Upper Tiber, only one peak during spring can be observed. Conversely, over the Upper Tiber area, after the first peak in spring, the spatially-averaged NDVI rises again. This behaviour can be likely attributed to the irrigated crops, more uniformly distributed over the Upper Tiber area with respect to the others considered in this study. This trend seems to be reflected in the SMAP at 1 km and THEIA Sentinel-1 km data sets, both produced by merging the soil moisture information with the NDVI. Hence, if from one hand the vegetation conditions may affect the results, on the other they corroborate the district-scale signal detected by almost all the evaluated products and partly attributable to irrigation. In fact, well-developed vegetation is expected where irrigation occurs.

The spatial averages at the scale of the agricultural areas can bring to a loss of information about irrigation events occurring over sub-areas, especially if the spatial scale at which the irrigation practices generally occur over these districts is

considered. For this reason, the maps of the mean spatial relative differences during the periods June-September of 2017, 2018, and 2019 have been produced (see Figure 5.15). The maps help in detecting portions of the pilot agricultural areas showing positive relative differences during the highest-intensity irrigation season that can be interpreted as an irrigation track contained into the remotely sensed soil moisture data sets.
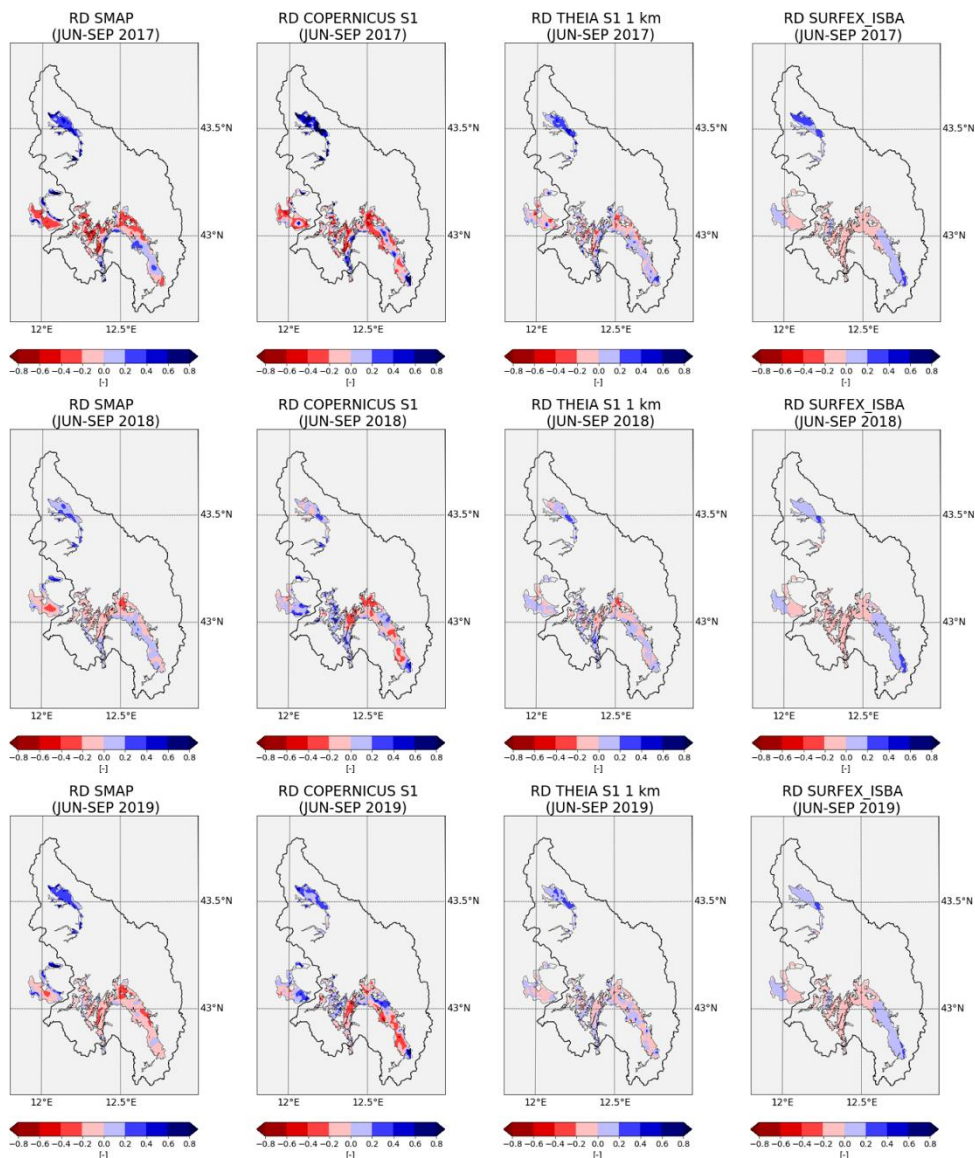
Figure 5.15. Maps of the spatial relative differences averaged during the periods June-September 2017 (upper panel), 2018 (middle panel), and 2019 (lower panel). Derived from Dari et al. (2021b).

For the SMAP at 1 km data set, positive relative differences can be observed over the Upper Tiber area for all the three focus years. Recursive patterns of relative

differences higher than zero can be observed over the Trasimeno area; this result may be affected by the adjacent lake. The Right Tiber area is generally drier than the others according to this metric. Except for pattern of slightly positive relative differences in the highest irrigation intensity season in 2017 and 2018, dry conditions are detected for the Left Tiber area also. Both versions of Sentinel-1 considered in this study provide mean positive relative differences over the Upper Tiber area in June-September 2017 and 2019, less in 2018. Recursive areas where the considered index shows values higher than zero can be detected in the Trasimeno area and in the Right Tiber area for the Copernicus Sentinel-1 data set in June-September 2018 and 2019. Scattered low-entity positive relative differences areas can be observed for THEIA Sentinel-1 at 1 km data. In the maps referred to the SURFEX-ISBA outputs, patterns of positive relative differences are obtained over the Upper Tiber area and portions of the Trasimeno and Left Tiber areas; surely, these results are not attributable to irrigation. Hence, the modeled soil moisture is a useful support to correctly interpret the remote sensing derived results. However, the patterns of positive relative differences are characterized by low values (less than 0.2). This issue suggests that the promising results obtained over the Upper Tiber area, which are common to almost all the remotely sensed products, are influenced but not fully determined by static pattern also reproduced by the model. The analysis in terms of temporal anomalies can help in disentangling the effects due static features from other factors (e.g., irrigation). The weekly time series of the temporal anomalies averaged over the pilot agricultural areas are shown in Figure 5.16.

No irrigation signals can be deduced from the trends of the temporal anomalies averaged over the pilot agricultural areas. In fact, all the considered products show, for each pilot area, lower temporal anomalies in the dry season with respect to the rest of the year, as expected in absence of irrigation. As already explained, by only looking at spatial means can be misleading, especially over topographically complex and highly-mixed areas. Hence, maps of the temporal anomalies averaged during the period June-September of 2017, 2018, and 2019 have been produced (see Figure 5.17). Positive or close-to-zero mean temporal anomalies detected during the highest-intensity irrigation periods are attributable to irrigation practices. In fact, positive or close-to-zero values of this metric indicate that a certain pixel is wetter than or close to its 3-years temporal mean during a period naturally expected to be dry.
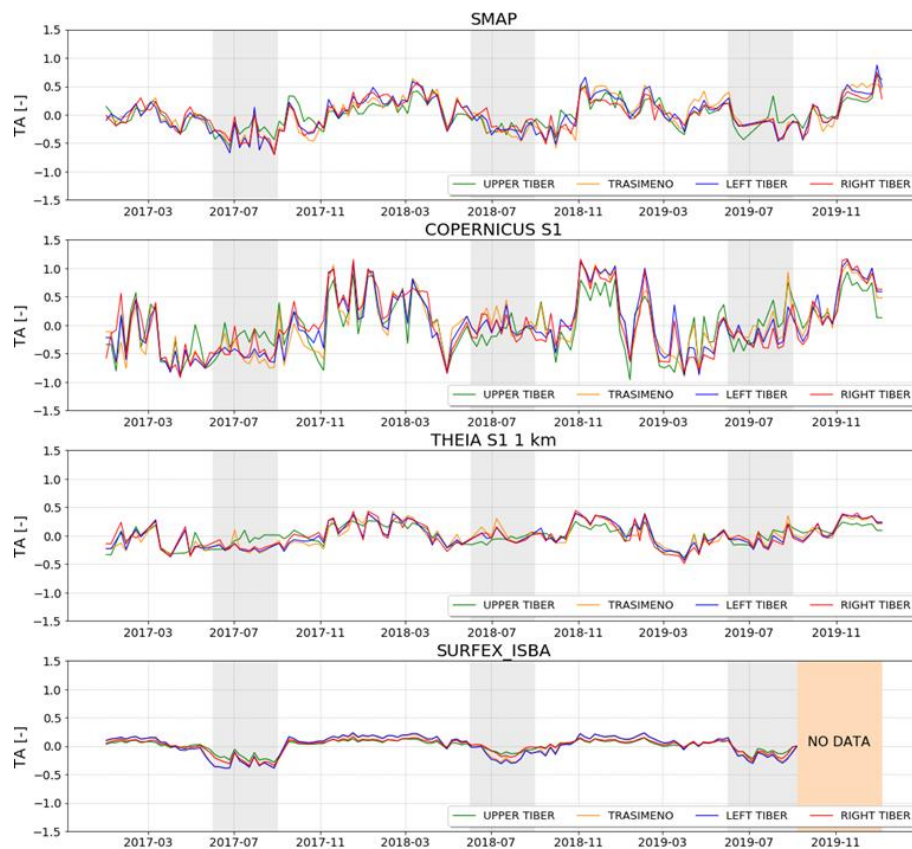
Figure 5.16. Weekly time series of the temporal anomalies according to all the considered data sets and averaged over the pilot agricultural areas: Upper Tiber, Trasimeno, Left Tiber, and Right Tiber (adapted from Dari et al., 2021b).

In general, a drier condition in 2017 with respect to 2018 and 2019 is observed for all the data sets, including the SURFEX-ISBA modeled soil moisture. No positive patterns of mean temporal anomalies are detected for the SMAP at 1 km data set; however, slightly negative (less than -0.1 or –0.2) values can be observed for the Upper Tiber and the Left Tiber areas during June-September 2018 and 2019. The two Sentinel-1 versions show similar patterns, especially in June-September 2018 and 2019. Slightly negative values are detected over the Upper Tiber area and scattered areas where positive temporal anomalies are obtained can be observed. The model shows evenly distributed dry conditions, as expected by a modeled data set during the summer season. Note that in this case negative close-to-zero values are not an irrigation signal, but the result of the smaller range of variability characterizing the modeled data with respect to remotely sensed observations.

110
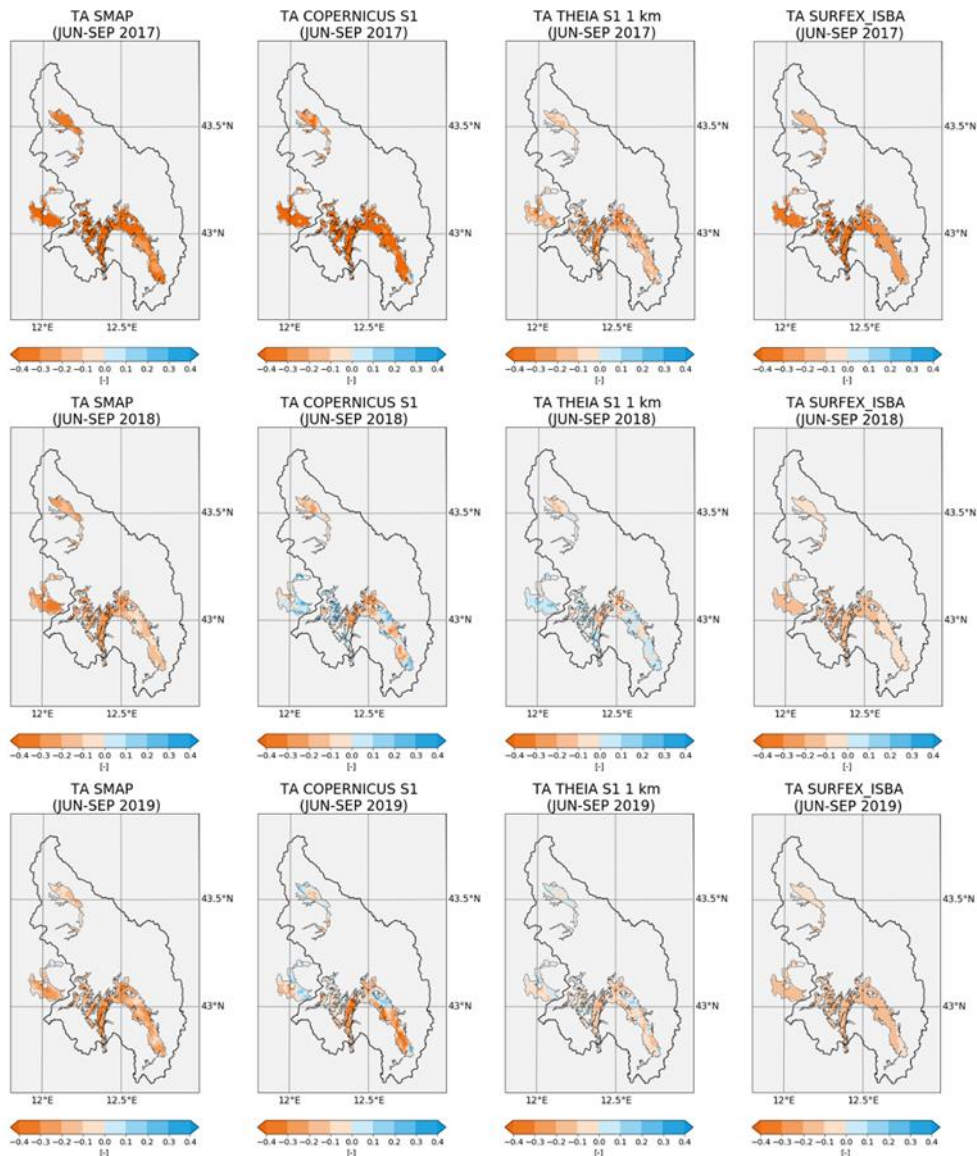
Figure 5.17. Maps of the temporal anomalies averaged during the periods June-September 2017 (upper panel), 2018 (middle panel), and 2019 (lower panel). Adapted from Dari et al. (2021b).

5.2.2 Analysis at a Plot Scale Spatial Resolution

The analysis at a plot scale (100 m) spatial resolution, for which the THEIA Sentinel-1 product has been used, allows to investigate the spatial-temporal dynamics of soil moisture over the single agricultural field. Figures 5.18 and 5.19 show the spatial relative differences and the temporal anomalies, respectively, averaged during June-September 2017, 2018, and 2019.
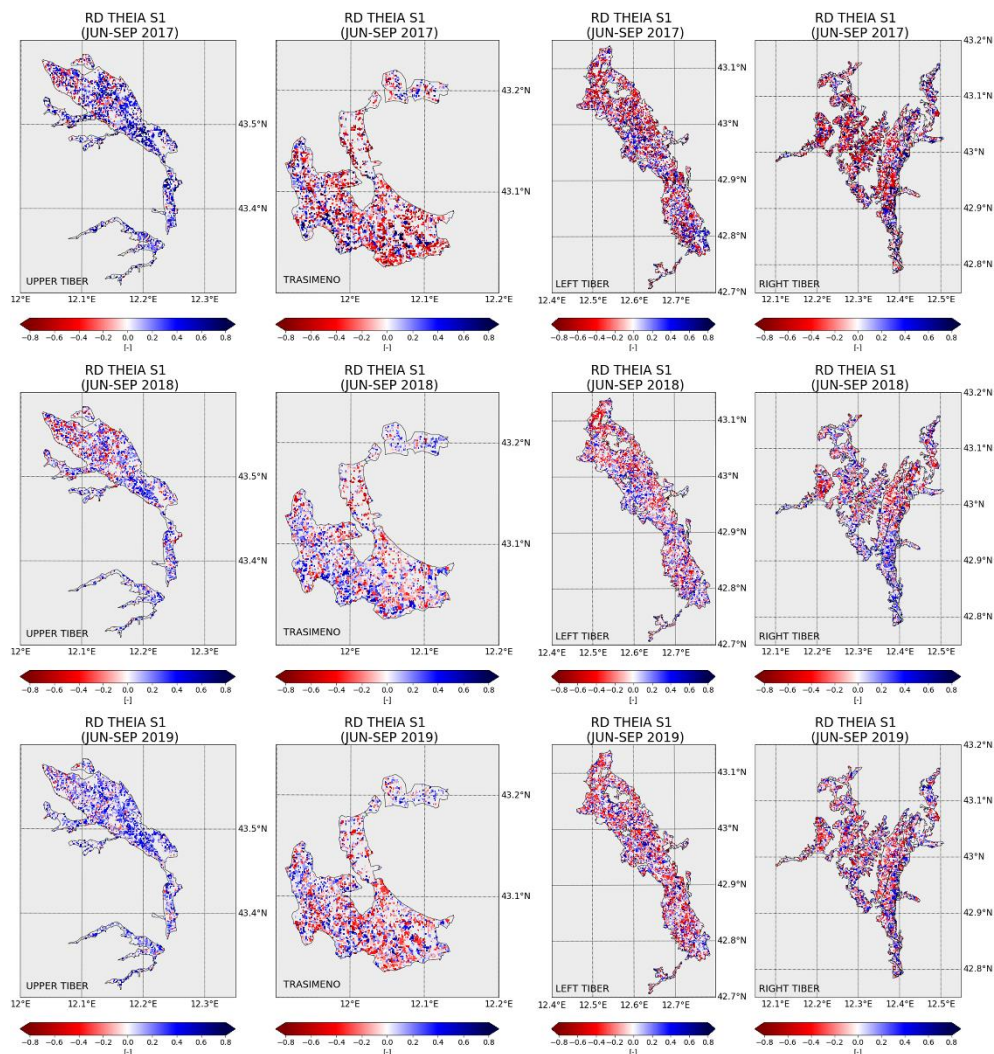
Figure 5.18. Maps of the spatial relative differences averaged during the periods June-September 2017 (upper panel), 2018 (middle panel), and 2019 (lower panel). For each agricultural pilot area (Upper Tiber, Trasimeno, Left Tiber, and Right Tiber), a dedicated map has been produced (Dari et al., 2021b).

In this case, because of the considered spatial resolution, the maps are provided for each agricultural area separately. Despite this, the information is too much detailed to analyse the obtained results as previously done for the analysis at 1 km spatial resolution. Nevertheless, an overall good agreement between the spatial and the temporal analysis can be observed. The K-means clustering algorithm represents a useful tool to synthetize the results obtained for this fine-resolution analysis and to support the related discussion. A binary classification of irrigated and non-irrigated areas has been produced by exploiting the mean spatial relative differences and the mean temporal anomalies during June-September 2017, 2018,

and 2019 as input data points. Hence, a classification considering two clusters and two input parameters (shown in Figures 5.18 and 5.19) has been performed.
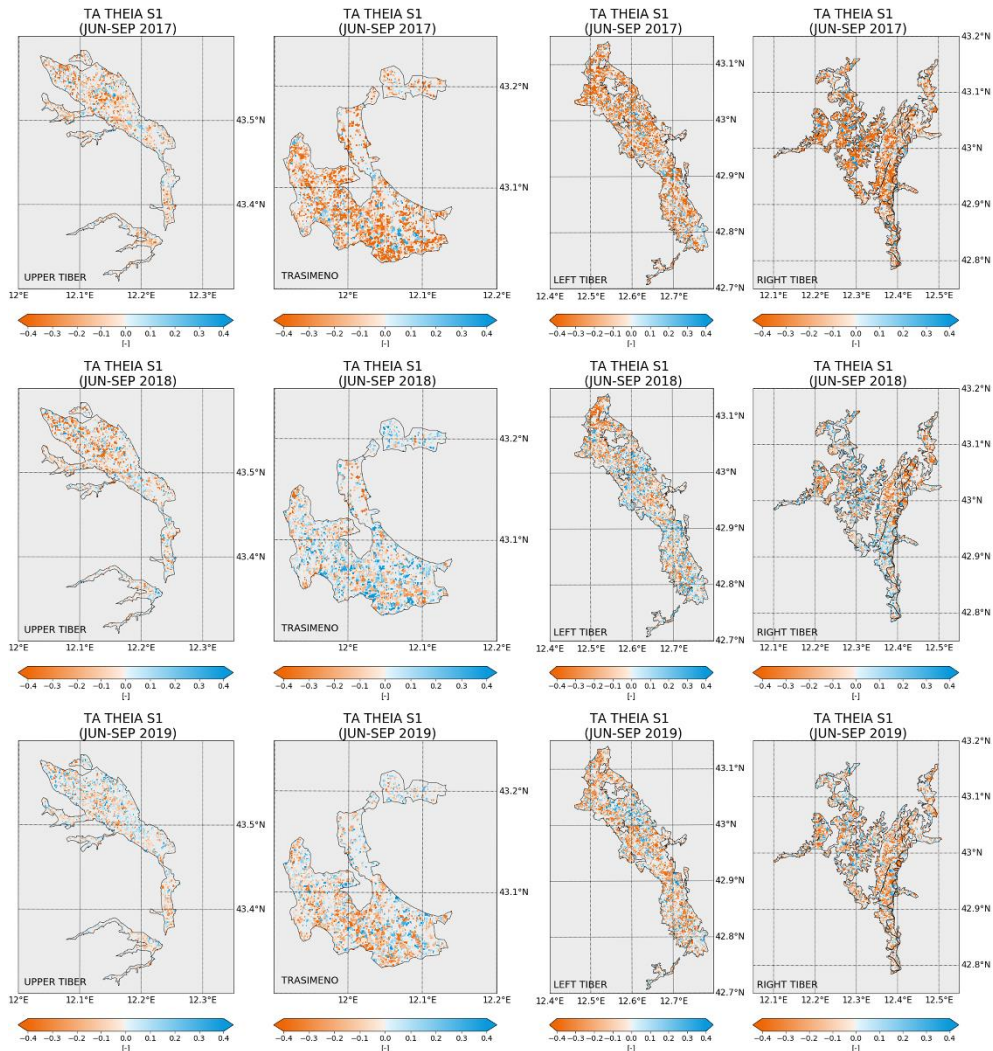
Figure 5.19. Maps of the temporal anomalies averaged during the periods June-September 2017 (upper panel), 2018 (middle panel), and 2019 (lower panel). For each agricultural pilot area (Upper Tiber, Trasimeno, Left Tiber, and Right Tiber), a dedicated map has been produced (Dari et al., 2021b).

The results of the K-means clustering are shown in Figure 5.20, where fields classified as irrigated are represented in green and fields classified as not irrigated are shown in brown. A first interesting result emerging from the classification maps is the high rate of fields classified as irrigated over the Upper Tiber area during all the three focus periods in 2017, 2018, and 2019. This agricultural area is known to be the most evenly cultivated and irrigated one among those evaluated in this study. Sunflowers, maize, and mostly tobacco are cultivated. The performed

classification reproduces well the irrigation density expected for the Upper Tiber area. Unfortunately, despite the detail of the information reached with the filed-scale analysis and thus its potential utility, a comprehensive validation cannot be performed over the Upper Tiber basin case study. In fact, a detailed irrigation-related data set, as the SIGPAC crops maps available for Catalonia, does not exist for the considered study area. Hence, the few information on irrigation practices collected over four pilot fields have been used to test the robustness of the proposed classification. According to the ground truth irrigation data (see Figure 4.13) the UT1 field should result irrigated in 2017 and 2018, not in 2019. Conversely, UT2 should be classified as irrigated in 2018 and 2019, not in 2017. Finally, for the LT1 and LT2 pilot fields, only the data for 2019 is available; both fields should be classified as irrigated. The performances of the clustering-derived classification are shown in the scatter plots provided in Figure 5.21.
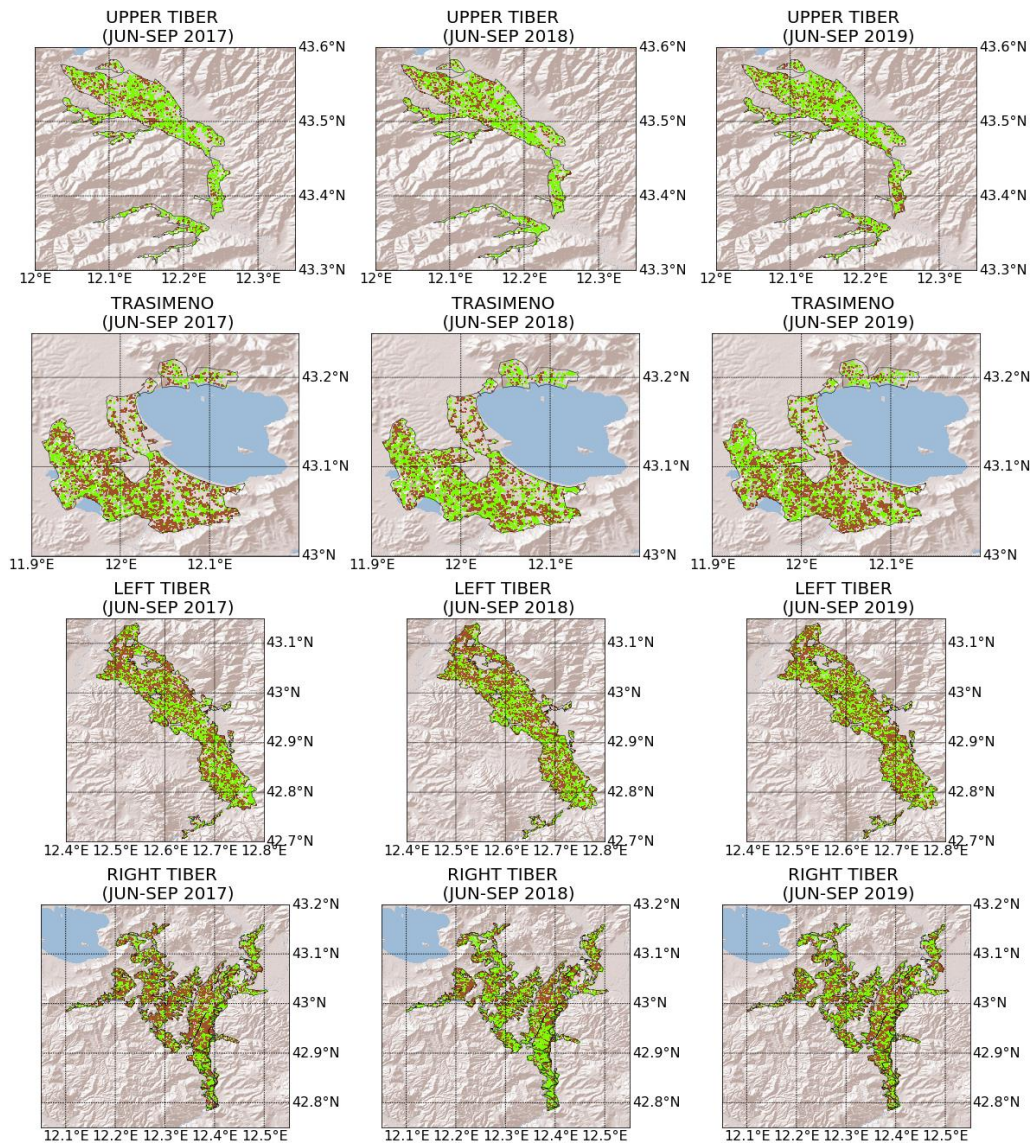
Figure 5.20. Maps of the clustering-derived classifications during the periods June-September 2017 (left column), 2018 (middle column), and 2019 (right column); each row is referred to a pilot agricultural area. Irrigated pixels are represented in green, while not irrigated ones are shown in brown (Dari et al., 2021b).
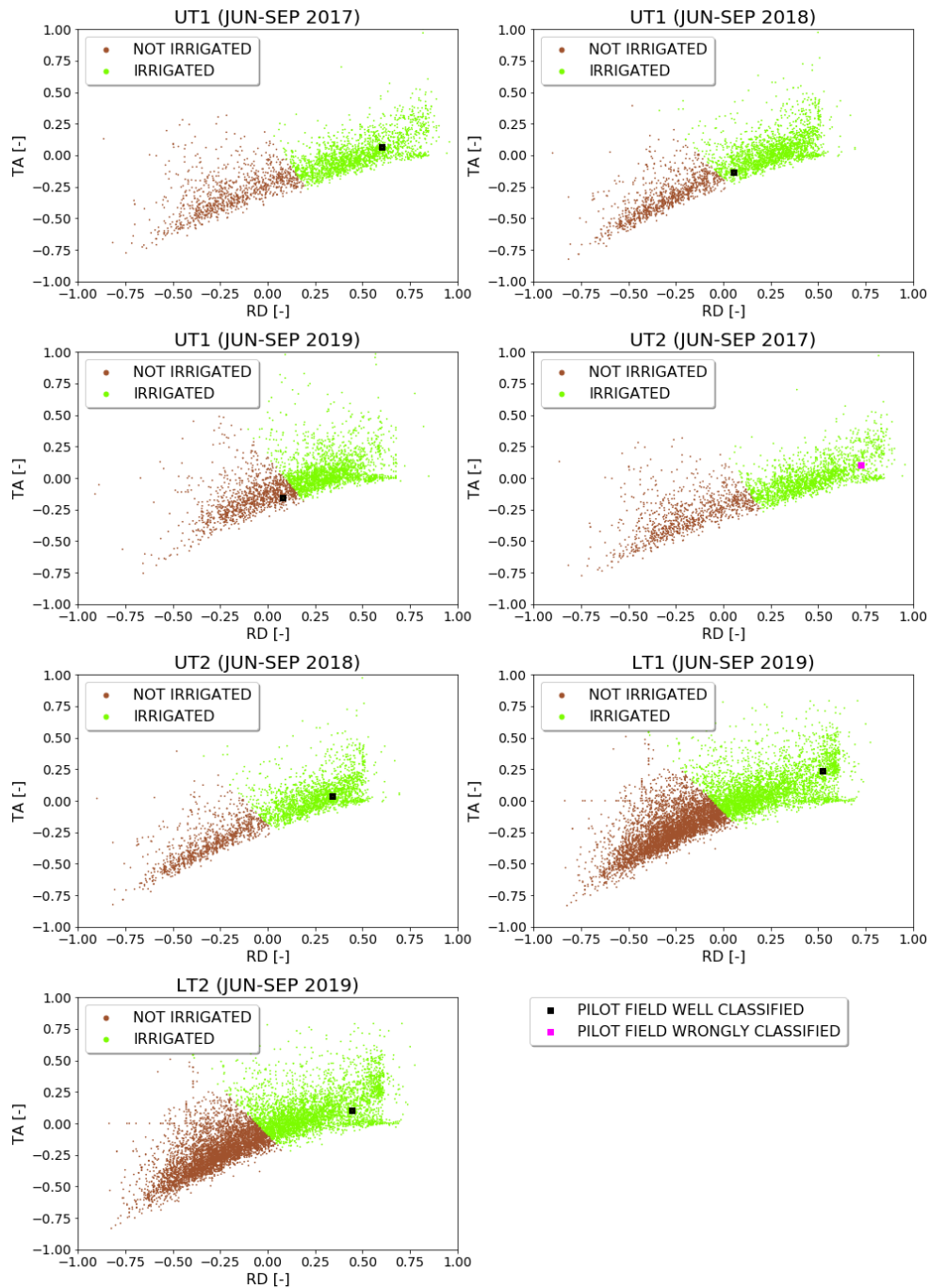
Figure 5.21. Input data points exploited in the clustering. The mean relative differences and the mean temporal anomalies calculated for the periods of interest are provided on the x-axis and on the y-axis, respectively. The cluster of the 100 m resolution pixel classified as irrigated is represented in green, while the cluster grouping the non-irrigated 100 m resolution pixel is represented in brown. The data points referred to the pilot fields are indicated with a square whose colour is black (magenta) if the irrigation occurrence is correctly (wrongly) reproduced by the proposed method (Dari et al., 2021b).

116

The actually irrigation/non-irrigation occurrence of the UT1 field is well reproduced by the proposed methodology. Regarding the UT2 field, the K-means algorithm fails in 2017, when it wrongly classifies the not irrigated field as irrigated. The irrigation occurrence in 2018 is well reproduced, while in 2019 the soil moisture data is not available. The occurrence of irrigation over the LT1 and LT2 pilot fields is well reproduced by the proposed classification. Despite the limited dimension of the ground truth data set does not ensure the representativeness of the obtained results, it is noteworthy that, when both soil moisture and benchmark irrigation data are available, the proposed method fails only once.

In order to test the detectability of irrigation events occurring over the pilot agricultural sites, the trends of the THEIA Sentinel-1 surface soil moisture against with in-situ rainfall and irrigation measurements are evaluated. Figure 5.22 shows the time series of the THEIA Sentinel-1 soil moisture, ground-observed rainfall, and irrigation for the pilot points UT1 and UT2. The same kind of information is provided for the pilot fields LT1 and LT2 in Figure 5.23.
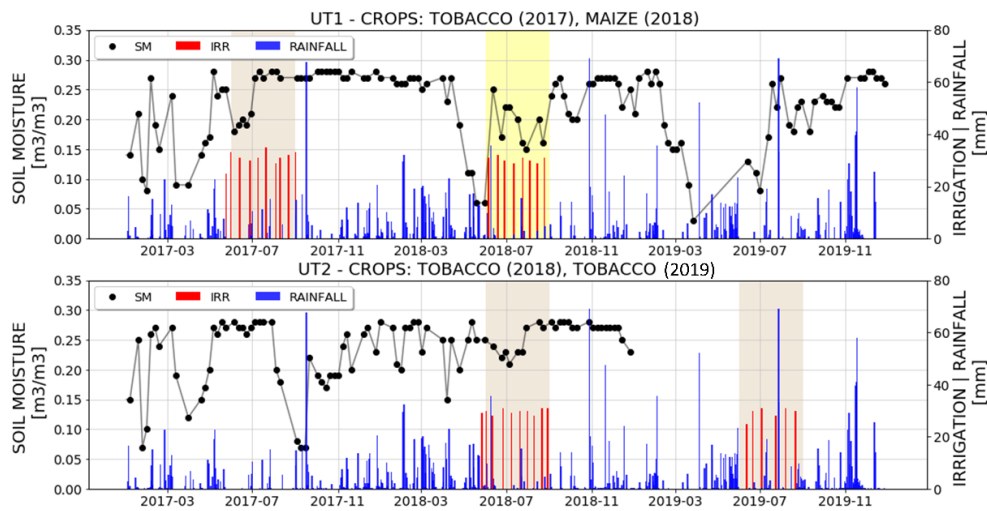
Figure 5.22. Time series of THEIA Sentinel-1 soil moisture, ground-observed rainfall, and irrigation over the pilot fields UT1 (upper panel) and UT2 (lower panel) in 2017-2019. The irrigation seasons are highlighted with different colours on the basis of the crop type.

117
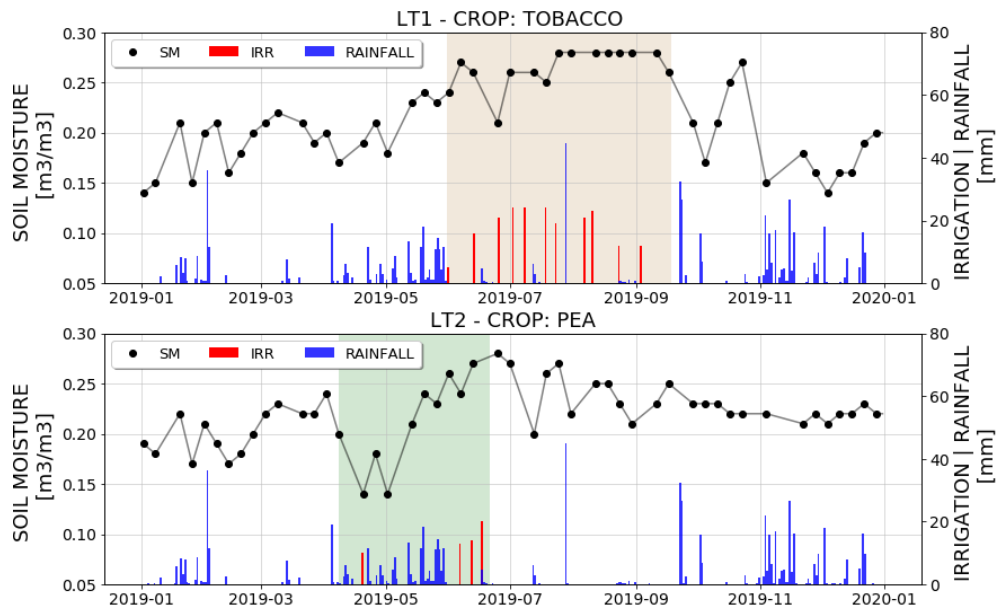
Figure 5.23. Time series of THEIA Sentinel-1 soil moisture, ground-observed rainfall, and irrigation over the pilot fields LT1 (upper panel) and LT2 (lower panel) in 2019. The irrigation seasons are highlighted with different colours on the basis of the crop type.

A common issue is found when Tobacco is cultivated (brown shaded area); in fact, the soil moisture increases up to the saturation condition during the irrigation season and then high values are kept until the end of October. An interesting result is obtained for the Maize in the UT1 plot during 2018 (yellow shaded area). In this case, the soil moisture time series seems to be more responsive to the irrigation amounts. Similarly, the brief irrigation season occurred in June 2019 over the LT2 field is reproduced by the THEIA Sentinel-1 data.

5.2.3 Discussion and Remarks

Interesting results emerge from the double-scale analysis carried out over the Upper Tiber basin. The main aim of this study is to test the applicability of the methodology developed for the case study in the Ebro basin over a more complex area, where irrigation practices are less evenly distributed and occur at a finer spatial scale. However, the detectability of irrigation at 1 km spatial resolution has been investigated; the only agricultural area where irrigation is evenly detected by all the remotely sensed soil moisture products, at least according to the spatial analysis, is the Upper Tiber area. Nevertheless, the clear district-scale signal is not corroborated by the temporal analysis. It is noteworthy that positive spatial relative differences over the Upper Tiber area detected for the modeled data set

also, thus suggesting that the results are partly influenced by static patterns, e.g., soil texture. In addition, as shown in Figure 5.14, the time series of the spatial relative differences referred to the Upper Tiber area show an increase during the irrigation season that is kept after the end of this period. This behaviour is reflected on the NDVI time series. This circumstance, along with the consideration that the most common crop over this area is tobacco, suggests that the height reached by these plants can likely have some effects on the retrieved soil moisture. It is noteworthy that, a similar issue is found in the plot-scale resolution soil moisture time series over the pilot fields where tobacco is cultivated. For this kind of crop, the harvesting begins before middle September. However, the process is not immediate, as first the leaves at the basis of the plant and then those above are gradually harvested. Hence, tobacco plants can be still present and affect the retrieved soil moisture even after September. The Sentinel-1 versions evaluated in the analysis at 1 km spatial resolution show potential in detecting scattered sub-portions of the pilot agricultural areas, where irrigation signal can be observed according to both spatial and temporal analyses. An overall good agreement between the patterns of spatial relative differences and temporal anomalies obtained through the Copernicus Sentinel-1 and the THEIA product aggregated at 1 km can be observed in Figures 5.15 and 5.17. The spatial extent of the irrigation practices over the agricultural areas in the Upper Tiber basin and the uneven distribution in space of the irrigated fields, together with the crop rotation, suggest to test the detectability of irrigation through plot-scale resolution products. The K-means clustering classification, exploiting the mean of the spatial relative differences and the mean of the temporal anomalies calculated through THEIA Sentinel-1 data as input, allows to produce high-resolution (100 m) binary maps of irrigated and not irrigated fields (see Figure 5.20). Unfortunately, the lack of information about irrigation practices on a consistent number of pilot fields represents a limitation. However, promising results are obtained by considering the few ground-truth data available. The high-resolution (100 m) maps of irrigated areas referred to the periods June-September 2017, 2018, and 2019, show higher rates of irrigated fields over the Upper Tiber area with respect to the other pilot districts; this is a comforting result, as the Upper Tiber is known to be the most evenly irrigated agricultural district. Furthermore, the validation carried out through the few information available shows a good agreement between the proposed maps and the actual irrigation occurrence. In fact, where both ground-truth and soil moisture data are available, the algorithm well classifies the

irrigated/non-irrigated fields six times out of seven. The perspective of obtaining soon a larger ground-truth data set will make a more comprehensive and thus robust validation possible. The THEIA Sentinel-1 data shows potential in detecting irrigation events. Nevertheless, the well-developed vegetation conditions can be responsible of disturbances affecting the retrieved soil moisture conditions (El Hajj et al., 2017; Le Page et al., 2020). Finally, another potential limitation of the plot-scale THEIA Sentinel-1 data is the temporal frequency (6 days), which can represent an issue in reproducing irrigation events occurring with a certain temporal distance from the SAR acquisition (Bousbih et al., 2018; Bazzi et al., 2019; Le Page et al., 2020).

The above discussed results lead to the following final remarks:

1. The analysis at 1 km resolution reveals some potential in detecting the uniform irrigation pattern existing in the Upper Tiber area. This result, obtained for all the considered products, is more evident for the spatial analysis with respect to the temporal one; hence, an influence due to static patterns (e.g., soil texture) is expected and needs to be further investigated;

2. The Copernicus Sentinel-1 and the THEIA Sentinel-1 aggregated at 1 km show potential in detecting scattered irrigation in accordance to both spatial and temporal analyses;

3. The proposed maps of irrigated areas at a plot scale resolution (100 m) show promising results in reproducing the spatial distribution of irrigated fields by exploiting remotely sensed soil moisture only. The limited ground truth information available show good accordance with the clustering-derived maps, but a larger data set on the actual occurrence of irrigation is needed in order to perform a more comprehensive and thus reliable validation.

4. Plot-scale THEIA Sentinel-1 data is able to reproduce the soil moisture dynamics on the single agricultural field and thus to detect irrigation events. Nevertheless, limitations due to the influence of vegetation and to the low temporal frequency are pointed out.

Chapter 6

Results of the Irrigation Quantification Activity

In this chapter, the results of the irrigation quantification activity are provided. As explained in Chapter 4, the methodology developed to estimate irrigation water amounts from remotely sensed soil moisture has been applied in the pilot area in the Ebro basin only; the experiment exploiting SMAP at 1 km data (henceforth SMAP experiment) is described in Section 6.1, while in Section 6.2 the results of the experiment exploiting SMOS at 1 km data (henceforth SMOS experiment) are presented.

6.1 SMAP Experiment

In the SMAP experiment the amounts of irrigation water applied to the pilot districts during the period January 2016 – September 2017 have been estimated and compared with benchmark irrigation volumes. An analysis aiming to assess the sensitivity of the results to the model's parameters has been also performed. The SM2RAIN algorithm has been calibrated over the dryland at East of the Urgell district during the whole period considered for the irrigation estimates. The median values of the distributions of the parameters Z^*, a, and b (see Section 4.6.1.1) resulting from the calibration have been used as fixed values for each pixel of the irrigated domain during the irrigation estimates step; for this experiment these values are: $Z^* = 32.930$ mm, $a = 0.882$ mm and $b = 7.704$. The time series of the estimated irrigation amounts spatially averaged over each district, together with the associated benchmark amounts and with spatially averaged rainfall from the SAFRAN data set are provided in Figure 6.1. Note that the time series referred to Urgell, Algerri Balaguer, and North and South Catalan and Aragonese are 5-days aggregated, while the results for the Pinyana disctict are monthly aggregated, in order to directly compare them with the benchmark amounts, available at a

monthly temporal resolution. In addition, for the Pinyana district the results are represented through bars.
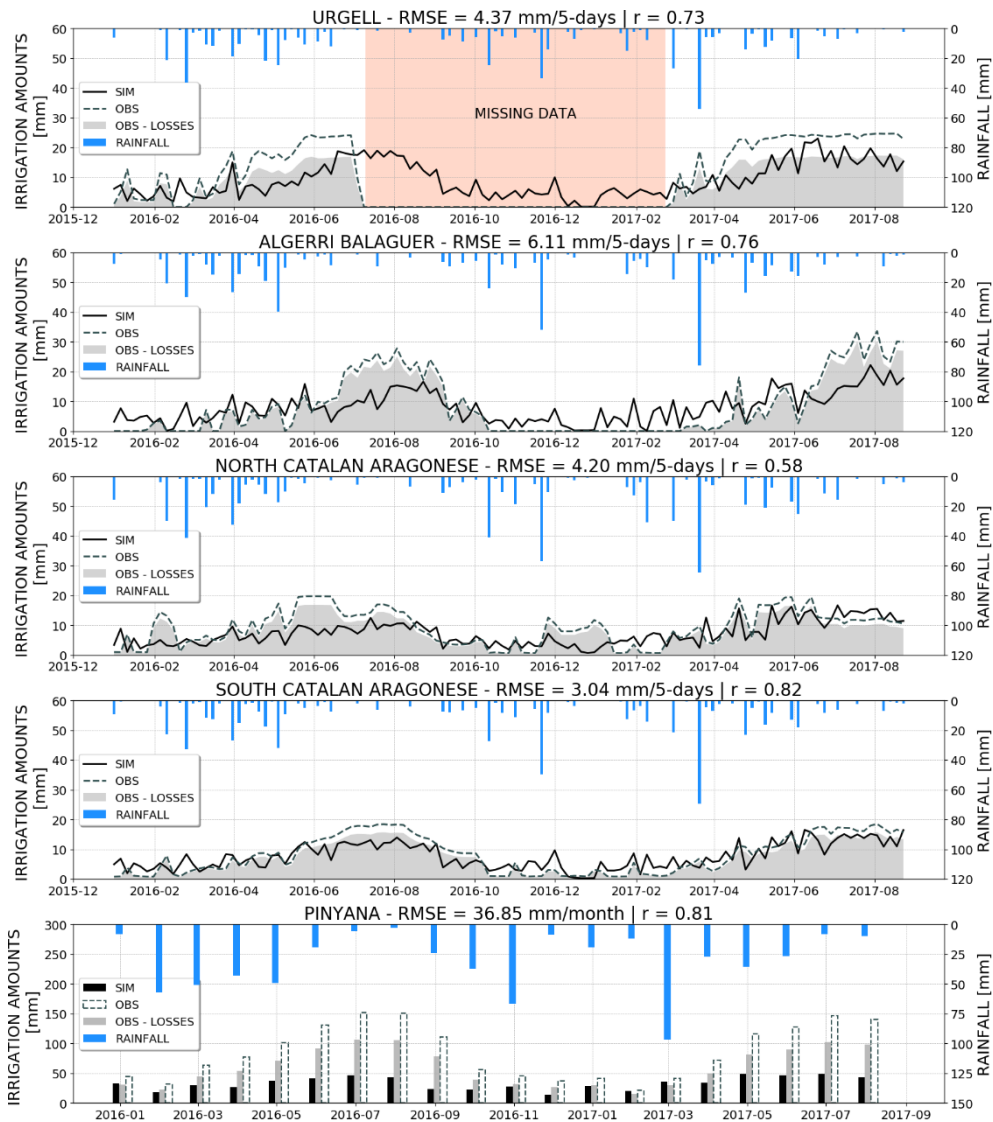
Figure 6.1. Time series of spatially averaged estimated irrigation amounts (black line), gross benchmark irrigation (dark grey dashed line), benchmark irrigation with losses taken into account (light grey shaded area), and spatially averaged rainfall from SAFRAN (light blue bars). For all the districts except Pinyana, the data are 5-days aggregated, while for the Pinyana district the data are monthly aggregated and represented through bars with the same colours code adopted for the other districts (Dari et al., 2020).

The Pearson correlation coefficient (r) and the RMSE are used to evaluate the performances of the proposed method in reproducing the actually occurred irrigation. The scores are calculated by considering the aggregated irrigation water amounts and the benchmark values reduced according to the losses due to

irrigation efficiency. A good agreement (RMSE = 4.37 mm/5-days and r = 0.73) between estimated and benchmark irrigation can be observed over the Urgell district; unfortunately, the analysis over this district is limited because of the missing data in the benchmark irrigation volumes. Over the Algerri Balaguer district, a similar r, equal to 0.76, associated with a RMSE equal to 6.11 mm/5-days is obtained. In this case, false estimated irrigation during the winter season and underestimates during the peaks of the highest-intensity irrigation season (from July to September) are observed. The lowest r value (0.58) is obtained for the North Catalan and Aragonese district; conversely, for this area the RMSE is satisfactory (4.20 mm/5-days). The South Catalan and Aragonese is the district where the best overall performances are observed; the RMSE results equal to 3.04 mm/5-days, while r is equal to 0.82. Over the Pinyana district, although if good agreement between monthly aggregated trends of estimated and benchmark irrigation amounts (r = 0.81) is found, not-negligible underestimates are obtained (RMSE = 36.85 mm/month). It is noteworthy that, even if the RMSE values obtained over the Algerri Balaguer and the Pinyana district are comparable, they can be attributed to different issues; in fact, the error over the Algerri Balaguer is determined by false irrigation during winter and underestimates during the highest irrigation intensities periods, while the error over the Pinyana district is due to systematic underestimates produced by the method.

Figure 6.2 shows, for each district, the aggregated magnitudes of estimated irrigation amounts against the cumulated benchmark values during 2016 and the considered portion of 2017. The estimated irrigation amounts are represented through black bars, the benchmark values reduced according to the losses due to the efficiency of the particular irrigation system are represented through light grey bars, while the bars with dashed edges represent the gross benchmark amounts. The colours of the circles above the bars of each district express the magnitude of the difference between the estimated and the reference long-term magnitudes; red indicates an underestimate, while an overestimate is represented in blue. It appears clear how, for four of the five pilot districts, the cumulated values of the actually occurred irrigation amounts are well reproduced by the proposed methodology. The only exception is the Pinyana district, where not-negligible underestimates are obtained (-337.57 mm in 2016 and -186.75 mm in January-September 2017). Good performances are obtained over the Urgell district (even if an overestimate equal to +80 mm in 2016 is obtained), the Algerri Balaguer district, and the South Catalan and Aragonese district. Over the North Catalan and

Aragonese area the proposed method produces an underestimate of -116.97 mm with respect to the actually occurred irrigation in 2016, while a good agreement is obtained during the periof January-September 2017.
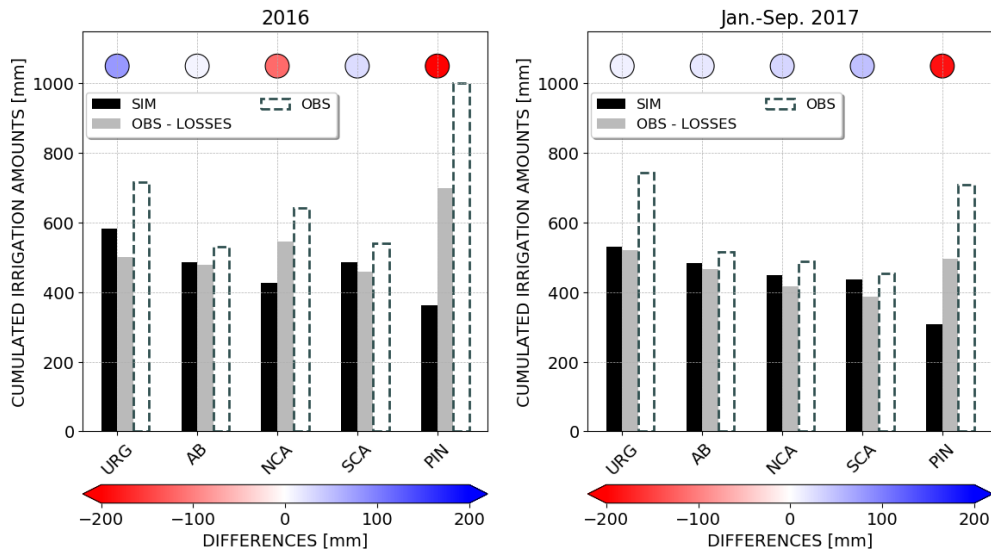
Figure 6.2. Estimated and observed cumulated irrigation amounts during 2016 (on the left) and January-September 2017 (on the right) over the pilot districts: Urgell (URG), Algerri Balaguer (AB), North Catalan and Aragonese (NCA), South Catalan and Aragonese (SCA), and Pinyana (PIN). The black bars represent the estimated irrigation amounts, the light grey bars are referred to the benchmark values reduced by considering the losses due to irrigation efficiency, and the bars with dashed edges represent the gross benchmark values. The colours of the circles above the bars indicate the differences between the estimated and the benchmark amounts (Dari et al., 2020).

Figure 6.3 shows the spatial distribution of the SM2RAIN-derived irrigation estimates cumulated during the whole 2016 and January-September 2017. Some irrigation-related patterns, for instance those in the central and upper parts of the Urgell or at the West side of Algerri Balaguer, are recursive in both maps. It is noteworthy that, the same patterns can be observed in the maps of irrigated areas proposed in this research (see Figure 5.12). In general, over the Urgell, where inundation irrigation is the most widespread technique, evenly distributed high rates of cumulated irrigation amounts can be detected. The intense irrigation-related pattern in the Algerri Balaguer district is less evident going to the East side, which actually is not irrigated; in fact, a protected area destined to bird reserve is located at East of the Algerri Balaguer. Recursive areas of high long-term magnitudes of estimated irrigation can be spotted in both Northern and Southern partitions of the Catalan and Aragonese district. Finally, evenly distributed low

rates of cumulated SM2RAIN-derived irrigation amounts can be observed over the Pinyana district, corroborating the previous results showing poor performances of the proposed method in retrieving the amounts of water applied for irrigation over this district.
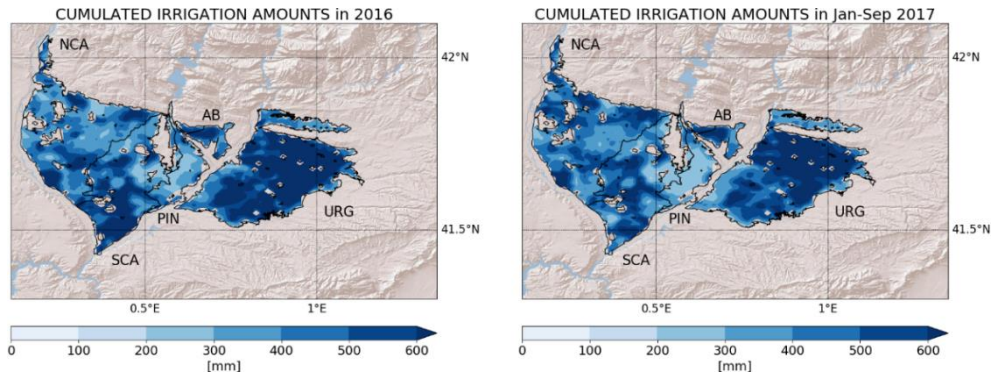
Figure 6.3. Maps of the estimated irrigation water amounts cumulated for the whole 2016 (left side) and for the period January-September 2017 (right side) over the pilot districts: URG stands for Urgell, AB for Algerri Balaguer, NCA for North Catalan and Aragonese, SCA for South Catalan and Aragonese, and PIN for Pinyana (Dari et al., 2020).

In the SMAP experiment, a complementary analysis aimed to assess which SM2RAIN term contributes the most in determining the total amount of water entering into the soil has been performed. Figure 6.4 provides, for each district, the spatially averaged contribution of each SM2RAIN's term to the model's output (irrigation rates plus rainfall rates). The drainage contribution is represented through the red shaded area, the soil moisture variation through the blue shaded area, and the actual evapotranspiration term through the green shaded area. The final model output is represented through the black line. SAFRAN-derived rainfall rates (blue bars) and estimated irrigation rates (magenta bars), both averaged over each related district, are also shown. In each plot of Figure 6.4, a pie chart is also provided; it expresses the percentage of each term's contribution to the total, computed when soil moisture variations are higher than zero. In fact, while the $g(t)$ and $e(t)$ terms represent fluxes and thus assume values greater than or equal to zero, the $nZdS(t)/dt$ term represents a change in a stock and can assume both positive or negative values. During periods in which neither rainfall or irrigation events occur, the surface soil moisture assumes a decreasing trend following a drying law. Under these conditions, the contribution of soil moisture variations is negative and it equilibrates the contributions of actual evapotranspiration and drainage that keep on being positive. Hence, a negative soil moisture variation is necessary to balance consumptions of the available water content in the control

volume of soil, thus solving the balance. This is the main reason why the percentages of each contribution to the total shown in the pie charts has been calculated for periods when the $nZdS(t)/dt$ term is positive only, i.e., after rainfall or irrigation events. It is noteworthy that soil moisture also plays an indirect role consisting in modulating the potential evapotranspiration over the bare soil.
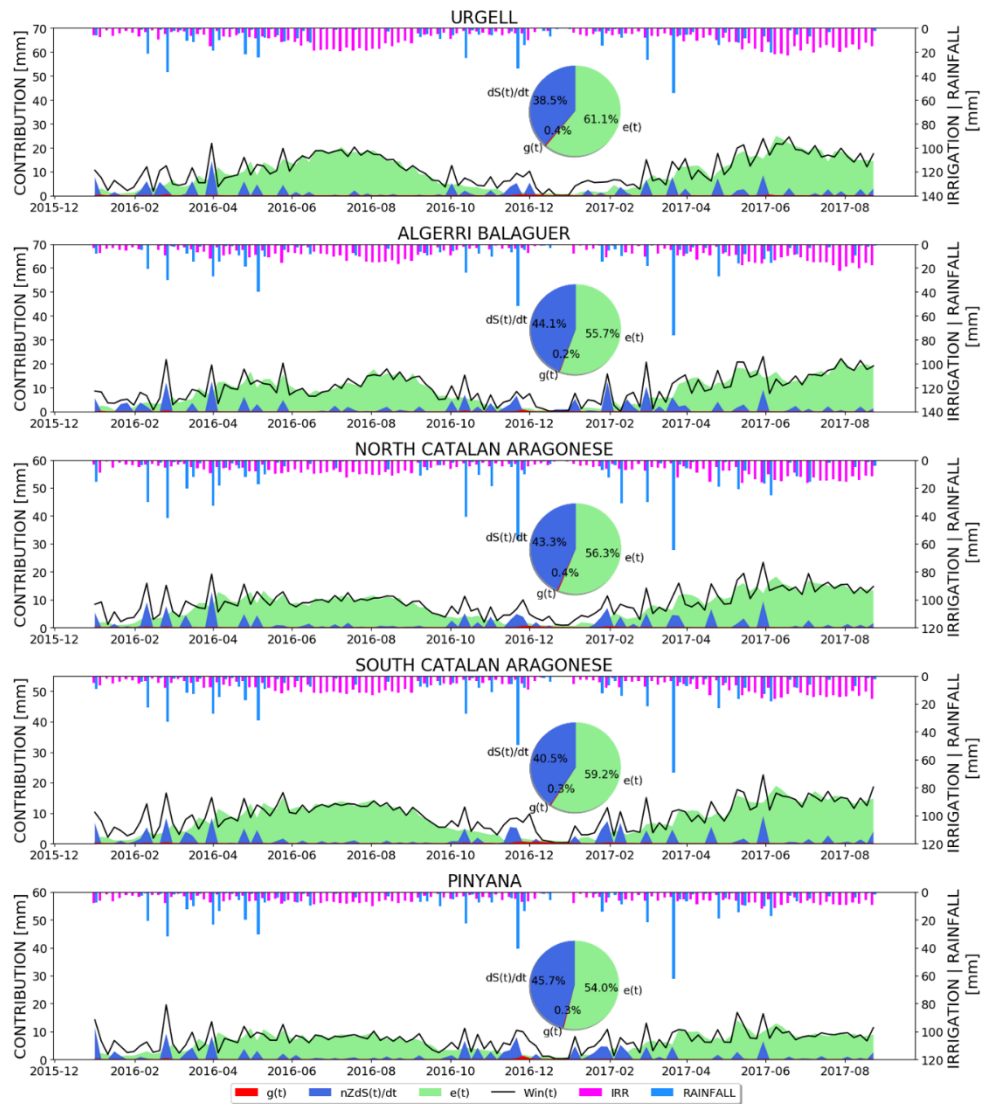
Figure 6.4. 5-days aggregated time series of the contributions of the drainage, $g(t)$, of the soil moisture variation, $nZdS(t)/dt$, and of the actual evapotranspiration, $e(t)$, to the total SM2RAIN-derived amount of water entering into the soil, $W_{in}(t)$. SAFRAN-derived rainfall rates and the estimated irrigation rates are also shown (bar charts). All the data are spatially averaged over the related districts. The pie charts show the percentages of each contribution to the total, calculated when the soil moisture variation is positive (Dari et al., 2020).

Hence, the pie charts of Figure 6.4 only show the direct contribution of soil moisture variations to the total, as their indirect role is difficult to be quantitatively estimated. For all the pilot districts, the drainage rate brings a negligible contribution to the total, ranging between 0.2% and 0.4% of the total. Similar results were recently obtained by Jalilvand et al. (2019), in which coarser resolution soil moisture products were used. The direct contribution of soil moisture variations ranges between 38.5% and 45.7% of the total. The actual evapotranspiration term is the predominant one for all the pilot irrigation districts; the percentages associated to it vary between 54.0% and 61.1% of the total.

The results of the assessment of the uncertainty due to the parameters Z^*, a, and b are shown in Figure 6.5, in which the 10-days aggregated values of the district-averaged estimated irrigation amounts obtained through the main simulation previously described are represented through the black line. The additional simulations obtained by randomly considering the 25th, 50th, and 75th percentiles of the three parameters' distributions are represented in light grey and constitute a confidence interval on which this analysis is based.
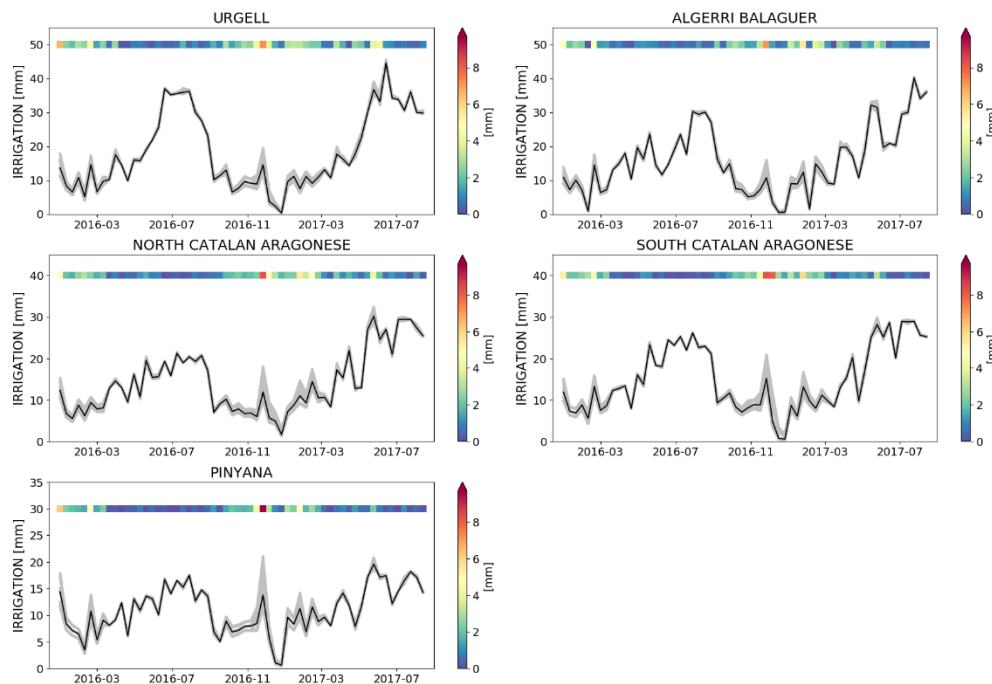
Figure 6.5. 10-days aggregated time series of the districts-averaged estimated irrigation with the related confidence interval, expressing the uncertainty due to the Z^*, a, and b parameters and whose amplitude is expressed through the upper horizontal bar (Dari et al., 2020).

The amplitude of the interval in time is expressed by the horizontal bar above each plot. For all the pilot districts, the amplitude of the confidence interval is small (lower than 2-3 mm/10-days) during the highest-intensity irrigation periods in 2016 and 2017. Outside the May-September time window, the amplitude of the confidence interval rises, reaching the maximum values at the end of 2016. The overall maximum amplitudes detectable range between 7.1 mm/10-days (for the Algerri Balaguer district) and 9.7 mm/10-days (for the Pinyana district).

The sensitivity to the p parameter has been evaluated separately from the other parameters and according to another procedure, whose results are shown in Figure 6.6. The 10-days aggregated spatial averages of the estimated irrigation amounts over each district through the main simulation are represented with the black line, while the additional simulations obtained by keeping Z^*, a, and b fixed to the median values of their distributions determined during the calibration step and by increasing the p value from 0.3 to 0.6 with steps of 0.01 are represented in light grey.
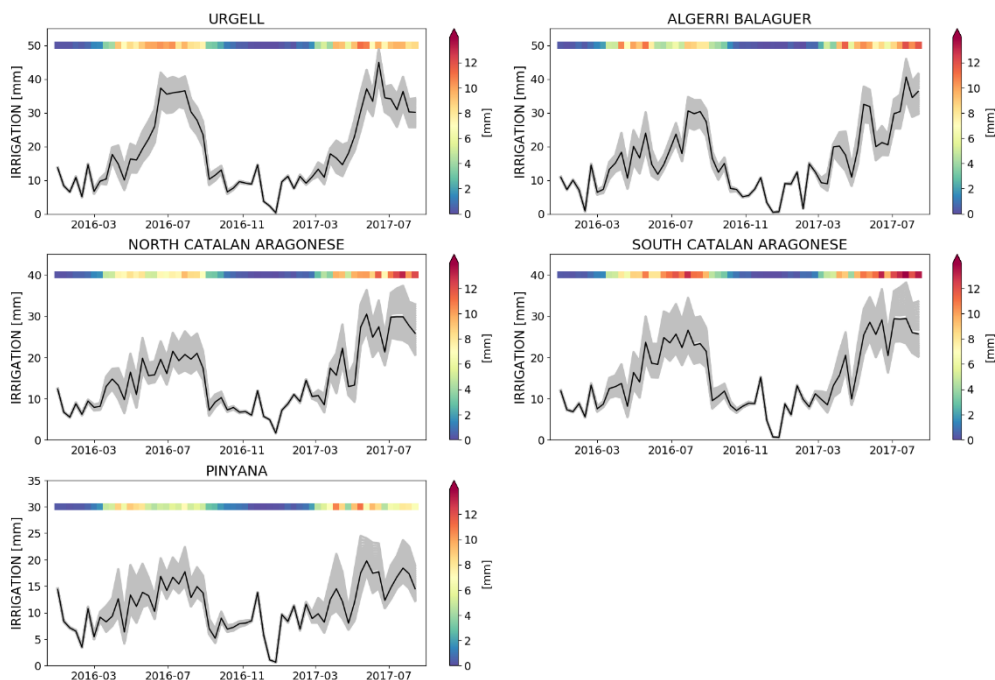
Figure 6.6. 10-days aggregated time series of the districts-averaged retrieved irrigation with the related confidence interval, expressing the uncertainty due to the p parameter and whose amplitude is expressed through the upper horizontal bar (Dari et al., 2020).

Conversely from what happens for the parameters Z^*, a, and b, the uncertainty due to the p parameter is higher when irrigation mainly occurs, i.e., from May to

September; this is an expected result, as this parameter regulates the stress conditions in the modeling of the crop evapotranspiration. The widest amplitudes of the confidence interval referred to the uncertainty to the p parameter are detected during the highest-intensity irrigation season in 2017 and vary between 11.1 mm/10-days (for the Pinyana district) and 14.7 mm/10-days (for the South Catalan and Aragonese district).

6.2 SMOS Experiment

The SMOS experiment, carried out by adopting the same model configuration as the SMAP experiment and covering the period from January 2011 to September 2017 has a dual target, namely to compare the performances of the two high-resolution (1 km) soil moisture data sets during the overlapping period (January 2016 – September 2017) and to extend the irrigation estimates back to 2011. The calibration phase, performed through an objective function aimed to minimize the root mean square difference between the retrieved rainfall over the dryland at East of the Urgell and the SAFRAN-derived rainfall, provides the following values for the Z^*, a, and b parameters: $Z^* = 22.896$ mm, $a = 13.770$ mm and $b = 3.864$.

The long-term magnitudes of the estimated irrigation amounts in the SMOS experiment are shown in Figure 6.7. For each district, the cumulated SMOS-derived irrigation amounts are represented through orange bars, the cumulated benchmark values reduced by considering the losses associated to the system of the irrigation system are shown with light grey bars, and the cumulated gross benchmark values are represented through bars with dashed edges. In order to facilitate the comparison between the two irrigation estimates experiments carried out, the cumulated SMAP-derived irrigation amounts are also shown (black bars). The circles above the bars assume different colours on the basis of the magnitudes of the differences between the irrigation amounts estimated through the SMOS experiment and the net benchmark volumes, with underestimates indicated in red and overestimates in blue.
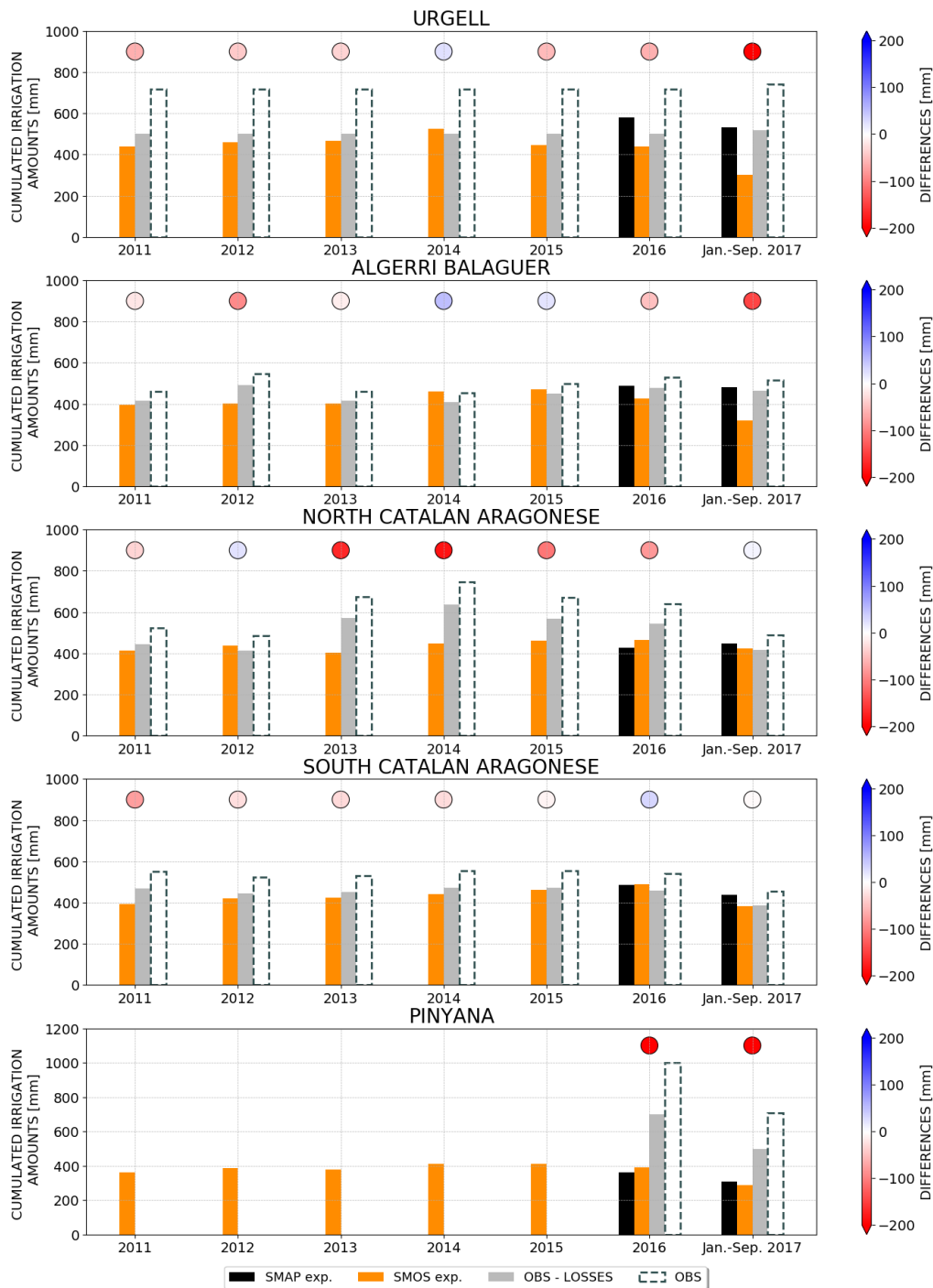
Figure 6.7. Cumulated irrigation amounts estimated through the experiment with SMOS at 1 km data set (orange bars) and through experiment exploiting SMAP at 1 km data set (black bars) against benchmark values reduced by considering the losses due to irrigation efficiency (light grey bars) and gross benchmark values (bars with dashed edges). The colours of the circles indicate the differences between the SMOS-derived estimates and the benchmark amounts (Dari et al., 2020).

130

Over the Urgell district and the Algerri Balaguer district, the SMOS-derived irrigation estimates are slightly lower than the SMAP-derived ones. This issue is attributable to the RFI problems affecting soil moisture data retrieved by SMOS over these areas since mid-2016 already discussed in the previous chapter of this thesis. For both partitions of the Catalan and Aragonese district, as well as for the Pinyana district, the SMOS-derived irrigation estimates are comparable to those retrieved in the SMAP experiment; over the Northern and Southern partitions of the Catalan and Aragonese district the SMOS experiment provides even higher performances with respect to the SMAP experiment. By looking at the performances of the SMOS experiment only in reproducing the actually occurred irrigation over the pilot districts, estimates consistent with net benchmark amounts are overall obtained. Unfortunately, it has not been possible to obtain benchmark irrigation amounts for the Pinyana district; hence, the performances of the SMOS experiment cannot be clearly determined over this area. Nevertheless, the similitudes with the SMAP-derived estimates suggest that the actually occurred irrigation over this district is confirmed to be not adequately estimated through the proposed approach. Good accordance between the cumulated SMOS-derived estimates and the cumulated net benchmark values are observed over the Urgell and the Algerri Balaguer districts until 2016, when the abovementioned RFI issues start affecting the SMOS-retrieved soil moisture. Not-negligible underestimates (up to -185.93 mm) are detected over the Northern partition of the Catalan and Aragonese district during the period 2013-2015. Finally, the water actually applied for irrigation over the Southern partition of the Catalan and Aragonese district results well reproduced by the irrigation estimates produced through the SMOS experiment.

As a result of the merging of the two irrigation-estimate experiments carried out, a data set of almost 7 years (from January 2011 to September 2017) of estimated irrigation amounts has been obtained. The first five years of the data set are derived from the SMOS experiment, while the remaining period is covered by the SMAP experiment. The spatial distribution of the cumulated SMOS-derived irrigation amounts during the period 2011-2015 are provided in Figure 6.8. It is noteworthy that during this time span SMOS data is not affected by RFI problems. In fact, patterns of high cumulated irrigation amounts over the Urgell and the Algerri Balaguer can be observed. In particular, recursive evenly distributed high irrigation amounts are observed in the Upper part of the Urgell. This pattern has been found in the SMAP experiment also during the remaining years (see Figure

6.3). Both Southern and Northern partitions of the Catalan and Aragonese district show similar long-term magnitudes patterns of estimated irrigation. As an example, the central portion of the South Cataland and Aragonese district, where a non-irrigated area destined to vineyard exist, is well reproduced through negligible cumulated irrigation amounts. It is noteworthy that, the same area is well reproduced by the SMAP experiment during 2016 and the considered portion of 2017 also, thus consolidating the reliability of the merged data set. According to the SMOS experiment also, Pinyana is the district showing the lowest cumulated irrigation values.
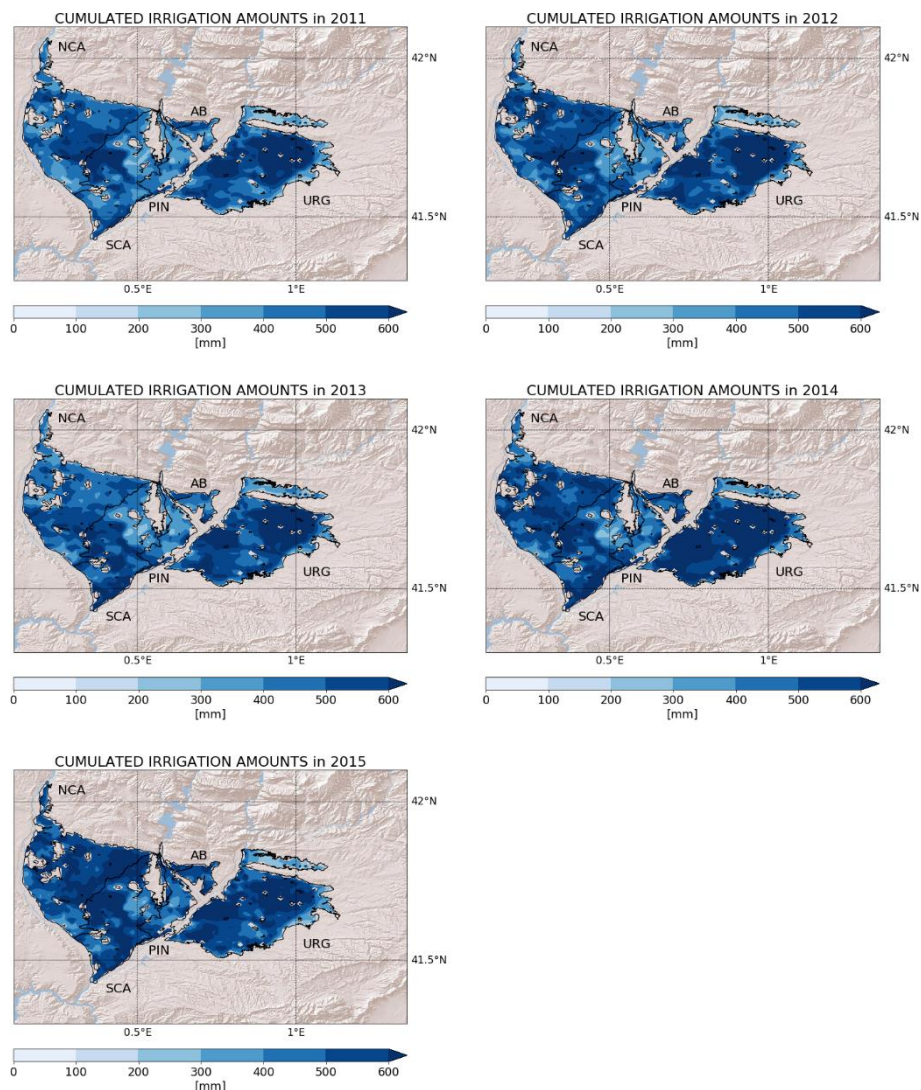
Figure 6.8. Maps of the estimated irrigation water amounts cumulated for each year in the period 2011-2015 over the pilot districts: Urgell (URG), Algerri Balaguer (AB), North Catalan and Aragonese (NCA), South Catalan and Aragonese (SCA), Pinyana (PIN).

Although the analysis carried out by using DISPATCH downscaled SMOS data is less detailed than the one performed with DISPATCH downscaled SMAP data, it shows the suitability of SMOS soil moisture at 1 km also to be used to retrieve the amounts of water actually applied for irrigation through the proposed methodology.

6.3 Discussion and Remarks

In this research, a methodology to retrieve water amounts actually applied for irrigation practices by exploiting high-resolution (1 km) soil moisture products is proposed. The pilot area in the Ebro basin, rich in terms of irrigation-related information, has proven to be particularly suitable to assess the robustness of the approach. Furthermore, this analysis fills the gap between the potential of coarse resolution soil moisture data to detect irrigation signals shown in previous studies (Brocca et al., 2018; Zaussinger et al., 2019) and the need for high-resolution products to adequately capture small-scale irrigation practices.

In the SMAP experiment satisfactory results have been obtained for four of the five pilot districts. Over the areas where the method is capable to retrieve the actually occurred irrigation amounts, both long-term magnitudes and irrigation timing are well reproduced. The correlation calculated between the estimated irrigation amounts and the net irrigation benchmark volumes between 0.58 (observed for the Northern partition of the Catalan and Aragonese district) and 0.82 (referred to the Southern partition of the Catalan and Aragonese district). The RMSE between estimated and reference irrigation amounts ranges between 3.04 mm/5-days (found for the Southern partition of the Catalan and Aragonese district) and 6.11 mm/5-days (observed for the Algerri Balaguer district). It is noteworthy that, according to both metrics, the Southern portion of the Catalan and Aragonese district is where the overall best performances are obtained. During the winter season in 2016, irrigation events not reflected in the benchmark data can be observed for the Algerri Balaguer. These events may be explained as false irrigation produced by SM2RAIN or as actually occurred irrigation with a certain delay with respect to the time when the water has been pumped from the river feeding the irrigation canal. The Algerri Balaguer system is equipped with three reservoirs to stock water to be delivered to the crops later than the withdrawn from the river. The presence of the reservoirs and their use can also explain the underestimates obtained during summer over the Algerri Balaguer. In this

research, the water pumped to the district has been taken as instant reference real irrigation, but probably only part of this water amount is immediately delivered to the crops and another part is stored into the reservoirs in order to be delivered later. It is noteworthy that an eventual delay between the withdrawn of water from the river and the supply of this water to the irrigated fields may negatively affect the RMSE and r values found over the district.

Despite Algerri Balaguer being the district where this issue is more evident, as winter irrigation is not apparently reflected by the benchmark values, amounts of estimated irrigation between the end of 2016 and the beginning of 2017 are observed over all the districts. For instance, an interesting result is represented by not negligible irrigation events occurred in winter 2016 over the North Catalan and Aragonese district and reproduced by the proposed method. In general, the winter irrigation events can be false irrigation alarms occurring when the total amount of water entering into the soil is not equilibrated by the rainfall removal. An issue explaining the false irrigation events during winter may be the missing precipitation in the SAFRAN data set. In fact, if the data set does not properly capture an event, an underestimate in the rainfall removal phase occurs, thus overestimating irrigation. It is noteworthy that SAFRAN has proven to be accurate over the study area (Quintana-Seguí et al., 2017), but its spatial resolution (5 km) may represent an issue for the proposed application, in which a spatial resolution of 1 km is adopted. However, the inclusion of a major number of precipitation stations from the SAIH system into SAFRAN is foreseen.

Several complementary causes can explain the unsatisfactory performances obtained over the Pinyanan district. Mainly, a "contamination" due to an adjacent not irrigated area and large uncertainties associated to the benchmark irrigation amounts and to the associated losses. The Pinyana irrigation canal, as well its irrigation system, is the most ancient one of the pilot area. Not all the water delivered through this canal is used for irrigation practices, but the withdrawal for other purposes are actually negligible. The main issue is probably the scarce distribution efficiency. The Pinyana canal is an old free surface one, hence, the associated losses may be higher than assumed.

Despite the evapotranspiration term has proven to be not essential in SM2RAIN applications aimed to retrieve rainfall (Brocca et al., 2015), the SMAP experiment points out the importance of a correct modeling of this process to estimate irrigation over semi-arid areas. The same result can be found in Jalilvand et al.

(2019). In this study, the evapotranspiration term plays the leading role in determining the SM2RAIN output, followed by the direct contribution of soil moisture variations. Soil moisture plays a much complex role in the soil water balance. In fact, according to the proposed water-limited approach, the soil moisture affects the evapotranspiration estimate also, as it modulates the potential one over the bare soil portion of irrigated pixels. This effect is clearly visible in Figure 6.9, where several variables referred to a control point located in the Urgell district are shown; in particular, the upper panel shows the occurrence of periods characterized by irrigation estimates (blue line) lower than the potential evapotranspiration rates (red line) in presence of low soil moisture values (light blue line in the lower panel). Furthermore, soil moisture is also involved in the regulation of the occurrence of stress conditions.

The analysis aimed to assess the uncertainties associated to the SM2RAIN's parameters highlights that the retrieved irrigation estimates are scarcely affected by the parameters Z^*, a, and b. In fact, the amplitude of the confidence interval associated to these parameters reaches the minimum values during the highest-intensity irrigation periods, while the maximum amplitudes are reached at the end of 2016. Conversely, the amplitudes of the confidence interval referred to the uncertainty linked to the p parameter reach the maximum values when irrigation mainly occurs. This is expected since the p parameter is involved in the crop evapotranspiration process. In the FAO model, stress is taken into account by computing the fraction of water available for crops. This amount of water is the root zone soil moisture and it is derived from tables where reference values for each crop are provided. For many crops, a fraction equal to 0.5 is recommended. In the parametrization proposed in this research, the occurrence of stress conditions is determined through a surface soil moisture threshold. Hence, not the whole soil water profile is take into account. Furthermore, the threshold adopted for the beginning of the stress conditions is static both in space and time. For this reason, the build of a dynamic modeling for p, in which the parameter can vary for each crop type and in time, is among the future developments of the proposed approach.
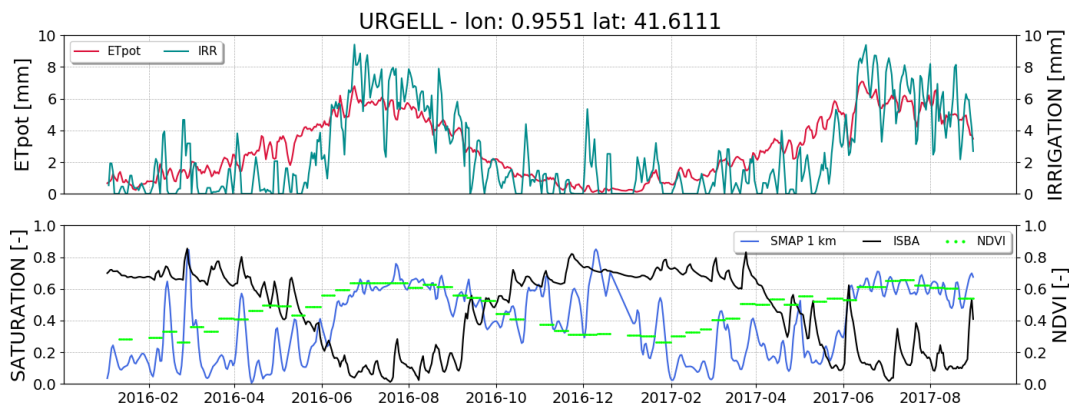
Figure 6.9. Time series of several variables referred to a control point in the Urgell district. Upper panel: estimated irrigation (blue line) and potential evapotranspiration (red line). Lower panel: soil moisture from SMAP at 1 km data set (light blue line), soil moisture from ISBA (black line), and NDVI (green dots).

The SMOS experiment shows the reliability of the SMOS at 1 km data set also in retrieving the amounts of water applied for irrigation. Except for the areas where the already discussed RFI problems affect the result, the SMOS-derived estimates result close to the SMAP-derived ones. Over the Catalan and Aragonese district, the SMOS experiment even reaches better performances than the SMAP experiment in reproducing the actually occurred irrigation. A good agreement between the SMOS-derived estimates and the benchmark amounts is generally obtained also for the period 2011-2015.

On the basis of the above discussed results, the following remarks can be drawn:

1. The proposed methodology is capable to quantitatively estimate the actually occurred irrigation events over four of the five pilot districts;

2. where the method performs well, not only the long-term cumulated irrigation amounts, but their timing and spatial distribution also are well reproduced;

3. the evapotranspiration term cannot be neglected in SM2RAIN applications aimed to estimate irrigation over semi-arid regions. In fact, this process plays the leading role in determining the total amount of water entering into the soil, even more than the direct contribution of soil moisture, which also plays indirect roles difficult to be quantitatively assessed;

4. the retrieved irrigation estimates are less sensitive to the SM2RAIN's parameters Z^*, a, and b during the highest-intensity irrigation periods.

Conversely, the uncertainties due to the p parameter are higher when irrigation mainly occurs;

5. the comparable performances of the DISPATCH downscaled SMOS and SMAP data sets allow to build a reliable data set of estimated irrigation covering a time span of almost seven years, from January 2011 to September 2017.

Chapter 7

Future Perspectives

In this chapter, the future developments foreseen for this research are presented. They mainly regard further improvements in the irrigation detection and quantification tasks, described in Section 7.1, and the inclusion of irrigation into SURFEX simulations, described in Section 7.2. Finally, the IRRIGATION+ project is presented in Section 7.3.

7.1 Detecting and Quantifying Irrigation

As explained in Chapter 5, the collection of more ground truth irrigation data over the pilot agricultural areas in the Upper Tiber basin represents a future development to be addressed in order to perform a robust validation of the clustering-derived maps of irrigated areas at a plot scale. However, benchmark irrigation volumes at a plot scale are desirable for the pilot area in the Ebro basin also. The results obtained by the analysis on the irrigation detectability carried out over the two pilot areas, which are thoroughly different from each other, provide insights on the crucial role played by the spatial resolution of the remote sensing data; in fact, irrigation is practiced worldwide over domains whose extension is widely varying because of several factors, e.g., the topography. The link between the extension of the irrigated areas and the required resolution of soil moisture data for irrigation detection and mapping purposes highlighted by the presented results is useful under the perspective of an extension to larger scales of the proposed methodologies. In fact, the use of temporal stability derived indices to identify where irrigation occurs is expected to be easily applied over larger domains (i.e., at the Country scale). Further investigations on the possibility to retrieve the amounts of water actually applied for irrigation are surely among the future perspectives of the presented research. This task can be declined according to several activities, namely the application of the proposed methodology to estimate irrigation quantities over the Upper Tiber basin also, the exploration of alternative methods to retrieve the irrigation water amounts, and modifications to

the proposed SM2RAIN configuration. Concerning the application of the presented methodology over the pilot agricultural areas in the Upper Tiber basin, some clarifications need to be done. As discussed in Chapter 5, the complexity in terms of topography and the spatial extent of the irrigation events over this area make the adoption of soil moisture products at very high resolution necessary. In fact, even if the preliminary results at 1 km show some potential in detecting only uniform irrigation patterns over the Upper Tiber area, the prevalent characteristics of the area suggest the adoption of soil moisture products at a plot scale. Furthermore, the results obtained by the spatial analysis at 1 km are not clearly confirmed by the temporal analysis; hence, further investigations are needed. The results obtained with the THEIA Sentinel-1 soil moisture suggest to test this product in analyses aimed to quantify irrigation amounts at a plot scale. For the pilot fields within the Upper Tiber basin, the benchmark amounts of water applied for irrigation are already available. Over these fields, SM2RAIN experiments exploiting soil moisture data from the THEIA Sentinel-1 data set can be performed. It is noteworthy that the modeling of the evapotranspiration will be probably modified. In fact, it is not easy to obtain all the variables needed to implement the dual crop coefficient approach proposed in the FAO model (Equation 4.13), as at the considered spatial scale they should be ground-observed. Hence, two options are possible for the implementation of the proposed SM2RAIN setting over the pilot fields located in the Upper Tiber area and in the Left Tiber area. Over the single plot, the solver equation is hereby reported as Equation 7.1:

$$W_{in}(t) = Z^* \frac{dS(t)}{dt} + aS(t)^b + e(t) \tag{7.1}$$

The two possible options regard the representation of the $e(t)$ term. A first way consists in applying the single crop coefficient approach; in this case, the $e(t)$ term is calculated according to Equation (4.15) and the K_c coefficient can be derived from curves referred to the specific crop cultivated over the pilot field, or it can be approximated through the relation existing with the NDVI. The advantage of using K_c curves specific for crops or regions is that they take into account processes not captured by the NDVI, e.g., the growing of the fruit, which needs water but does not impact on the LAI. It is noteworthy that the rigorous application of the FAO model requires the $ET_0(t)$ term calculated according to the Penman-Monteith equation. As previously explained, the implementation of such method is difficult at the considered spatial scale. Hence, simplified formulations (e.g., the Hargreaves formula or the Thornthwaite equation) coupled with a coarser

modeling can be considered. For instance, the approach in which the potential evapotranspiration is only limited by the available water content already adopted in previous studies (Brocca et al., 2018; Filippucci et al., 2020) is an option. Another issue is represented by the calibration step, which can be performed over the same plot by masking out periods when irrigation rates are higher than zero (calibration during non-irrigation periods).

Another future step of the presented research is the assessment of the loss in reliability when using evapotranspiration observations from available data sets over the study area in the Ebro basin. Very preliminary investigations on this issue have been already done. Considering the SMAP experiment described in Chapter 6 as a benchmark, two alternative simulations performed by "degrading" the accuracy of the evapotranspiration information have been carried out. In the first of the two additional simulations, the potential evapotranspiration retrieved by MODIS sensor has been used. In this case, the SM2RAIN settings have been kept equal to the benchmark simulation. Instead, in the second additional simulation, the actual evapotranspiration has been directly taken from MODIS observations. The cumulated irrigation amounts obtained through these two experiments, together with gross and net benchmark amounts are shown in Figure 7.1; in detail, panel a) shows the results obtained by using exactly the same approach described in Chapter 6 with potential evapotranspiration from MODIS data instead of computed according to the Penman-Monteith method. Panel b) provides the results obtained in the simulation performed by taking the actual evapotranspiration rates directly from MODIS sensor. In the experiment exploiting potential evapotranspiration from MODIS, the retrieved irrigation overestimates the actually occurred one over all the districts, except for Pinyana. This issue can be explained by higher potential evapotranspiration rates in the MODIS-derived data with respect to those calculated in the benchmark simulation described in Chapter 6. It is noteworthy that the p parameter, regulating the beginning of stress conditions, has been maintained equal to 0.45; this is another factor affecting the results. Conversely, no losses in accuracy are obtained when putting the actual evapotranspiration from MODIS directly into the algorithm; in fact, the long-term magnitudes are well reproduced in this case, as differences rarely drop below -100 mm and are often close to zero. Overestimates are never observed for this experiment.
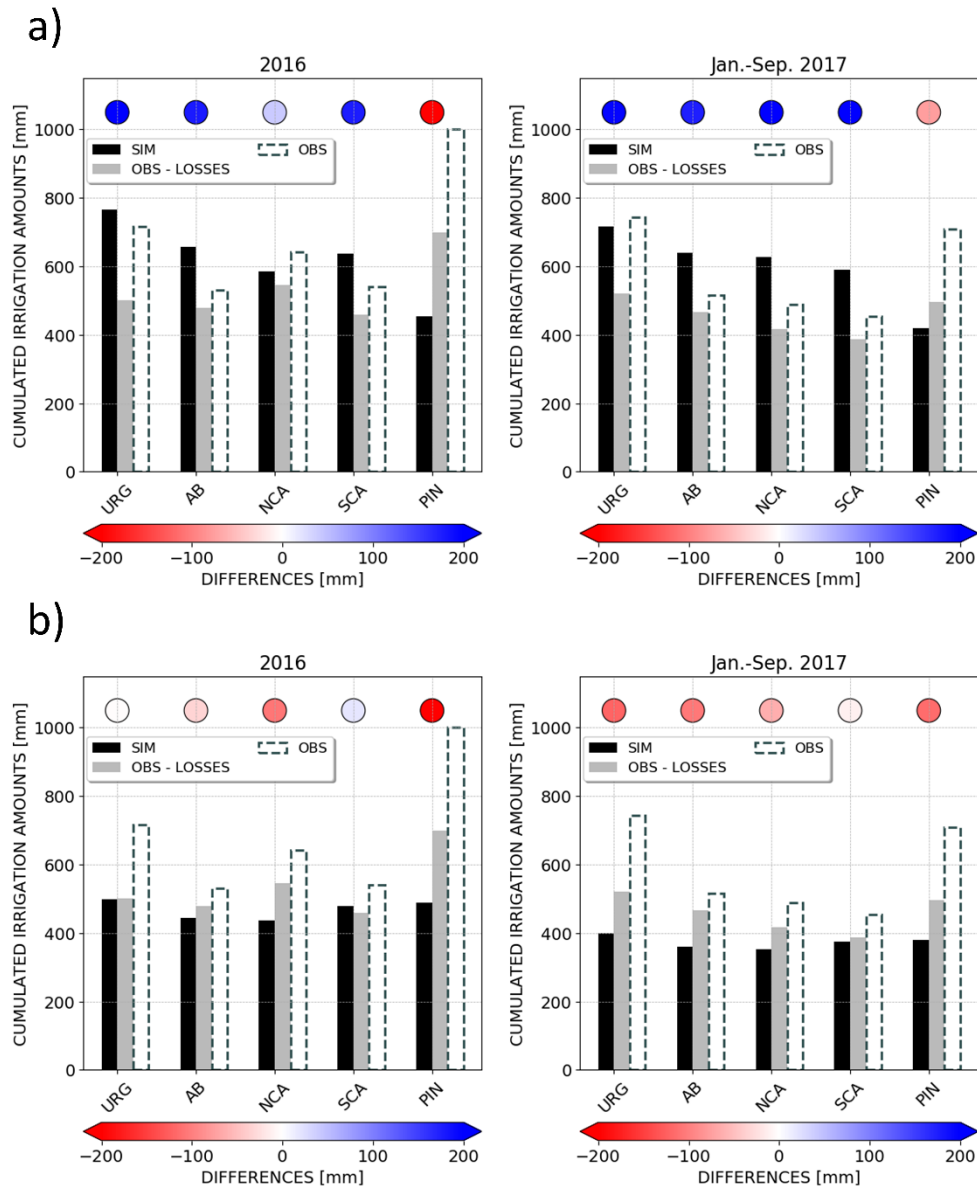
Figure 7.1. In panel a), long-term magnitudes obtained by the experiment using potential evapotranspiration from MODIS. In panel b), the same results obtained by the simulation exploiting actual evapotranspiration from MODIS. Each panel shows the estimated (black bars) and the observed cumulated irrigation amounts (light grey bars) during 2016 (on the left) and January-September 2017 (on the right) over the pilot districts: Urgell (URG), Algerri Balaguer (AB), North Catalan and Aragonese (NCA), South Catalan and Aragonese (SCA), and Pinyana (PIN). The colours of the circles above the bars indicate the differences between the estimated and the benchmark amounts.

Nevertheless, the spatial distribution of the cumulated irrigation amounts obtained by these two additional experiments reveals the inaccuracy in reproducing the areas where the highest irrigation rates are located in the

141

experiment using actual evapotranspiration from MODIS (see Figure 7.2). In fact, while the spatial distribution of the cumulated irrigation amounts obtained in the experiment using MODIS potential evapotranspiration is consistent with the benchmark simulation, the same is not valid for the experiment exploiting MODIS actual evapotranspiration. The reason relies in the different SM2RAIN settings adopted for the two simulations; in the one with MODIS potential evapotranspiration, the setting for the evapotranspiration term is the same adopted in the benchmark simulation; hence, the spatial distributions of the retrieved irrigation and of the crop coefficient are linked. Conversely, the irrigation patterns obtained by the experiment exploiting MODIS actual evapotranspiration are not much reliable, as they are almost constant over all the irrigation domain, with the only exception of a middle horizontal portion where higher rates are observed.
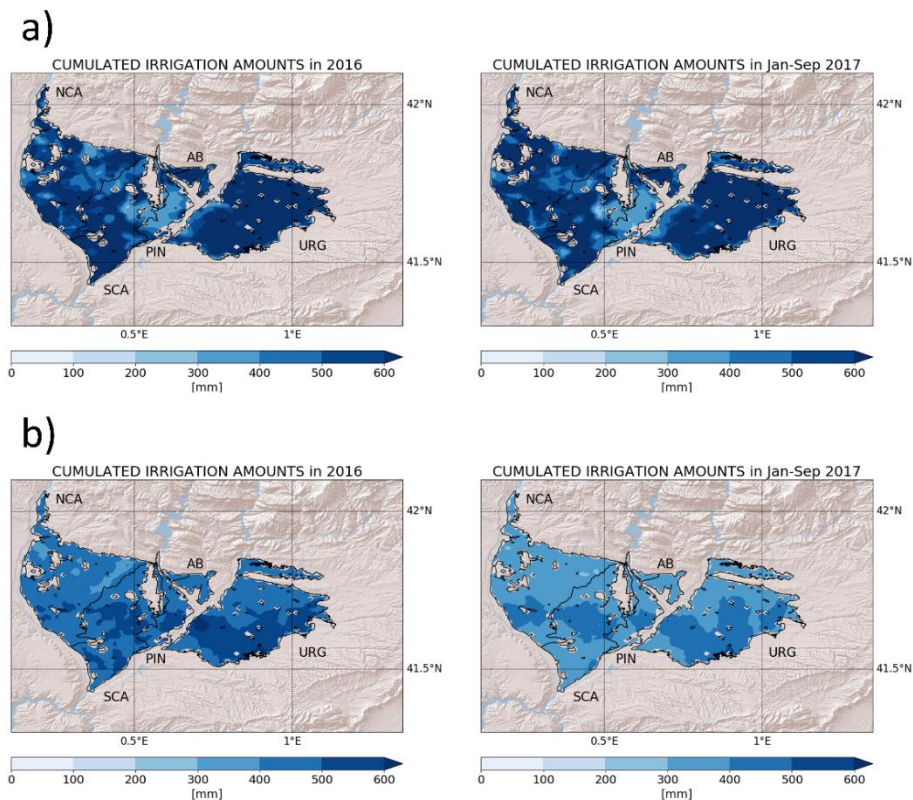
Figure 7.2. Maps of the estimated irrigation water amounts cumulated for the whole 2016 (left side) and for the period January-September 2017 (right side) over the pilot districts: URG stands for Urgell, AB for Algerri Balaguer, NCA for North Catalan and Aragonese, SCA for South Catalan and Aragonese, and PIN for Pinyana. Panel a) is referred to the experiment exploiting MODIS potential evapotranspiration and panel b) to the one exploiting MODIS actual evapotranspiration.

This issue is attributable to the actual evapotranspiration data set; in fact, similar patterns can be observed in the maps of the mean value of this variable during the highest-intensity irrigation periods in 2016 and 2017, which are provided in Figure 7.3.

However, the above discussed experiments only represent a preliminary analysis in the context of a more complex study related to this research. In fact, a comprehensive assessment of the performances obtained by applying the methodology described in Chapter 6 by exploiting multi-sources rainfall and evapotranspiration data is among the future perspectives of this work.
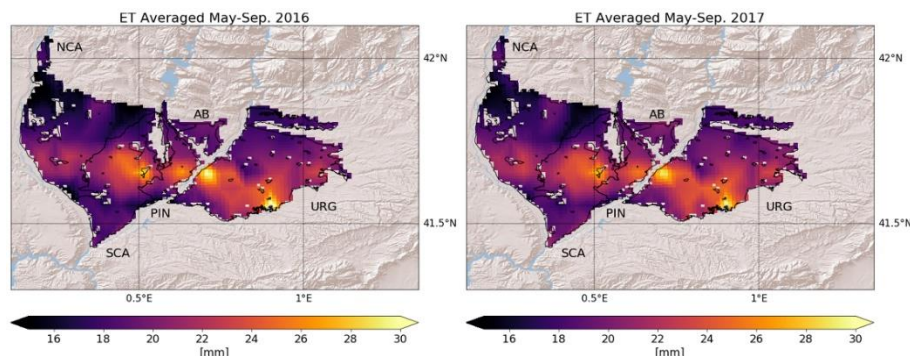
Figure 7.3. Spatial distribution of the mean actual evapotranspiration observed by the MODIS sensor during the period May-September 2016 (left side) and 2017 (right side) over the pilot area in the Ebro basin.

Plot-scale investigations on the potential in detecting and estimating irrigation over the study area within the Ebro basin through the Sentinel-1 data delivered by THEIA are foreseen, as well as comparisons with results obtained in similar studies (e.g., Bazzi et al., 2019).

Finally, other approaches aimed to the quantification of irrigation through remotely sensed data can be tested and compared with the method developed in this research. As an example, the approach proposed by Zaussinger et al. (2019) exploits the differences between remotely sensed and modeled soil moisture to retrieve the amounts of water applied for irrigation. Figure 7.4 provides a sketch synthetizing the idea beyond the approach.
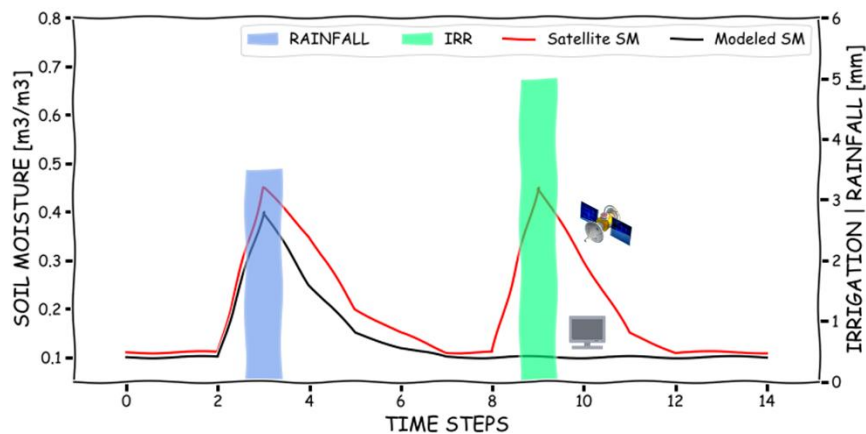
Figure 7.4. Sketch representing the idea beyond the method proposed by Zaussinger et al. (2019) to estimate irrigation through differences between remotely sensed and modeled soil moisture.

A remotely sensed soil moisture data set containing the irrigation information is influenced by both rainfall and irrigation events; conversely, a modeled soil moisture data is responsive to rainfall only, as it does not contain any irrigation information. Hence, by identifying irrigation events through the concomitance of a decrease in the modeled soil moisture and an increase in the observed one in absence of rainfall, the irrigation amounts can be retrieved by integrating all the differences between remotely sensed and modeled soil moisture during irrigation events. The approach is equivalent to attribute the differences between observed and modeled soil moisture to irrigation practices. The described method represents an alternative to the SM2RAIN-based approach to estimate irrigation. The implementation of such method through the DISPATCH downscaled products and SURFEX-ISBA outputs represents a future perspective of this research in the irrigation quantification framework.

7.2 Irrigation in SURFEX

Even if not yet published, a new version of SURFEX-ISBA involving a finer modelling of irrigation has been recently developed by Météo-France (Druel et al., 2019). In fact, an irrigation scheme was already available in SURFEX v8.1. In the new version, an irrigation scheme can be activated over irrigated areas when soil moisture drops below a threshold value. In this soil-moisture-deficit approach, the model is capable to simulate sprinkler, drip, and flood irrigation methods. An example of daily simulated irrigation over the Southern France and the Northern Spain averaged during the period 1979-1981 is provided in Figure 7.5; in this simulation, sprinkler irrigation has been adopted everywhere, as a detailed map

of the employed irrigation techniques is not available yet. The heavily irrigated pilot area in the Ebro basin can be immediately detected. The implementation of an irrigation scheme within SURFEX-ISBA opens important perspectives for this study. The outputs from simulations carried out with the irrigation scheme activated can be compared with those obtained with the canonical SURFEX-ISBA configuration in which the SM2RAIN-derived data set of estimated irrigation described in Chapter 6 is added to the atmospheric forcing or directly to the soil in order to assess the different impacts of the two configurations on the components of the hydrological cycle. Furthermore, comparisons between SURFEX-ISBA simulations in which the estimated irrigation is added to the atmospheric forcing (equivalent to assume that the irrigation amounts are supplied through sprinklers) or directly to the soil (thus simulating flood irrigation or drip irrigation) and SURFEX-ISBA simulations in which the irrigation scheme is not activated (reproducing the natural physical processes only) are useful to assess the impact of irrigation practices on the natural hydrological cycle.
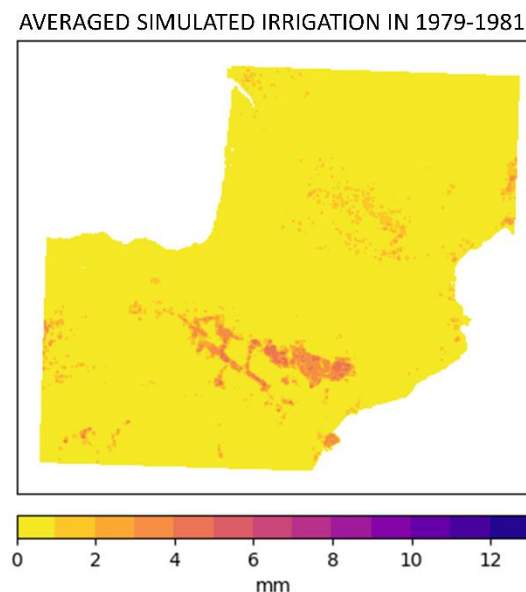
Figure 7.5. Output of SURFEX-ISBA simulation with the new irrigation scheme activated (courtesy of Pere Quintana-Seguí).

7.3 The IRRIGATION+ Project

The presented research fits perfectly into the activities foreseen by the IRRIGATION+ project, funded by ESA and started in March 2020. The project was born with the aim of advancing the comprehension of all the irrigation-related

issues (its extent, its timing, and how much water is used for it) through Earth Observation capabilities. The main targets of the project are:

1. The development of algorithms and methods to detect, map and quantify irrigation at three different spatial scales, from the plot scale to global scale. Local scale (less than 100 m) analyses can support the agricultural water management. Catchment and sub-catchment (~1 km) investigations are useful for water management purposes; finally, regional and global scale (more than 10 km) analyses are useful to support large-scale climate and hydrological studies;
2. the production of satellite-derived data sets from local to global scale as a basis for the operationalization of the irrigation products;
3. the assessment of the impact of the developed irrigation products on the society and on the science.

Five pilot areas have been chosen to develop and test the output products from the IRRIGATION+ project. The first case study is the Pianura Padana, in Northern Italy; it is the widest productive agricultural area of Italy. Information on amounts of water applied for irrigation purposes are available for four sites: Faenza, San Michele Fosdondo, Budrio, and Brunel. The second study area is the focus area within the Ebro basin investigated in this research. It is noteworthy that, along with all the features already described that make this site particularly suitable for irrigation-related studies, the area will also be involved in the HyMeX (HYdrological cycle in the Mediterranean Experiment) LIAISE campaign. A big amount of useful data is expected to be collected through such campaign: meteorological data, surface energy budget data, soil moisture, land surface temperature, and reference irrigation data. The third study area is the Adour Garonne basin, in France. For this domain, irrigation, rainfall, and soil tensiometry data from twenty-five pilot plots located in the Tarn and the Lot departments are available. The fourth case study, particularly suitable for testing evapotranspiration-based approaches, is the Hex Valley, Western Cape, South Africa. The last study area is the Lower Saxony, in Germany. For this area, about 7000 irrigation events during the summer season in 2016, 2017, and 2018 are available for four pilot sites. It is noteworthy that, additional data sets from additional case studies will also be evaluated.

For the irrigation quantification activity, several approaches will be exploited; they are the SM2RAIN approach, the soil moisture delta approach, data assimilation

techniques, and an evapotranspiration-based approach. Note that the SM2RAIN approach is the method adopted in this research and the soil moisture delta approach is the method proposed in Zaussinger et al. (2019). For the irrigation mapping activity two main methods will be adopted: one SVM-based (Bousbih et al., 2018) and another one exploits Sentinel-1 SAR time series (Gao et al., 2018; Bazzi et al., 2019). Finally, the irrigation timing will be assessed through an algorithm based on the comparison between derivative of observed soil moisture and derivative of a soil water balance.

It is noteworthy that, among the assessments of the impact of the developed irrigation products on science, a case study is represented by the irrigation parametrization described in Section 7.2. The SASER modelling chain, with the new SURFEX-ISBA scheme activated, will be tested over the Urgell and the outputs will be compared with irrigation estimates produced by the project and data collected from the LIAISE campaign. Finally, the impacts of irrigation practices on evapotranspiration and drainage will be evaluated through comparisons between irrigated and non-irrigated simulations.

Chapter 8

Conclusions

In this research, methodologies aimed to detect and map irrigated areas and to quantify the amounts of water used for this purposes have been developed. The proposed approaches, mainly based on remote sensing soil moisture, have been tested over two case studies, namely a heavily irrigated area within the Ebro basin, in Spain, and agricultural areas in the Upper Tiber basin, in Italy. The capability to detect irrigation of several remote sensing data sets has been investigated over the study area in Spain. The evaluated data sets are DISPATCH downscaled SMOS and SMAP versions at 1 km, SMAP at 9 km, Sentinel-1 at 1 km, and ASCAT at 12.5 km. The capability to detect irrigation of the considered products has been evaluated through indices describing the spatial-temporal dynamics of soil moisture and derived from the temporal stability theory. Then, a method exploiting the best-performing products to map irrigated areas through the K-means clustering algorithm has been developed. For the case study in Italy, the irrigation detection and mapping activity has been carried out by performing a double-scale analysis (1 km and plot-scale). The choice of such investigation has been determined by the topographic features of the study area, much complex than in the case study in the Ebro basin. In addition, except for the Upper Tiber area, irrigation is not evenly distributed, as the crop rotation is largely adopted. In the analysis at 1 km spatial resolution, the detectability of irrigation through several products has been investigated; they are the DISPATCH downscaled version of SMAP at 1 km and the Sentinel-1 at 1 km version delivered by the Copernicus Global Land Service, both used in the case study in the Ebro basin also, and a field-scale-born Sentinel-1 version produced by THEIA and aggregated at 1 km. In the analysis at a plot scale, the THEIA Sentinel-1 product, aggregated at 100 m, has been used. The detectability of irrigation signals has been assessed through the same approach adopted in the Spanish case study, namely by exploiting indices derived from the temporal stability theory. Maps of irrigated areas at high-resolution (100 m) have been produced through the K-means clustering algorithm.

Both the analyses aimed to detect irrigation signals carried out in the two study areas have been supported by an additional data set of soil moisture modeled through the SURFEX-ISBA land surface model. Irrigation estimates have been performed on the focus area in the Ebro basin only; two experiments have been performed: one exploiting DISPATCH downscaled SMAP data at 1 km and one exploiting DISPATCH downscaled SMOS data at 1 km. Both soil moisture data sets have been used as an input for the SM2RAIN algorithm, adapted to retrieve the irrigation water amounts. In this research, the guidelines provided in the FAO paper n. 56 have been implemented into the algorithm to adequately reproduce the crop evapotranspiration.

The main results of the irrigation detection and mapping analyses carried out over the case study in the Ebro basin during the period 2016-2017 are summarized in the following.

- 1 km spatial resolution is suitable to detect irrigation occurring over the pilot area in the Ebro basin through remote sensing soil moisture.
- Indices derived from the temporal stability theory are useful tools to assess the capability to detect irrigation of remote sensing products, as they describe the spatial-temporal dynamics of soil moisture.
- The DISPATCH downscaled L-band passive microwave products, namely SMAP and SMOS at 1 km, are the best performing data sets in detecting irrigation over the study area in the Ebro basin. Reliable information on where irrigation actually occurs is retrieved from these products. The worsening of the performances obtained by SMOS at 1 km in 2017 is attributable to RFI issues.
- The proposed methodology to map irrigated areas is particularly performing in distinguishing between irrigated areas and rainfed agricultural areas.
- According to both the validations carried out, ST.A.SMAP16 and ST.A.SMAP17 (please refer to Table 5.1 for the meaning of the codes) are the experiments that best reproduce irrigated areas. These classifications exploit remotely sensed soil moisture only; this is an interesting and comforting result, considering the scarcity of models running at 1 km spatial resolution over large areas. The better performances of the SMAP at 1 km data set with respect to the SMOS at 1 km data set are mainly attributable to the RFI problems affecting the latter.

- The experiments D.A.C.SMAP16 and D.A.C.SMAP17, merging remotely sensed and modeled soil moisture as input, are the best performing ones in concurrently reproducing all the three considered classes: the irrigated areas, the dryland, and the forest or natural areas.

The main results of the double-scale irrigation detection and mapping analysis carried out over the agricultural areas within the Upper Tiber basin during the period 2017-2019 are summarized in the following.

- Some potential in detecting uniform irrigation patterns over the Upper Tiber agricultural area is found in the analysis at 1 km spatial resolution. The result is common to all the remotely sensed products used and it is more evident for the analysis based on the spatial relative differences with respect to the investigation based on the temporal anomalies. For this reason, potential influences due to static patterns (e.g., soil texture) make further studies required.

- The Copernicus Sentinel-1 and THEIA Sentinel-1 aggregated at 1 km products show promising results in spotting scattered irrigation, confirmed by both spatial and temporal analyses.

- K-means clustering derived maps of irrigated areas at 100 m spatial resolution provide satisfactory results in reproducing the spatial distribution of irrigated fields. These classifications exploit remotely sensed soil moisture only. According to the limited ground truth information available, the clustering-derived maps appear reliable in reproducing the actually occurring irrigation events. A larger ground truth data set to perform a more comprehensive and reliable validation is desirable.

- THEIA Sentinel-1 soil moisture shows promising results in detecting irrigation events, even though limitations mainly due to the influence of the vegetation cover and to the low temporal frequency (6 days) are pointed out.

The main results of the SMAP experiment (period of interest: January 2016 – September 2017) and of the SMOS experiment (period of interest: January 2011 – September 2017) aimed to estimate the amounts of water actually applied for irrigation are summarized as follows.

- The proposed approach performs well in quantitatively reproducing the actually occurring irrigation over four of the five pilot districts.

- The methodology performs well not only in reproducing the long-term magnitudes of occurring irrigation, but the timing and the spatial distribution of irrigation events also. However, false irrigation alarms during winter are detected.

- The investigation aimed to determine which SM2RAIN term is the predominant one in determining the algorithm's output highlights the importance of a correct representation of the evapotranspiration term in SM2RAIN applications aimed to estimate irrigation over semi-arid regions. In fact, this term plays the leading role in determining the algorithm's output, more than the direct contribution of soil moisture variations. However, soil moisture plays indirect roles also, which are difficult to be quantitatively assessed.

- The obtained estimates are less sensitive to the algorithm's parameters Z^*, a, and b during the highest irrigation intensity season. The same is not valid for the p parameter, whose associated uncertainties are larger when irrigation mainly occurs.

- The DISPATCH downscaled products, namely SMAP and SMOS at 1 km, provide comparable results in estimating irrigation. Hence, a data set merging irrigation estimates obtained from the two experiments carried out and covering the period from January 2011 to September 2017 is produced.

The presented research has produced many interesting results that hopefully are only the first step of many future developments, which include the use of better validation data sets, models improvements, and the use of even more performing remote sensing products.

Bibliography

Abbot, B.W., Bishop, K., Zarnetske, J.P., Minaudo, C., Chapin III, F.S., Krause, S., Hannah, D.M., Conner, L., Ellison, D., Godsey, S.E., et al., 2019. Human domination of the global water cycle absent from depictions and perceptions. Nat. Geosci., 12, 533–540.

Abdullah, K.B., 2006. Use of water and land for food security and environmental sustainability. Irr. And Drain., 55 (3), 219–222.

Abolafia-Rosenzweig, R., Livneh, B., Small, E.E., Kumar, S.V., 2019. Soil moisture data assimilation to estimate irrigation water use. J. Adv. Model. Earth Syst., 11, 3670– 3690.

Albergel, C., Dutra, E., Munier, S., Calvet, J. C., Munoz-Sabater, J., de Rosnay, P., Balsamo, G., 2018. ERA-5 and ERA-Interim driven ISBA land surface model simulations: which one performs better? Hydrol. Earth Syst. Sci., 22, 3515-3532.

Allen, R.G., Pereira, L.S., Raes, D., Smith, M., 1998. Crop Evapotranspiration: Guidelines for Computing Crop Requirements, Irrigation and Drainage Paper; FAO: Rome, Italy.

Alter, R.E., Im, E.S., Eltahir, E.A., 2015. Rainfall consistently enhanced around the Gezira Scheme in East Africa due to irrigation. Nat. Geosci. 8, 763–767.

Ambika, A.K., Mishra, V., 2016. Remotely sensed high resolution irrigated area mapping in India for 2000 to 2015. Sci. Data 3, 160118.

Bartalis, Z., Wagner, W., Naeimi, V., Hasenauer, S., Scipal, K., Bonekamp, H., Figa, J., Anderson, J., 2007. Initial soil moisture retrievals from the METOP-A Advanced Scatterometer (ASCAT). Geophysical Research Letters. 34, L20401.

Bastiaanssen, W.G.M., Cheema, M.J.M., Immerzeel, W.W., Miltenburg, I.J., Pelgrum, H., 2012. Surface energy balance and actual evapotranspiration of the transboundary Indus Basin estimated from satellite measurements and the ETLook model, Water Resour. Res, 48.

Bauer-Marschallinger, B., Naeimi, V., Cao, S., Paulik, C., Schaufler, S., Stachl, T., Modanesi, S., Ciabatta, L., Massari, C., Brocca, L., Wagner, W., 2018. Towards

global soil moisture monitoring with Sentinel- 1: harnessing assets and overcoming obstacles. IEEE Trans. Geosci. Remote Sens., 57, 520-539.

Bazzi, H., Baghdadi, N., Ienco, D., El Hajj, M., Zribi, M., Belhouchette, H., Maria Jose Escorihuela, Demarez, V., 2019. Mapping Irrigated Areas Using Sentinel-1 Time Series in Catalonia, Spain. Remote Sens., 11(15), 1836.

Bazzi, H., Baghdadi, N., Fayad, I., Zribi, M., Belhouchette, H., Demarez, V., 2020. Near Real-Time Irrigation Detection at Plot Scale Using Sentinel-1 Data. Remote Sens., 12(9), 1456.

Boone, A., 2000. Modélisation des processus hydrologiques dans le schéma de surface ISBA: Inclusion d'un réservoir hydrologique, du gel et modélisation de la neige. Ph.D. thesis Université Paul Sabatier (Toulouse III).

Boone, A.A., Calvet, J.C., Noilhan, J., 1999. The inclusion of a third soil layer in a land surface scheme using the force-restore method. J. Appl. Meteorol., 38, 1611–1630.

Bousbih, S., Zribi, M., El Hajj, M., Baghdadi, N., Lili-Chabaane, Z., Gao, Q., Fanise, P., 2018. Soil moisture and irrigation mapping in a semi-arid region based on Sentinel-1 and Sentinel-2 synergy, Remote Sens., 10(12), 1953.

Breña-Naranjo, J. A., Kendall, A. D., Hyndman, D. W., 2014. Improved methods for satellite-based groundwater storage estimates: A decade of monitoring the high plains aquifer from space and ground observations. Geophys. Res. Lett., 41(17), 6167-6173.

Brocca, L., Ciabatta, L., Massari, C., Moramarco, T., Hahn, S., Hasenauer, S., Kidd, R., Dorigo, W., Wagner, W., Levizzani, V., 2014. Soil as a natural rain gauge: Estimating global rainfall from satellite soil moisture data. J. Geophys. Res., 119, 5128–5141.

Brocca, L., Filippucci, P., Hahn, S., Ciabatta, L., Massari, C., Camici, S., Schüller, L., Bojkov, B., Wagner, W., 2019. SM2RAIN-ASCAT (2007-2018): global daily satellite rainfall data from ASCAT soil moisture observations. Earth Syst. Sci. Data, 11, 1583-1601.

Brocca, L., Massari, C., Ciabatta, L., Moramarco, T., Penna, D., Zuecco, G., Pianezzola, L., Borga, M., Matgen, P., Martínez-Fernández, J., 2015. Rainfall estimation from in situ soil moisture observations at several sites in Europe: An evaluation of SM2RAIN algorithm. J. Hydrol. Hydromech., 63, 201–209.

Brocca, L., Melone, F., Moramarco, T., Morbidelli, R., 2010. Spatial-temporal variability of soil moisture and its estimation across scales. Water Resour. Res. 46, W02516.

Brocca, L., Moramarco, T., Melone, F., Wagner, W., 2013. A new method for rainfall estimation through soil moisture observations. Geophys. Res. Lett., 40, 853-858.

Brocca, L., Pellarin, T., Crow, W.T., Ciabatta, L., Massari, C., Ryu, D., Su, C.-H., Rudiger, C., Kerr, Y., 2016. Rainfall estimation by inverting SMOS soil moisture estimates: A comparison of different methods over Australia. J. Geophys. Res., 121, 12062–12079.

Brocca, L., Tarpanelli, A., Filippucci, P., Dorigo, W., Zaussinger, F., Gruber, A., Fernández-Prieto, D., 2018. How much water is used for irrigation? A new approach exploiting coarse resolution satellite soil moisture products. Int. J. Earth Obs. Geoinformation, 73, 752-766.

Cai, X., Rosegrant, M.W., 2002. Global Water Demand and Supply Projections: Part 1. A Modeling Approach. Water Int. 27, 159–169.

Calera-Belmonte, A., Jochu, A., Cuesta Garcia, A., Montoro ROdriguez, A., Lopez Fuster, P., 2005. Irrigation management from space: Towards user-friendly products. Irrig. Drain. Syst., 19, 337–353.

Canela, Ll., Barragán, J., Montserrat, J., 1991. Evaluación del riego por tablares en la colectividad de Linyola Canal de Urgell (Lleida). Riegos y Drenayes, 50, 24-48.

Chan, S.K., Bindlish, R., O'Neill, P., Jackson, T., Njoku, E., Dunbar, S., Chaubell, J., Piepmeier, J., et al., 2018. Development and assessment of the SMAP enhanced passive soil moisture product. Remote Sens. Environ., 204, 931-941.

Chen, F., Crow, W.T., Bindlish, R., Colliander, A., Burgin, M.S., Asanuma, J., Aida, K., 2018. Global-scale evaluation of SMAP, SMOS and ASCAT soil moisture products using triple collocation. Remote Sens. Environ., 214, 1-13.

Ciabatta, L., Marra, A.C., Panegrossi, G., Casella, D., Sano, P., Dietrich, S., Massari, C., Brocca, L., 2017. Daily precipitation estimation through different microwave sensors: verification study over Italy. J. Hydrol. 545, 436–450.

Ciabatta, L., Massari, C., Brocca, L., Gruber, A., Reimer, C., Hahn, S., Paulik, C., Dorigo, W., Kidd, R., Wagner, W., 2018. SM2RAIN-CCI: a new global long-term rainfall data set derived from ESA CCI soil moisture. Earth Syst. Sci. Data, 10, 267–280.

Colliander, A., Jackson, T.J., Bindlish, R., Chan, S., Das, N., Kim, S.B., Cosh, M.H., Dunbar, R.S., Dang, L., Pashaian, L., et al., 2017. Validation of SMAP surface soil moisture products with core validation sites. Remote Sens. Environ., 191, 215–231.

Cots, Ll., Montserrat, J.,; Borrás, E., Barragán, J., 1993. Evaluación del uso del agua en la zona de "Les Planes" (430 ha) del término municipal de Arbeca (Colectividad n. 13 de los Canales de Urgell, Lleida). XI Jornadas Técnicas sobre Riegos. Asociación Española de Riegos y Drenajes. Valladolid, 178-185.

Dari, J., Brocca, L., Quintana-Seguí, P., Escorihuela, M.J., Stefan, V., Morbidelli, R., 2020a. Exploiting high-resolution remote sensing soil moisture to estimate irrigation water amounts over a Mediterranean region. Remote Sens., 12, 2593.

Dari, J., Morbidelli, R., Saltalippi, C., Massari, C., Brocca, L., 2019. Spatial-temporal variability of soil moisture: Addressing the monitoring at the catchment scale. J. Hydrol. 570, 436-444.

Dari, J., Quintana-Seguí, P., Escorihuela, M.J., Stefan, V., Brocca, L., Morbidelli, R., 2021a. Detecting and mapping irrigated areas in a Mediterranean environment using remote sensing soil moisture and a land surface model. Under Review in J. Hydrol.

Dari, J., Quintana-Seguí, P., Escorihuela, M.J., Stefan, V., Morbidelli, R., Casadei, S., Brocca, L., 2021b. Double-scale analysis on the detectability of irrigation through remote sensing soil moisture over an area with complex topography in central Italy. Submitted to Sci. Total Environ.

Das, N.N., Entekhabi, D., Dunbar, R.S., Chaubell, M.J., Colliander, A., Yueh, S., Jagdhuber, T., Chen, F., Crow, W., et al., 2019. The SMAP and Copernicus Sentinel 1A/B microwave active-passive high resolution surface soil moisture product. Remote Sens. Environ., 233, 111380.

David, C.H., Habets, F., Maidment, D.R., Yang, Z.-L., 2011. RAPID applied to the SIM-France model. Hydrol. Process., 25, 3412-3425.

Deines, J. M., Kendall, A. D., Crowley, M. A., Rapp, J., Cardille, J. A., Hyndman, D. W., 2019. Mapping three decades of annual irrigation across the US High Plains Aquifer using Landsat and Google Earth Engine. Remote Sens. Environ., 233, 111400.

Deines, J.M., Kendall, A.D., Hyndman, D.W., 2017. Annual irrigation dynamics in the US Northern High Plains derived from Landsat satellite data. Geophys. Res. Lett. 44 (18), 9350–9360.

Dierckx, W., Sterckx, S., Benhadj, I., Livens, S., Duhoux, G., Van Achteren, T., Francois, M., Mellab, K., Saint, G., 2014. PROBA-V mission for global vegetation monitoring: Standard products and image quality. Int. J. Remote Sens., 35, 2589–2614.

Dobson, M.C., Ulaby, F.T., 1981. Microwave backscatter dependence on surface roughness, soil moisture and soil texture: Part iii- soil tension. IEEE Trans. Geosci. Remote Sens., 19, 51-61.

Döll, P., Siebert, S., 2002. Global modelling of irrigation water requirements. Water Resour. Res., 38, 81–810.

Druel, A., Albergel, C., Munier, S., Calvet, J.-C., 2019. Implementation of a new irrigation scheme in the ISBA Land Surface Model. EMS Annual Meeting, Copenhagen (Denmark), 9-13 September 2019.

Duchemin, B., Hadria, R., Er-Raki, S., Boulet, G., Maisongrande, P., Chehbouni, A., Escadafal, R., Ezzahar, J., et al., 2006. Monitoring wheat phenology and irrigation in center of Morocco: On the use of relationship between evapotranspiration, crops coefficients, leaf area index and remotely sensed vegetation indices. Agric. Water Manag., 79, 1–27.

Durand, Y., Brun, E., Merindol, L., Guyomarc'h, G., Lesaffre, B., Martin, E., 1993. A meteorological estimation of relevant parameters for snow models. Ann. Glaciol., 18, 65–71.

El Hajj, M., Baghdadi, N., Zribi, M., Bazzi, H., 2017. Synergic use of Sentinel-1 and Sentinel-2 images for operational soil moisture mapping at high spatial resolution over agricultural areas. Remote Sens., 9, 1292.

Entekhabi, D., Njoku, E.G., Neill, P.E., Kellogg, K.H., Crow, W.T., Edelstein, W.N., et al., 2010. The soil moisture active passive (SMAP) mission. Proceedings of the IEEE 2010, 98 (5), 704–716.

Er-Raki, S., Chehbouni, A., Guemouria, N., Duchemin, B., Ezzahar, J., Hadria, R., 2007. Combining FAO-56 model and ground-based remote sensing to estimate water consumptions of wheat crops in a semi-arid region. Agric. Water Manag., 87, 41–54.

Escorihuela, M. J., Quintana-Seguí, P., 2016. Comparison of remote sensing and simulated soil moisture datasets in Mediterranean landscapes. Remote Sens. Environ., 180, 99–114.

FAO 2006. AQUASTAT online database. Food and Agriculture Organization of the United Nations (FAO), available at: http://www.fao.org/ag/agl/aglw/aquastat/main/index.stm

Faroux, S., Kaptué Tchuenté, A.T., Roujean, J.-L., Masson, V., Martin, E., Le Moigne, P., 2013. ECOCLIMAP-II/Europe: a twofold database of ecosystems and surface parameters at 1km resolution based on satellite information for use in land surface, meteorological and climate models, Geosci. Model Dev., 6, 563– 582.

Filippucci, P., Tarpanelli, A., Massari, C., Serafini, A., Strati, V., Alberi, M., Raptis, K.G.C., Mantovani, F., Brocca, L., 2020. Soil moisture as a potential variable for tracking and quantifying irrigation: a case study with proximal gamma-ray spectroscopy data. Adv. Water Resour., 136, 103502.

Feki, M., Ravazzani, G., Ceppi, A., Mancini, M., 2018. Influence of soil hydraulic variability on soil moisture simulations and irrigation scheduling in a maze field. Agric. Water Manag., 202, 183-194.

Ferguson, C.R., Pan, M., Oki, T., 2018. The effect of global warming on future water availability: CMIP5 synthesis. Water Resour. Res., 54(10), 7791-7819.

Foley, J.A., Ramankutty, N., Brauman, K.A., Cassidy, E.S., Gerber, J.S., Johnston, M., et al., 2011. Solutions for a cultivated planet. Nature. 478 (7369), 337–342.

Fontanet, M., Fernàndez-Garcia, D., Ferrer, F., 2018. The value of satellite remote sensing soil moisture data and the DISPATCH algorithm in irrigation fields. Hydrol. Earth Syst. Sci., 22, 5889–5900. doi:10.5194/hess-22-5889-2018

Gao, X., Zhao, X., Si, B.C., Brocca, L., Hu, W., Wu, P., 2015. Catchment-scale variability of absolute versus temporal anomaly soil moisture: time-invariant part not always plays the leading role. J. Hydrol. 529, 1669–1678.

Gao, Q., Zribi, M., Escorihela, M.J., Baghdadi, N., Quintana-Seguí, P., 2018. Irrigation mapping using Sentinel-1 time series at field scale. Remote Sens., 10, 1495.

Girotto, M., De Lannoy, G.J.M., Reichle, R.H., Rodell, M., Draper, C., Bhanja, S.N., Mukherjee, A., 2017. Benefits and pitfalls of GRACE data assimilation: a case study of terrestrial water storage depletion in India. Geophys. Res. Lett., 44, 4107-4115.

Gleick, P.H., 2003. Global freshwater resources: Soft-path solutions for the 21st century. Science, 302, 1524.

Gorelick, N., Hancher, M., Dixon, M., Ilyushchenko, S., Thau, D., Moore, R., 2017. Google Earth Engine: planetary-scale geospatial analysis for everyone. Remote Sens. Environ., 202, 18-27.

Habets, F., Boone, A., & Noilhan, J., 2003. Simulation of a Scandinavian basin using the diffusion transfer version of ISBA. Glob. Planet. Change, 38, 137–149.

Haddeland, I., Skaugen, T., Lettenmaier, D.P., 2007. Hydrologic effects of land and water management in North America and Asia: 1700–1992. Hydrol. Earth Syst. Sci., 11, 1035-1045.

Hain, C.R., Crow, W.T., Anderson, M.C., Yilmaz, M.T., 2015. Diagnosing neglected soil moisture source–sink processes via a thermal infrared–based two-source energy balance model. J. Hydrometeorol. 16, 1070–1086.

Hersbach, H., Bell, B., Berrisford, P., Hirahara, S., Horányi, A., Muñoz-Sabater, J., Nicolas, J., Peubey, C., et al., 2020. The ERA5 global reanalysis. Q. J. Roy. Meteor. Soc., 1-51.

Hornáček, M., Wagner, W., Sabel, D., Truong, H.-L., Snoeij, P., Hahmann, T., Diedrich, E., Doubková, M., 2012. Potential for high resolution systematic global surface soil moisture retrieval via change detection using Sentinel-1. Sel. Top. Appl. Earth Obs. Remote Sens., IEEE J. Of, 5, 1303–1311.

Hu, X., Shi, L., Zeng, J., Yang, J., Zha, Y., Yao, Y., Cao, G., 2016. Estimation of actual irrigation amount and its impact on groundwater depletion: A case study in the Hebei Plain, China. J. Hydrol., 543(B), 433-449.

Hunter, M.C., Smith, R.G., Schipanski, M.E., Atwood, L.W., Mortensen, D.A., 2017. Agriculture in 2050: Recalibrating targets for sustainable intensification. BioScience, 67(4), 386-391.

Jalilvand, E., Tajrishy, M., Hashemi, S.A.G., Brocca, L., 2019. Quantification of irrigation water using remote sensing of soil moisture in a semi-arid region. Remote Sens. Environ., 231, 111226.

Jin, N., Tao, B., Ren, W., Feng, M., Sun, R., He, L., Zhuang, W., Yu, Q., 2016. Mapping irrigated and rainfed wheat areas using multi-temporal satellite data. Remote Sens., 8(3), 207.

Kerr, Y. H., Waldteufel, P., Wigneron, J. P., Delwart, S., Cabot, F., Boutin, J., Escorihuela, M. J., Font, J., Reul, N., Gruhier, C., et al., 2010. The SMOS mission:

New tool for monitoring key elements of the global water cycle. Proceedings of the IEEE, 98, 666–687.

Koster, R.D., Brocca, L., Crow, W.T., Burgin, M.S., De Lannoy, G.J.M., 2016. Precipitation estimation using L -band and C-band soil moisture retrievals. Water Resour. Res. 52 (9), 7213–7225.

Kueppers, L. M., Snyder, M. A., Sloan, L. C., 2007. Irrigation cooling effect: Regional climate forcing by land-use change. Geophys. Res. Lett., 34, L03703.

Kumar, S.V., Jasinski, M., Mocko, D.M., Rodell, M., Borak, J., Li, B., Beaudoing, H.K., Peters-Lidard, C.D., 2019. NCA-LDAS land analysis: Development and performance of a multisensor, multivariate land data assimilation system for the national climate assessment. J. Hydrometeorol., 20(8), 1571-1593.

Kumar, S. V., Peters-Lidard, C. D., Santanello, J. A., Reichle, R. H., Draper, C. S., Koster, R. D., Nearing, G., Jasinski, M. F., 2015. Evaluating the utility of satellite soil moisture retrievals over irrigated areas and the ability of land data assimilation methods to correct for unmodeled processes, Hydrol. Earth Syst. Sci., 19, 4463–4478.

Kummu, M., Guillaume, J., De Moel, H., Eisner, S., Flörke, M., Porkka, M., Siebert, S., Veldkamp, T., Ward, P., 2016. The world's road to water scarcity: shortage and stress in the 20th century and pathways towards sustainability. Sci. Rep.-UK, 6, 38495.

Lawston, P.M., Santanello, J.A., Kumar, S.V., 2017. Irrigation signals detected from SMAP soil moisture retrievals. Geophys. Res. Lett. 44, 11,860–867.

Le Page, M., Jarlan, L., El Hajj, M.M., Zribi, M., Baghdadi, N., Boone, A., 2020. Potential for the detection of irrigation events on maize plots using Sentinel-1 soil moisture products. Remote Sens, 12, 1621.

Lei, F., Crow, W.T., Kustas, W.P., Dong, J., Yang, Y., Knipper, K.R., Anderson, M.C., Gao, F., Notarnicola, C., Greifeneder, F., McKee, L.M., Alfieri, J.G., Hain, C., Dokoozlian, N., 2020. Data assimilation of high-resolution thermal and radar remote sensing retrievals for soil moisture m onitoring in a drip-irrigated vineyard. Remote Sens. Environ., 239, 1116222.

Lievens, H., Reichle, R.H., Liu, Q., De Lannoy, G.J.M., Dunbar, R.S., Kim, S.B., Das, N.N., Cosh, M., Walker, J.P., Wagner, W., 2017. Joint Sentinel-1 and SMAP data assimilation to improve soil moisture estimates. Geophys. Res. Lett. 44, 6145– 6153.

MacQueen, J.B., 1967. Some methods for classification and analysis of multivariate observations. Proceedings of 5-th Berkeley Symposium on Mathematical Statistics and Probability, Berkeley, University of California Press, 1:281-297.

Mahfouf, J. F. F., Noilhan, J., 1996. Inclusion of gravitational drainage in a land surface scheme based on the force-restore method. J. Appl. Meteorol., 35, 987–992.

Malbéteau, Y., Merlin, O., Molero, B., Rüdiger, C., Bacon, S., 2015. DisPATCh as a tool to evaluate coarse.scale remotely sensed soil moisture using localized in situ measurements: Application to SMOS and AMSR.E data in Southeastern Australia. Int. J. Appl. Earth Obs. Geoinf., 45, 221–234.

Massari, C., Brocca, L., Pellarin, T., Abramowitz, G., Filippucci, P., Ciabatta, L., Maggioni, V., Kerr, Y., Fernandez Prieto, D., 2020. A daily 25 km short-latency rainfall product for data-scarce regions based on the integration of the Global Precipitation Measurement mission rainfall and multiple-satellite soil moisture products. Hydrol. Earth Syst. Sci., 24, 2687-2710.

Masson, V., Le Moigne, P., Martin, E., Faroux, S., Alias, A., Alkama, R., ... Voldoire, A., 2013. The SURFEXv7.2 land and ocean surface platform for coupled or offline simulation of earth surface variables and fluxes. Geosci. Model Dev., 6, 929–960.

Maté, L., Cruz, J., Cruz, L.M., 1994. Evaluación de la eficiencia de un polígono de riego en la zona del Canal de Aragón y Cataluña y estimación del ahorro potencial de agua de riego debido a la aplicación de la técnica de refino láser y al aumento del módulo de agua disponible. Actas del Symposium Nacional sobre presente y futuro de los regadíos españoles.

Merlin, O., Escorihuela, M. J., Mayoral, M. A., Hagolle, O., AlBitar, A., Kerr, Y., 2013. Self-calibrated evaporation-based disaggregation of SMOS soil moisture: An evaluation study at 3 km and 100 m resolution in Catalunya, Spain. Remote Sens. Environ., 130, 25–38.

Merlin, O., Walker, J. P., Chehbouni, A., Kerr, Y., 2008. Towards deterministic downscaling of SMOS soil moisture using MODIS derived soil evaporative efficiency. Remote Sens. Environ., 112, 3935–3946.

Mittelbach, H., Seneviratne, S.I., 2012. A new perspective on the spatio-temporal variability of soil moisture: temporal dynamics versus time-invariant contributions. Hydrol. Earth Syst. Sci., 16, 2169–2179.

Molero, B, Merlin, O., Malbéteau, Y., Al Bitar, A., Cabot, F., Stefan, V., Kerr, Y., Bacon, S., Cosh, M.H., Bindlish, R., Jackson, T.J., 2016. SMOS disaggregated soil

moisture product at 1 km resolution: Processor overview and first validation results. Remote Sens. Environ., 180, 361-376.

Montanari, A., Young, G., Savenije, H. H. G., Hughes, D., Wagener, T., Ren, L. L., Koutsoyiannis, D., Cudennec, C., Toth, E., et al., 2013. "Panta Rhei – Everything Flows": Change in hydrology and society – The IAHS Scientific Decade 2013– 2022. Hydrol. Sci. J., 58, 1256-1275.

Monteith, J.L., 1965. Evaporation and environment. In Proceedings of the 19th Symposium of the Society for Experimental Biology, Cambridge University Press, New York, NY, USA, 205–233.

Moore, N., Rojstaczer, S., 2002. Irrigation's influence on precipitation: Texas High Plains, U.S.A. Geophys. Res. Lett., 29(16).

Morbidelli, R., Saltalippi, C., Flammini, A., Cifrodelli, M., Dari, J., Corradini, C., García-Marín, A.P., Moramarco, T., 2019. On the applicability of temporal stability analysis to raingauge network design. Hydrol. Sci. J., 64, 1424-1438.

Mualem, Y., 1986. Hydraulic Conductivity of Unsaturated Soils: Prediction and Formulas. Methods of Soil Analysis, A. Klute (Ed.).

Naeimi, V., Scipal, K., Bartalis, Z., Hasenauer, S., Wagner, W., 2009. An improved soil moisture retrieval algorithm for ERS and METOP scatterometer observations. IEEE Trans. Geosci. Remote Sens., 47, 1999–2013.

Nie, W., Zaitchik, B.F., Rodell, M., Kumar, S.V., Anderson, M.C., Hain, C., 2018. Groundwater withdrawals under drought: Reconciling GRACE and land surface models in the United States High Plains Aquifer. Water Resour. Res., 54(8), 5282-5299.

Noilhan, J., Mahfouf, J., 1996. The ISBA land surface parameterisation scheme. Glob. Planet. Change, 13, 145–159.

Noilhan, J., Planton, S., 1989. A simple parameterization of land surface processes for meteorological models. Monthly Weather Review, 117, 536–549.

O'Neill, P. E., Chan, S., Njoku, E. G., Jackson, T., Bindlish, R., 2016. SMAP enhanced L3 radiometer global daily 9 km EASE-grid soil moisture, version 1. L2_SM_P-E. Boulder, CO: NASA National Snow and Ice Data Center Distributed Active Archive Center.

Ozdogan, M., Gutman, G., 2008. A new methodology to map irrigated areas using multi- temporal MODIS and ancillary data: an application example in the continental US. Remote Sens. Environ. 112, 3520–3537.

Ozdogan, M., Yang, Y., Allez, G., Cervantes, C., 2010. Remote sensing of irrigated agriculture: opportunities and challenges. Remote Sens. 2, 2274–2304.

Peña-Arancibia, J.L.; Mainuddin, M.; Kirby, J.M.; Chiew, F.H.S.; McVicar, T.R., Vaze, J., 2016. Assessing irrigated agriculture's surface water and groundwater consumption by combining satellite remote sensing and hydrologic modelling. Sci. Total Environ., 542, 372–382.

Peña-Arancibia, J.L., McVicar, T.R., Paydar, Z., Li, L., Guerschman, J.P., Donohue, R.J., Dutta, D., Podger, G.M., van Dijk, A.I.J.M., Chiew, F.H.S., 2014. Dynamic identification of summer cropping irrigated areas in a large basin experiencing extreme climatic variability. Remote Sens. Environ. 154, 139–152.

Peng, J., Loew, A., Merlin, O., Verhoest, N.E.C., 2017. A review of spatial downscaling of satellite remotely sensed soil moisture. Rev. Geophys., 55, 341-366.

Penman, H.L., 1948. Natural evaporation from open water, bare soil, and grass. Proc. R. Soc. Lond., 193, 120–146.

Poe, G., 1990. Optimum interpolation of imaging microwave radiometer data. IEEE Trans. Geosci. Remote Sens., 28(5), 800–810.

Pokhrel, Y.N., Hanasaki, N., Wada, Y., Kim, H., 2016. Recent progresses in incorporating human land-water management into global land surface models toward their integration into Earth system models, WIREs Water, 3, 548-574.

Pulliainen, J. T., Manninen, T., Hallikainen, M. T., 1998. Application of ERS-1 wind scatterometer data to soil moisture monitoring in boreal forest zone. IEEE Trans. Geosci. Remote Sens., 34, 758-770.

Qiu, J., Gao, Q., Wang, S., Su, Z., 2016. Comparison of temporal trends from multiple soil moisture data sets and precipitation: the implication of irrigation on regional soil moisture trend. Int. J. Appl. Earth Observ. Geoinf., 48, 17–27.

Quintana-Seguí, P., Le Moigne, P., Durand, Y., Martin, E., Habets, F., Baillon, M., Canellas, C., Franchisteguy, L., Morel, S., 2008. J. Appl. Meteorol. Climatol., 47, 92–107.

Quintana-Seguí, P., Peral, C., Turco, M., Llasat, M.C., Martin, E., 2016. Meteorological anaòysis systems in North-East Spain: Validation of SAFRAN and SPAN. J. Environ. Inform., 27(2), 116-130.

Quintana-Seguí, P., Turco, M., Herrera, S., Miguez-Macho, G., 2017. Validation of a new SAFRAN-based gridded precipitation product for Spain and comparisons to Spain02 and ERA-Interim. Hydrol. Earth Syst. Sci., 21, 2187–2201.

Ray, S.S., Dadhwal, V.K., 2001. Estimation of crop evapotranspiration of irrigation command area using remote sensing and GIS. Agric. Water Manag., 49, 239–249.

Rockström, J., Falkenmark, M., Lannerstad, M., Karlberg, L., 2012. The planetary water drama: Dual task of feeding humanity and curbing climate change. Geophys. Res. Lett., 39, L15401.

Romaguera, M., Krol, M., Salama, M., Su, Z., Hoekstra, A., 2014. Application of a remote sensing method for estimating monthly blue water evapotranspiration in irrigated agriculture. Remote Sens. 6, 10033–10050.

Rosegrant, M.W., Meijer, S., Cline, S.A., 2002. International Model for Policy Analysis of Agricultural Commodities and Trade (IMPACT): Model Description; IFPRI: Washington, DC, USA.

Savenije, H. H. G., Hoekstra, A. Y., and van der Zaag, P., 2014. Evolving water science in the Anthropocene, Hydrol. Earth Syst. Sci., 18, 319–332.

Schmugge, T.J., 1985. Chapter 5: Remote Sensing of Soil Moisture. In: Anderson, M.G., Burt, T.P. (Eds.), Hydrological Forecasting, John Wiley and Sons, New York, 101-124.

Siebert, S., Henrich, V., Frenken, K., Burke, J., 2013. Global Map of Irrigation Areas version 5. Rheinische Friedrich-Wilhelms-University, Bonn, Germany / Food and Agriculture Organization of the United Nations, Rome, Italy.

Siebert, S., Kummu, M., Porkka, M., Döll, P., Ramankutty, N., Scanlon, B.R., 2015. A global data set of the extent of irrigated land from 1900 to 2005. Hydrol. Earth Syst. Sci., 19, 1521-1545.

Simonneaux, V., Duchemin, B., Helson, D., Er-Raki, S., Olioso, A., Chehboun, A.G., 2008. The use of high-resolution image time series for crop classification and evapotranspiration estimate over an irrigated area in central Morocco. Int. J. Remote Sens., 29, 95–116.

Steffen, W., Grinevald, J., Crutzen, P., and McNeill, J., 2011. Anthropocene: conceptual and historical perspectives, Philos. T. R. Soc. A, 369, 842–867.

Sterckx, S., Benhadj, I., Duhoux, G., Livens, S., Dierckx, W., Goor, E., Adriaensen, S., Heyns, W., Van Hoof, K., Strackx, G., et al. The PROBA-V mission: Image processing and calibration. Int. J. Remote Sens., 35, 2565–2588.

Stogryn, A., 1978. Estimates of brightness temperatures from scanning radiometer data, IEEE Transactions on Antenna and Propagation, vol. AP-26, 720–726.

Su, Z., Troch, P.A., De Troch, F.P., 1996. A method for retrieving soil moisture using active microwave data. Physics Chem. Earth, 22(3-4), 235-239.

Teluguntla, P., Thenkabail, P.S., Xiong, J., Gumma, M.K., Congalton, R.G., Oliphant, A., et al., 2017. Spectral matching techniques (SMTs) and automated cropland classification algorithms (ACCAs) for mapping croplands of Australia using MODIS 250-m time-series (2000–2015) data. Int. J. Digit. Earth 8947, 1–34.

Thenkabail, P.S., Biradar, C.M., Noojipady, P., Dheeravath, V., Li, Y., Velpuri, M., Gumma, M., Gangalakunta, O.R.P., Turral, H., Cai, X., Vithanage, J., Schull, M., Dutta, R., 2009. Global irrigated area map (GIAM), derived from remote sensing, for the end of the last millennium. Int. J. Remote Sens., 30, 3679-3733.

Thenkabail, P.S., Parthasaradhi, G., Biggs, T.W., Gumma, M.K., Turral, H., 2007. Spectral matching techniques to determine historical land use/land cover (LULC) and irrigated areas using time-series AVHRR Pathfinder datasets in the Krishna river basin, India. Photogramm. Eng. Remote Sensing, 73, 1029-1040.

Toureiro, C., Serralheiro, R., Shahidian, S., Sousa, A., 2016. Irrigation management with remote sensing: Evaluating irrigation requirements for maize under Mediterranean climate condition. Agric. Water Manag., 184, 211–220.

Ulaby, F.T., Moore, R.K., Fung, A.K., 1986. Microwave Remote Sensing, Active and Passive: From Theory to Applications, Volume III. Artech House, Norwood, MA, 1065-2162.

Vachaud, G., Passerat de Silans, A., Balabanis, P., Vauclin, M., 1985. Temporal stability of spatial measured soil water probability density function. Soil Sci. Soc. Am. J. 49, 822–828.

Van Eekelen, M.W., Bastiaanssen, W.G., Jarmain, C., Jackson, B., Ferreira, F., Van der Zaag, P., et al., 2015. A novel approach to estimate direct and indirect water

withdrawals from satellite measurements: a case study from the Incomati basin. Agric. Ecosyst. Environ., 200, 126–142.

Vidal, J.P., Martin, E., Franchistéguy, L., Baillon, M., Soubeyroux, J.M., 2010. A 50-year high-resolution atmospheric reanalysis over France with the Safran system. Int. J. Climatol., 30, 1627–1644.

Vörösmarty, C. J., Green, P., Salisbury, J., and Lammers, R. B., 2000. Global water resources: vulnerability from climate change and population growth. Science, 289, 284–288.

Wada, Y., Wisser, D., Bierkens, M.F.P., 2014. Global modeling of withdrawal, allocation and consumptive use of surface water and groundwater resources. Earth Syst. Dyn. 5 (1), 15–40.

Wagner W., Blöschl, G., Pampaloni, P, Calvet, J. C., Bizzarri, B., Wigneron, J. P., Kerr, Y., 2007. Operational readiness of microwave remote sensing of soil moisture for hydrologic applications. Nord. Hydrol., 38, 1-20.

Wagner, W., Hahn, S., Kidd, R., Melzer, T., Bartalis, Z., Hase- nauer, S., Figa-Saldaña, J., de Rosnay, P., et al., 2013. The ASCAT soil moisture product: A review of its specifications, validation results, and emerging applications. Meteorologische Zeitschrift, 22, 5–33.

Wagner, W., Lemoine, G., Rott, H., 1999. A method for estimating soil moisture from ERS scatterometer and soil data. Remote Sens. Environ., 70, 191–207.

Wen, J., Su, Z. B., 2003. A time series based method for estimating relative soil moisture with ERS wind scatterometer data. Geophys. Res. Lett., 30, 1397.

Zaussinger, F., Dourigo, W., Gruber, A., Tarpanelli, A., Filippucci, P., Brocca, L., 2019. Estimating irrigation water use over the contiguous United States by combining satellite and reanalysis soil moisture data. Hydrol. Earth Syst. Sci., 23, 897–923.

Zhang, X., Qiu, J., Leng, G., Yang, Y., Gao, Q., Fan, Y., Luo, J., 2018. The Potential Utility of Satellite Soil Moisture Retrievals for Detecting Irrigation Patterns in China. Water, 10(11), 1505.

Zhou, T., Haddeland, I., Nijssen, B. and Lettenmaier, D. P., 2016. Human-induced changes in the global water cycle. Terrestrial Water Cycle and Climate Change: Natural and Human-Induced Impacts, Geophysical Monograph 221, First Edition.

Zohaib, M., Choi, M., 2020. Satellite-based global-scale irrigation water use and its contemporary trends. Sci. Total Environ., 714, 136719.